Aalto University
School of Chemical
Engineering

Juhani Heimo

Thermal Conductivity of Titanium Slags

Master's Programme in Chemical, Biochemical and Materials Engineering
Major in Sustainable Metals Processing

Master's thesis for the degree of Master of Science in Technology submitted for inspection, Espoo, 28th of August, 2018.

Supervisor Professor Ari Jokilaakso

Instructors D.Sc. Marko Kekkonen
M.Sc. Timo Haimi

Aalto University
School of Chemical
Engineering

Aalto University, P.O. BOX 11000, 00076 AALTO
www.aalto.fi

Abstract of master's thesis

Author Juhani Heimo

Title of thesis Thermal Conductivity of Titanium Slags

Degree Programme Master's Programme in Chemical, Biochemical and Materials Engineering

Major Sustainable Metals Processing

Thesis supervisor Ari Jokilaakso

Thesis advisors/Thesis examiners Marko Kekkonen, Timo Haimi

Date 28.08.2018 Number of pages 71 + 32 Language English

Ilmenite ($FeTiO_3$) is smelted in electric arc furnace (EAF) to produce high-titania slag. The slag is highly corrosive, and a freeze-lining is required to protect the refractory lining. The thickness and stability of the freeze-lining is dependent on the heat flux through the furnace wall layers. This thesis seeks to investigate the thermal conductivity of the high-titania slag. A secondary aim is to compare two measurement methods, transient plane source (TPS) and laser flash analysis (LFA).

The thermal conductivity of two titania slag samples is measured from room temperature to 400 °C with the TPS method, using Hot Disk instruments TPS 2500 S. Three slag samples and an additional sample of excavated freeze-lining are measured with Netzsch LFA 457 from room temperature to 1100 °C. Additionally one slag sample was measured with Netzsch LFA 427 at 1400 °C. Additional characterization included SEM-EDS and CT.

Prior research did not include values for thermal conductivities of titania slag. Measured values were compared to data of other slags, and refractory materials. The thermal conductivity of the samples was found to increase with increasing temperature. An exception was the freeze-lining sample. Its thermal conductivity began to decrease starting from room temperature up until 500 °C. With further heating, thermal conductivity began to climb. Values for all samples at all temperatures ranged from 1 W/mK to 5 W/mK, being in the same order of magnitude. There appears to be a trend of increasing temperature dependence of the thermal conductivity for all the slags.

Keywords Freeze-lining, Ilmenite, EAF, Thermal conductivity

Aalto-yliopisto
Kemian tekniikan
korkeakoulu

Aalto-yliopisto, PL 11000, 00076 AALTO
www.aalto.fi

Diplomityön tiivistelmä

Tekijä Juhani Heimo		
Työn nimi Titaanikuonien lämmönjohtavuus		
Koulutusohjelma Kemian, biokemian ja materiaalitekniikan maisteriohjelma		
Pääaine Metallien prosessi- ja kierrätystekniikka		
Työn valvoja Ari Jokilaakso		
Työn ohjaajat/Työn tarkastajat Marko Kekkonen, Timo Haimi		
Päivämäärä 28.8.2018	Sivumäärä 71 + 32	Kieli englanti

Titaanidioksidikuonaa valmistetaan sulattamalla ilmeniittiä ($FeTiO_3$) valokaariuunissa. Kuona on hyvin syövyttävää, ja uunin reunoille täytyy muodostaa kerros jähmettynyttä kuonaa tulenkestävän vuorauksen suojelemiseksi. Tämän jähmettyneen kerroksen paksuus riippuu uunin seinäkerrosten läpi kulkevasta lämpövirrasta. Tämän diplomityön päätavoite on selvittää titaanidioksidikuonan lämmönjohtavuutta. Toisarvoisena päämääränä on tarkoitus verrata kahta erilaista lämpöominaisuuksien mittausmenetelmää, hetkellistä tasolähdettä (transient plane source, TPS) ja laserpulssianalyysiä (laser flash analysis, LFA).

Kahden titaanidioksidikuonan lämmönjohtavuus mitattiin huoneenlämmöstä 400 °C:n TPS-menetelmällä, Hot Disk Instruments TPS 2500 S-laitteella. Netzsch LFA 457-laitteella mitattiin huoneenlämmöstä 1100 °C asti kolme kuonanäytettä, ja yksi seisakin aikana uunin seinämästä kaivettu, jähmettynyttä kuonakerrosta edustava näyte. Lisäksi yksi kuonanäytteistä mittautettiin Netzsch LFA 427 -instrumentilla 1400 °C:ssa. Lisäksi näytteiden karakterisointiin käytettiin SEM-EDS:a ja tietokonetomografiaa.

Aikaisemmasta tieteellisestä tutkimuksesta ei löytynyt mitattuja arvoja titaanikuonan lämmönjohtavuudelle. Kokeellisesti saatuja arvoja verrattiin täten muunlaisten metallurgisten kuonien ja tulenkestävien materiaalien lämmönjohtavuuden arvoihin. Kuonanäytteiden lämmönjohtavuus kasvoi lämpötilan noustessa. Uunin seinämästä peräisin olevan näytteen lämmönjohtavuus laski huoneenlämpötilasta 500 °C asti, kääntyen kasvuun lämpötilan noustessa. Näytteiden lämmönjohtavuus pysyi samassa kokoluokassa, vaihdellen 1 ja 5 W/mK välillä. Kuonanäytteiden lämmönjohtavuuden riippuvuus lämpötilasta vaikuttaa voimistuvan lämpötilan kasvaessa.

Avainsanat Autogeenivuoraus, Ilmeniitti, Valokaariuuni, Lämmönjohtavuus

Foreword

This thesis project has provided me with great opportunities to grow as a person and see the world. Thus, I would like to extend my heartfelt thanks to my supervisor Professor Ari Jokilaakso for his perseverance in recruiting me for this project, and perceptive feedback along the way. For their guidance and constructive criticism, my instructors Dr. Marko Kekkonen and Timo Haimi deserve my gratitude. In addition to Timo, others from Outotec have also been very helpful to the cause: thanks Petri Palovaara and Pasi Mäkelä from ORC. Professor Michael Gasik assisted me with the Hot Disk device, and Kalle Jalava provided indispensable practical knowledge about the high temperature measurements. Professor Pekka Taskinen also lent some of his vast expertise to help me along in my study of phase compositions.

Professor Merete Tangstad was an irreplaceable cog in the machine, facilitating my stay at NTNU and providing apt critique when the need presented itself. I would also like to thank Professor Leiv Kolbeinsen from NTNU for his input on ilmenite slags. Anne Støre and Ove Darell from SINTEF were absolutely instrumental to the success of the experiments during my stint in sunny Trondheim, providing many a cup of coffee in addition to their critical expertise. Samuel Rantataro spent hours in the chemistry building basement on my behalf, creating SEM-EDS analyses. Cheers to all the bearded men that shared an office with me in the dearly departed materials science building, Ise, J-P, Samu and Jani.

Finally, I want to thank my family, my friends all over Finland, and my dear partner Elisa for their ongoing support and unconditional love throughout my studies. You are the people responsible for me being who I am today, and without you this thesis would not have been written.

List of Symbols and Abbreviations

Symbol	Explanation	Unit
k	Thermal conductivity	W/mK
T	Temperature	°C/K
q	Heat flux	W/m^{2h}
h	Convective heat transfer coefficient	W/m^2K
E	Emissive power	W
α	Thermal diffusivity	m^2/s
σ	Stefan Boltzmann constant	W/m^2K^4
ϵ	Emissivity	No unit
G	Irradiation	W/m^2
h_{bath}	Convective heat transfer coefficient of the bath	W/m^2K
A_{bath}	Area normal to the direction of heat transfer at the freeze-lining/bath interface	m^2
T_{bath}	Bulk temperature of the bath	°C/K
T_f	Temperature of the freeze-lining/bath interface	°C/K
$T_{coolant}$	Temperature of the coolant	°C/K
X_i	Thickness of the furnace wall components	m
X_{fl}	Thickness of the frozen layer	m
k_i	Thermal conductivities of the wall materials	W/mK
A_i	Area of furnace wall section	m^2

k_{fl}	Thermal conductivity of the frozen layer	$\mathrm{W/mK}$
A_{fl}	Area of frozen layer section	$\mathrm{m^2}$
$h_{coolant}$	Convective heat transfer coefficient of the coolant	$\mathrm{W/m^2K}$

Table of Contents

1 Introduction

Titanium is the ninth most abundant element in the earth's crust, occurring in the mineable forms of ilmenite ($FeTiO_3$) and rutile (TiO_2). Rutile is the less common of the two, with a global production of 850 000 metric tonnes per annum (tpa) in 2015 (USGS Titanium Yearbook). Most of the rutile is used in the production of welding rods and titanium metal (Zhang, Zhu et al. 2011). According to the USGS, the global production of ilmenite reached 7.23 million metric tons in 2015, the majority of which is used in pigment production. A more recent study (Bedinger, George M. 2018) puts the global production capacity of TiO_2-pigment 7.3 million tpa, and titanium sponge metal production capacity at 277 000 tpa. China accounts for upwards of 3 million tons of the annual pigment production capacity, and the United States for another 1.36 million tons.

The two predominant processes for titanium dioxide pigment production are the sulphate process and the chloride process. Both processes can utilize high-titania slag as their raw material. (Sahu, Alex et al. 2006a) High-titania slag can be produced by smelting ilmenite concentrate together with a carbonaceous reductant such as anthracite in an electric arc furnace (EAF). The EAF process produces a high-titania slag and pig iron. A freeze-lining of solidified slag on the furnace walls is necessary to optimally operate the smelting process (Pistorius, P. C. 2008). Computer modeling of the process can help understand the governing mechanisms of the process and freeze-lining formation but requires accurate information on slag properties. There is a lack of thermal conductivity values for TiO_2-slag, and this thesis seeks to remedy that.

The primary goal of this thesis is to determine the thermal conductivity of ilmenite smelter slag from room temperature to 1400 °C. The thermal conductivity of the slag directly influences the formation of the freeze-lining on the furnace walls. Accurate knowledge of the thermal conductivity of the ilmenite slag is essential for process control and can improve the quality of simulations that are used to study the smelting

process. Two methods were chosen to conduct this investigation. They are the laser flash analysis (LFA) and the transient plane source (TPS) methods. A secondary goal of the thesis is to compare these two methods and their effectiveness for measuring thermal constants. Both methods are based on using a transient energy pulse, the size of which is quantified. In the case of the LFA this energy takes the form of a short laser pulse which is fired into one surface of the sample, with an infrared sensor reading the heat profile of the back surface. In the TPS method, the energy source is an electrical pulse which is ran through a double spiral. This spiral acts as both the heat source as well as the temperature sensor.

2 Heat transfer in pyrometallurgical systems

This chapter seeks to give a brief theoretical overview of three heat transfer mechanisms, thermal conduction, convection, and radiation. Understanding heat transfer from the molten bath of the ilmenite smelting furnace to the water-cooled furnace walls is required to be able study the formation of the freeze-lining essential to the smelting operation.

2.1 Heat transfer mechanisms

Heat transfer can be defined as thermal energy in transit due to spatial temperature difference (Incropera, Dewitt et al. 2007). There are three main mechanisms of heat transfer: conduction, convection, and radiation. To quantify heat transfer phenomena, so-called rate equations are used. They allow for the computation of the amount of energy being transferred per unit time.

2.1.1 Thermal conduction

Thermal conduction can be defined as the transfer of energy from between the particles of a substance. This propagation of heat is based on the interaction of these particles with each other. The direction of conductive heat transfer is from the more energetic towards the less energetic particles. Thermal energy is related to molecular motion, including internal rotational and vibrational motions as well as random translational motion. These motions cause molecules to interact with each other as they become close in proximity. This interaction leaves the energy levels of both molecules changed: thermal energy transfer has occurred. In gases and liquids, the main mechanism of thermal conduction is molecular or atomic collision.

The molecules in solid substances conform to a lattice structure, but their thermal movement can affect the structure adjacent to them. The propagation of thermal movement through the lattice structure of a solid substance is called lattice vibration. In

solids, the conduction of thermal energy can take place through lattice vibration, the quantifiable units of which are called phonons. (Incropera, Dewitt et al. 2007)

The rate equation for conduction is known as Fourier's law, which for simple one-dimensional conduction in a plane wall can be expressed as:

$$q_x = -k\frac{dT}{dx}, \quad (1)$$

where k is the thermal conductivity (W/m*K) characteristic to the medium, and $\frac{dT}{dx}$ is the temperature gradient in dimension x.

In this thesis, conduction is relevant in both of the experimental methodologies used. Furthermore, the majority of the heat flux out of the ilmenite smelting furnace occurs through the furnace walls. The heat transfer through the wall layers is governed by their thermal conductivities. Thus, accurate knowledge of the material properties, including thermal conductivity, of all the layers is essential for understanding the heat transfer phenomena in ilmenite smelting.

2.1.2 Convective heat transfer

Convection is a mode of heat transfer that is characterized by bulk flow of fluid contributing to heat transfer to and from a surface. The phenomenon itself is comprised of two distinct mechanisms: heat is transferred by both the random molecular motion in as well as the macroscopic motion of the bulk fluid. More precisely, convection is the combination of these two mechanisms, and the transport of thermal energy through bulk flow of fluid is termed advection.

The main interaction happens in the so-called hydrodynamic boundary layer, where the velocity of the fluid flow is zero at the interface between surface and fluid, and gradually increases to a finite value that is characteristic to the flow. At the surface-fluid interface, the heat is transported only through thermal diffusion, as the flow velocity is zero.

Consequently, diffusion dominates the heat transfer near the surface with fluid flow increasingly taking over as the point of scrutiny moves away from the surface.

The rate equation for convection is called Newton's law of cooling, and can be expressed as:

$$q = h(T_s - T_\infty), \quad (2)$$

where q (W/m^2) is the convective heat flux, T_s is the temperature of the surface, T_∞ is the temperature of the fluid, and h (W/m^2*K) is the convection heat transfer coefficient, which is dependent on multiple factors and usually requires experimental determination. In this expression, the heat flux is considered positive when heat is transferred from the surface, and negative when transferred to the surface. (Incropera, Dewitt et al. 2007)

In determining the heat balance of the EAF in ilmenite smelting, and the heat flux through the furnace wall, convective heat transfer plays an important role.

In ilmenite smelting, an electric arc is created in the furnace, causing a large part of the electrical energy to be converted into thermal energy, or heat, which is received by the melt and the furnace walls. This heat is the main input of thermal energy to the system. Thermal energy is lost through the furnace walls, and convective transfer phenomena govern the heat flow from melt to the innermost solid surface in the furnace wall, which ideally will be the freeze-lining. The heat that travels through the wall layers is removed by flowing coolant, once again entering the domain of convection-governed heat transfer.

2.1.3 Radiation

All matter that has a nonzero temperature emits thermal radiation. The emission is caused by changes in the electron configurations of the constituent atoms of the matter. While heat transfer through conduction and convection require a medium for the

energy to propagate, radiation does not. Furthermore, it occurs most efficiently in a vacuum. The thermal energy is transported by electromagnetic waves, the quanta of which are called photons.

An ideal radiator, or blackbody, has the maximum possible emissive power as described by the Stefan-Boltzmann law:

$$E = \sigma T_s^4, \tag{3}$$

where T_s is the absolute temperature of the surface, and σ is the Stefan Boltzmann constant $5.67 * 10^{-8}$(W/m^2 * K^4). However, at the same temperature, a real surface has a lower emissive power than a blackbody, described by:

$$E = \epsilon \sigma T_s^4, \tag{4}$$

where the added term ϵ is a characteristic property of the surface, called emissivity. Emissivity values are between 0 and 1, describing the emissive effectiveness of a surface.

In the case where a surface is subjected to radiative heat transfer, the term irradiation G can be used to describe the amount of radiation incident per unit area of the surface. The rate equation for irradiation of a surface is therefore:

$$G_{abs} = \alpha G, \tag{5}$$

where α is the absorptivity characteristic to the surface, gaining values between 0 and 1. Energy that is absorbed by the surface adds to the thermal energy of the irradiated body. Other surface attributes that affect the effect of an irradiative occurrence are opaqueness and transparency. If the surface is opaque, some of the incoming radiation is reflected. If there is some transparency in the surface, a part of the radiation may be transmitted. Regardless of the amount of opaqueness or transparency, the reflection and transmission of radiation do not affect the thermal energy of the irradiated body. (Incropera, Dewitt et al. 2007)

2.2 Slag freeze-lining in pyrometallurgical furnaces

In the context of pyrometallurgy, a freeze-lining is a frozen layer of slag that protects the refractory material from the molten material inside a furnace. The conditions inside a pyrometallurgical furnace are extreme: in addition to high temperatures, the system is often agitated, and the liquids inside chemically aggressive. The lifetime of refractory linings can be drastically reduced by the combined effect of these factors. Unscheduled breakdowns due to unforeseen refractory degradation add costs to the operation. Furthermore, extending the lifetime of wear-parts reduces operating expenses. (Fallah-Mehrjardi, Hayes et al. 2014)

The heat flux through the furnace wall that is in contact with the molten slag is what determines the formation of an autogenic layer of solidified slag on the refractory surface. Figure 1 below shows a schematic view of the furnace wall layers and heat transfer through them.

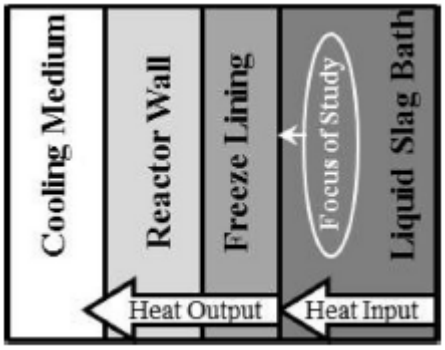

Figure 1 Schematic picture of heat transfer through furnace wall layers (Fallah-Mehrjardi, Hayes et al. 2014)

The thickness and stability of the freeze-lining is dependent on the heat flux through the wall layers. In steady state conditions, the situation can be described in mathematical form as in Equation 6 below (Fallah-Mehrjardi, Hayes et al. 2014):

$$Q_{bath} = Q_{fl} = Q_{wall} = Q_{coolant}, \quad (6)$$

where $\mathrm{Q}_{\mathrm{bath}}$ is the heat flux from the molten bath to the interface between slag and freeze-lining, Q_{fl} the heat flux through the freeze-lining, $\mathrm{Q}_{\mathrm{wall}}$ the heat flux through the furnace wall, and $\mathrm{Q}_{\mathrm{coolant}}$ the heat flux to the cooling medium. The steady-state condition of heat transfer through the furnace wall ($\mathrm{Q}_{\mathrm{bath}}$ being equal to the rate of heat output from the bath/freeze-lining interface to the coolant) can further be described by equation 7 below:

$$h_{bath}A_{bath}\left(T_{bath}-T_f\right)=\frac{T_f-T_{coolant}}{\sum\frac{X_i}{k_iA_i}+\frac{X_{fl}}{k_{fl}A_{fl}}} \tag{7}$$

The area terms cancel out as they are of equal magnitude. Subsequently solving for freeze-lining thickness we acquire the following:

$$X_{fl}=\left(\frac{k_{fl}}{h_{bath}}\right)*\left(\frac{T_f-T_{coolant}}{T_{bath}-T_f}\right)-\left(\frac{k_{fl}}{h_{coolant}}+k_{fl}\Sigma\frac{X_i}{k_i}\right) \tag{8}$$

This posits the thickness of the freeze-lining as a function of the bath superheat, convective heat transfer coefficient of the bath h_{bath}, the mean thermal conductivities of the different layers, and the convective parameters of the cooling medium. (Fallah-Mehrjardi, Hayes et al. 2014)

3 Prior research on thermal diffusivity and conductivity of slags

3.1 Thermal properties of slags and refractories

Metallurgical slags are generally oxide-based mixtures that float on top of a molten metal phase. They have a variety of functions, including impurity control and protecting the melt from oxidation. The slag in the ilmenite smelting process differs from more traditional silicate slags in that it is the primary product of the process, rather than a side-product. This section seeks to compare the thermal properties of slags and refractory materials to create a framework for the study of the thermal conductivity of ilmenite smelter slags.

3.1.1 Silicate slags

Silicate slags are commonplace in pyrometallurgy, present in both steelmaking and copper smelting operations. Thus, their structures and properties have been researched extensively through the decades, with compendiums such as the Slag Atlas (Verein Deutscher Eisenhüttenleute 1995) resulting from the continuous effort to understand them.

The thermal diffusivities of molten silicate-based slags have successfully utilized laser flash technology. (Eriksson, R., Seetharaman 2004). Eriksson and Seetharaman demonstrated that the $\mathrm{CaO} - \mathrm{Al_2O_3} - \mathrm{SiO_2}$ ternary slag system exhibits an increasing effective thermal diffusivity with increasing temperatures in molten form (Figure 2). They also discovered that thermal diffusivity values decreased with increasing cation content in the slag, concluding that this was likely due to their network-breaking effect on the silicate polymer structure.

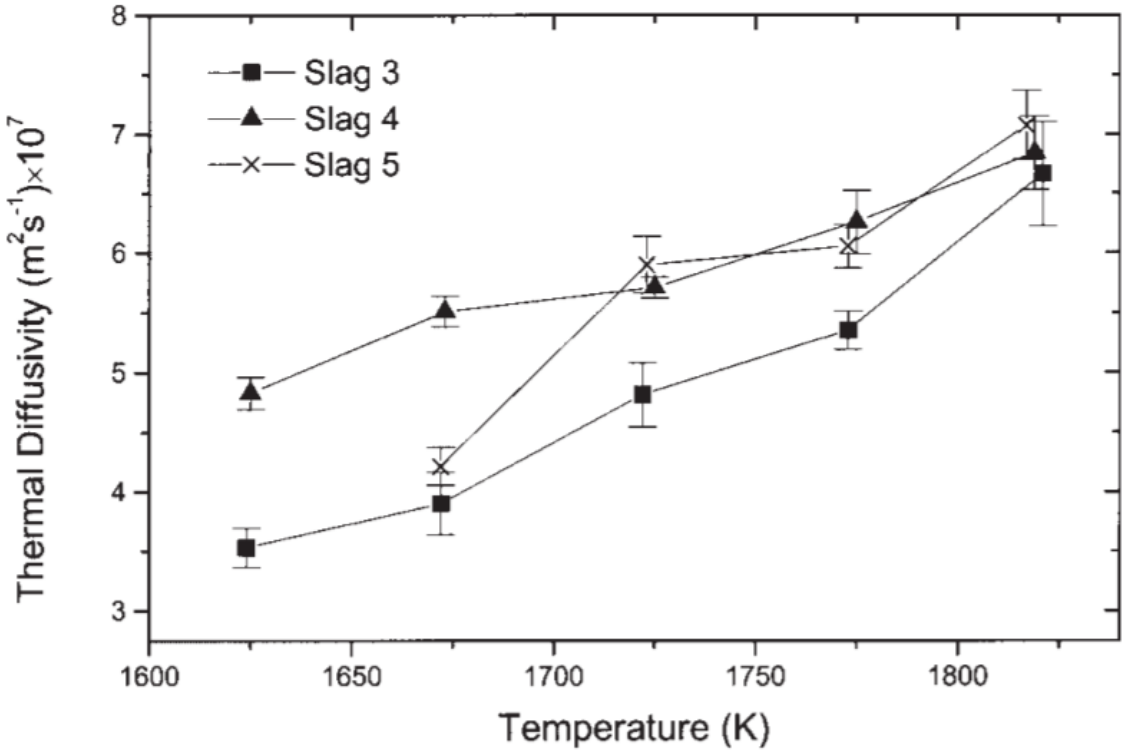

Figure 2 Effective thermal diffusivity as a function of temperature for three different compositions of CaO-Al_2O_3-SiO_2 slags (Eriksson, R., Seetharaman 2004)

It can be generally stated that the thermal conductivity of siliceous slags increases with increasing temperature, with a sharp drop in conductivity once the slag reaches a molten state. An example is shown in Figure 3 below. In liquid form, the siliceous slags conform to a 3-dimensional network, with silicon-oxygen tetrahedra (SiO_4^{-4}) forming the basic structural unit. These units can join to form 3-dimensional structures such as chains and rings. The size of these networked structures in a slag is characterized by its degree of polymerization. The thermal conductivity of liquid silicate slags varies with the degree of polymerization, and it is qualitatively established that the higher the degree of polymerization, the higher the thermal conductivity. This corresponds to the increasing phonon free path resulting from increased polymerization in the slag. The degree of polymerization can be affected by addition of different so-called network breakers, such as FeO, CaO, Na^{2+}, or Fe_2O_3, which decrease the degree of polymerization. (Sun, Pan et al. 2012)

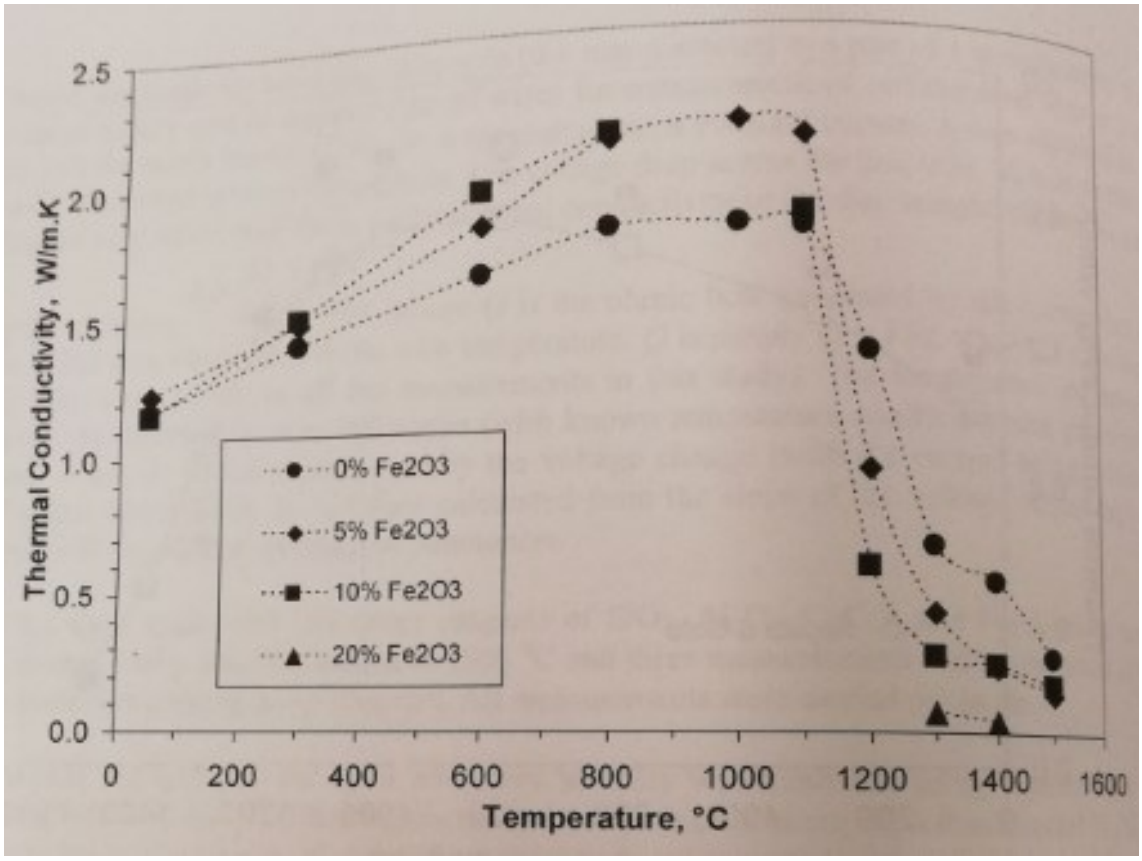

Figure 3 Thermal conductivities of a series of slags with 0, 5, 10 and 20 wt % additions of Fe2O3 to a slag with the composition 40SiO2-20Al2O3-40CaO (all wt %)(Sun, Pan et al. 2012)

An extensive review on the properties of molten slag systems was conducted by Matsushita et al (Matsushita, Watanabe et al. 2011). While the reported thermal conductivity values of molten slags conform to the same order of magnitude, there are some conflicting results regarding their temperature dependence, as is seen in Figure 4 below. Experiments that were conducted with the hot-wire technique showed that thermal conductivity decreases with increasing temperature. Meanwhile, increasing temperatures occasionally brought forth increasing thermal conductivity values when studied with the laser flash method. Thermal conductivity for the $Na_2O - SiO_2$ system was eminently found to reach a maximum of 1.1-1.4 W/mK somewhere between 700 and 1000 K. In many cases, as temperatures were increased the thermal conductivity kept decreasing even after passing the liquidus temperature, reaching 0.1 W/mK (Figure

4). The decrease near after the maximum is thought to possibly be a result of glass transition and subsequent lowering of heat capacity. (Matsushita, Watanabe et al. 2011)

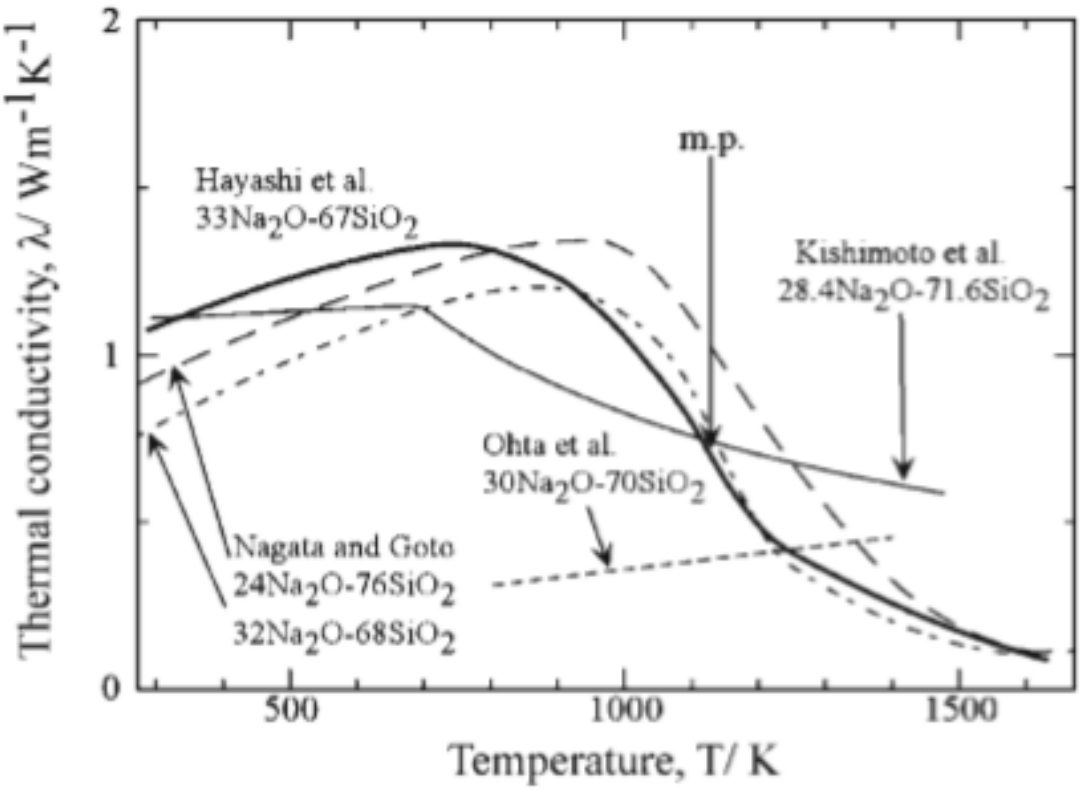

Figure 4 Collection of measurement results of the thermal conductivity of the Na_2O-SiO_2 slag system (Matsushita, Watanabe et al. 2011)

3.1.2 High TiO2 slags

Much of the research seems to have been focused on studying silicate-based slags specifically, whereas this thesis seeks to investigate the high-TiO_2 slag created in ilmenite smelting operations. The factors that govern the properties of these slags are somewhat different. For example, the level of polymerization in the melt is not as important a factor in determining the properties of an ilmenite slag as it is for siliceous slags. Similarly, the compositions in the studied slags are less varied than in some of the silicate studies. This is mainly due to the tendency of TiO_2-rich slags to conform to an M_3O_5-stiochiometry. (Handfield, Charette 1971, Pistorius, P., Coetzee 2003, Pistorius, P.

C. 2004a, Zietsman, Pistorius 2004, Guéguin, Cardarelli 2007, Pistorius, P. C. 2008, Pistorius, P. C. 2012)

The structure of TiO_2-rich slags in EAF smelting operations is drastically different from traditional silicate slags. There are no fluxing additions due to very low impurity tolerances, and the main constituents of the slag originate from the ilmenite feed. The slag composition is typically dominated by titanium oxides (85% $TiO_2 + Ti_2O_3$), with some FeO (10 %) and impurities (the remaining 5 %). Once solidified, the slag can be viewed as a solid solution conforming to pseudobrookite (M_3O_5) stoichiometry, with titanium existing as Ti_3O_5 and $FeTi_2O_5$, and impurities existing in forms such as $MnT_2O_5, MgTi_2O_5, Al_2TiO_5$ and Cr_2TiO_5. (Pistorius, P. C. 2012) No published experimental data on the thermal conductivity of high-TiO_2 slag was found for the literature study except for a previous estimation of 1 W/mK for smelter freeze-lining that has been made in order to conduct calculations (Pistorius, P. C. 2004b).

Viscosity of molten TiO_2-slag is not clearly dependent on temperature, as is with siliceous slags. Instead, the titania-slag stays very fluid if it is fully molten. High-TiO_2 slags have been found to have lower electrical resisitivities than siliceous slags, with increasing TiO_2 content bringing forth increasing specific electrical conductivity. The differences in behavior is likely caused by the structures of the slags. Siliceous slags exhibit polymerization in their molten form, whereas TiO_2-slags are prone to conform to crystalline configurations. (Handfield, Charette 1971)

The electrical conductivity of high-titania slags is much higher than their siliceous counterparts, reaching 6500 S/m (Guéguin, Cardarelli 2007). The specific electrical conductivity of a Al_2O_3-CaO-MgO-SiO_2 quaternary slag systems with varying compositions have been studied by multiple authors (Mills 1995). The compiled results at 1500 °C report conductivities as low as 0.8 S/m and high as 63 S/m.

3.1.3 Refractory Materials

Refractories in the context of process metallurgy are usually ceramic materials that are used to line the insides of furnaces. The material of the refractories is selected based on the demands of the particular process that they are intended for. Common materials include MgO and $\mathrm{Al_2O_3}$, to which materials such as carbon or silica may be added. In ilmenite smelting, magnesia-based refractories are used for their tendency to form solid spinel, chemical formula $\mathrm{Mg_2TiO_4}$, on contact with the slag. This is preferential to the tendency of alumina-based materials to dissolve in the presence of even low amounts of ilmenite slag. (Pistorius, P. C. 2008) The laser flash method was used to study the thermophysical properties of a range of materials in temperatures between room temperature and 1273 K (Min, Blumm et al. 2007). The study found the thermal conductivity of a magnesia carbon refractory material with 20 wt. % carbon content to decrease with increasing temperatures, changing from 25 W/mK to 16 W/mK (Figure 5). The thermal conductivity of both MgO refractory and $\mathrm{Al_2O_3}$ - $\mathrm{SiO_2}$ insulation bricks were examined in another study using the hot wire method at temperatures between 473 and 1473 K (Saito, Kanematsu et al. 2009). The refractory material exhibited an inverse dependence of thermal conductivity to temperature, with measured values ranging between 5 W/mK and 10 W/mK (Table 1). The insulation bricks exhibited a mutual dependence with increasing temperature, with measured conductivities of around 0.5 W/mK.

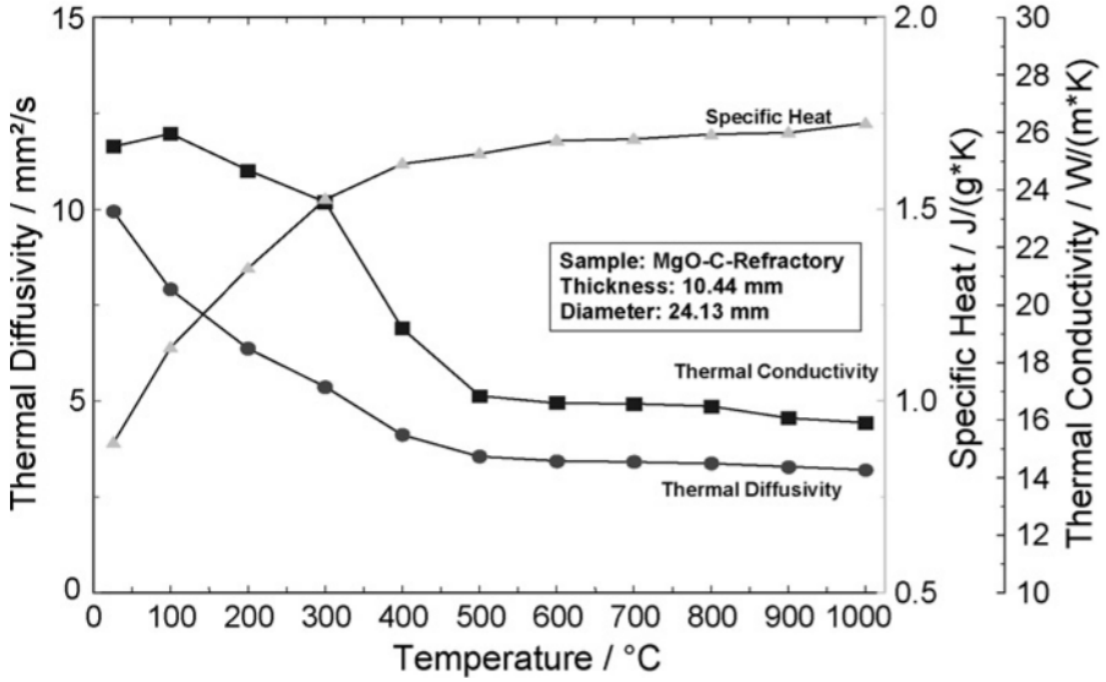

Figure 5 Specific heat, thermal conductivity and thermal diffusivity for magnesia-carbon refractory material (Min, Blumm et al. 2007)

Table 1 Thermal conductivity of magnesia refractory brick determined by hot wire method (Saito, Kanematsu et al. 2009)

Temperature /K	Thermal conductivity /W·m^{-1}·K^{-1}
473	10.1
473	9.4
473	9.7
773	9.6
773	9.2
773	9.8
1273	6.3
1273	6.3
1273	6.5
1473	5.4
1473	5.6
1473	5.6

3.2 Factors affecting thermal conductivity

Several factors have been identified as affecting the thermal conductivity of a given material. These include the structural nature of the sample, porosity and in the case of siliceous slags, the SiO_2-content. (Kenneth C. Mills, Miyuki Hayashi et al. 2014)

The ability of a material to conduct thermal energy is dependent on its structure. The phonon free path tends to be longer the longer the continuous structural units of the material are. For example, in SiO_2-based slags, as SiO_2 content increases, so does the degree of polymerization. This means that the structural units that the material consists of become longer, and the phonon free path increases. A mutual dependence of thermal conductivity with SiO_2-content naturally follows.

Another important structural element that affects a material's thermal conductivity is the grain size. As grain size decreases, the amount of grain boundaries increases. Grain boundaries create a discontinuity in the material, effectively decreasing its thermal conductivity. Discontinuities can also be caused by void spaces in a material. The term

porosity is used to describe the ratio of empty space to bulk material in a sample or material. The more porous a sample is, the less thermally conductive it becomes when compared to the theoretical conductivity of the material itself. An important distinction needs to be made between bulk- and characteristic attributes of a material, as they may differ greatly.

4 Ilmenite smelting production chain

Global production of ilmenite being over 7 million tpa (Bedinger, George, Kohler et al. 2018), its sources include traditional mining as well as mineral sand beneficiation operations. Exploitation of mineral sands is common along the African coast, with rutile and leucoxene being mined as well as ilmenite. Common minerals processing and separation methods include magnetic and gravity methods. (Rozendaal, Philander et al. 2017) Mineral sands do not require as much particle size reduction as whole ore, as they are naturally a smaller particle size.

4.1 Smelting

Ilmenite ore is smelted to separate $\mathrm{TiO_2}$from the mineral. The process inputs are ilmenite concentrate, carbon-containing reductant such as anthracite, and electrical power, which is delivered through graphite electrodes. The concentrate separates into two main molten phases, a molten iron bath and a $\mathrm{TiO_2}$-rich slag. The titania-rich slag is the main product of the ilmenite smelting process. It is tapped periodically to maintain furnace level. The slag is granulated and processed further, while the raw iron can be processed into pig iron or steel. The titanium dioxide is purified further for use as pigment, commonly through a process called chlorination. (Pistorius, P. C. 2008) Another pathway for titanium dioxide pigment production exists in the sulphate process, which is suitable for less pure slags. The smelting process will be discussed in more detail in Chapter 5.

4.2 Chlorination

The chlorination process accepts synthetic rutile as well as high-titania slag as feedstock. The process operates at a temperature of 900-950 °C, obtaining titanium tetrachloride $\mathrm{TiCl_4}$. Chlorination is most commonly performed in a fluidized bed, where the two main reactions (9,10) are depicted in the formulae below. (Zhang, Zhu et al. 2011)

$$\mathrm{TiO_2(s) + 2Cl_2(g) + 2C(s) \rightarrow TiCl_4(g) + 2CO(g)} \quad (9)$$

$$\mathrm{TiO_2(s) + 2Cl_2(g) + C(s) \rightarrow TiCl_4(g) + CO_2(g)} \quad (10)$$

The $\mathrm{TiCl_4}$ is then separated by selective distillation, and further processed to form pure $\mathrm{TiO_2}$. The chlorination process demands a relatively high-quality slag as feedstock, as impurities can disrupt the process. For example, the oxides MgO and CaO react to form $\mathrm{MgCl_2}$ and $\mathrm{CaCl_2}$ in the chlorination reactor. These divalent chlorides have their boiling points below the operating temperature of the chlorination process, and can accumulate in the bed, causing problems. (Pistorius, P. C. 2008)

4.3 The Sulphate Process

The sulphate process utilizes strong sulphuric acid to digest high-$\mathrm{TiO_2}$ slag according to Equation 11 below. The process can also use sufficiently upgraded ilmenite ore as feedstock.

$$\mathrm{FeTiO_3(s) + H_2SO_4(l) \rightleftharpoons FeSO_4(s) + TiO_2(s) + H_2O(l)} \quad (11)$$

The ferric sulphate is reduced to ferrous sulfate by adding metallic iron. Ferrous sulphate can then be crystallized as $\mathrm{FeSO_4 \cdot 7H_2O}$ by cooling the bath, and subsequently separated. Further processing entails boiling the solution to precipitate $\mathrm{TiO_2}$ and heating to about 1000 °C, removing remaining water and driving the formation of fine crystallized raw pigment. The sulphate process requires relatively low capital investment and has low energy consumption. However, its main disadvantage is the large number of byproducts such as ferrous sulphate that are produced. (Sahu, Alex et al. 2006b)

5 Ilmenite smelting

5.1 Electric arc furnace

Ilmenite smelting takes place in an electric arc furnace. The furnace can be either alternating current or direct current operated. The basic reactions in ilmenite smelting involve the carbon-driven reduction of $\mathrm{TiO_2}$ to $\mathrm{Ti_2O_3}$ and FeO to metallic Fe, as described by reactions 12 and 13, respectively, below (Pistorius, P. C. 2008). The metallic Fe makes its way to the iron bath, while metallic oxides remain in the slag

$$\mathrm{TiO_2} + \frac{1}{2}\mathrm{C} \rightarrow \mathrm{TiO_{1.5}} + \frac{1}{2}\mathrm{CO} \tag{12}$$

$$\mathrm{FeO} + \mathrm{C} \rightarrow \mathrm{Fe} + \mathrm{CO} \tag{13}$$

The extent of these reactions determines the slag composition. Both reactions occur partially, but (13) proceeds further, with optimal slag FeO content lying around 10% by mass or below. Conversely, the ratio of $\mathrm{TiO_2}$ to $\mathrm{Ti_2O_3}$ varies. For example, in the samples investigated in this thesis, it ranges from approximately 2 to 1, with total $\mathrm{TiO_2}$-equivalent content around 75-90%. Figure 6 below depicts a liquidus diagram for the $\mathrm{FeTiO_3 - TiO_2 - Ti_2O_3}$ -system. The temperature of the high-titania slag in the ilmenite smelting process is around 1600-1700 °C, with target FeO-content below 10%. As can be seen from Fig- 6, the melting point of the slag rises as the FeO-content is reduced by furthering the reduction reactions in the furnace.

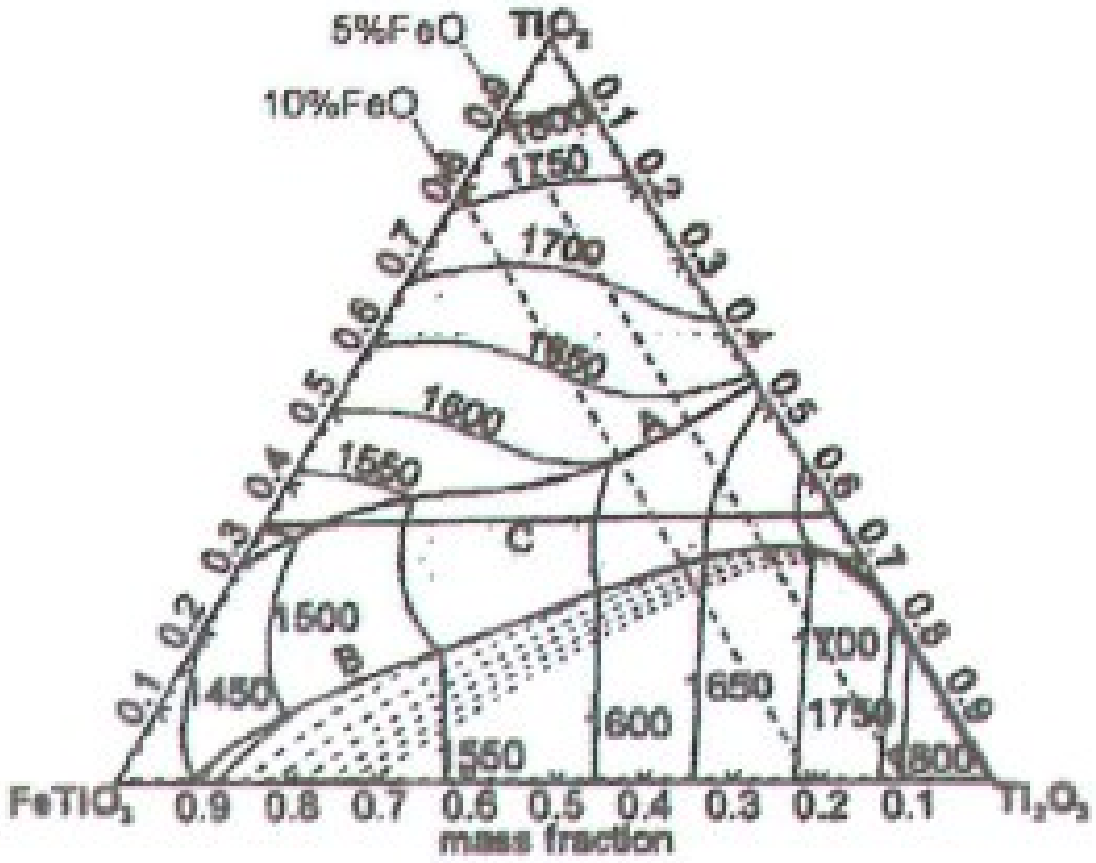

Figure 6 Calculated liquidus diagram of ilmenite smelter slags (Pistorius, P. C. 2008)

5.1.1 Titania-rich slag

The primary phases in solidified titania-rich slag are rutile (TiO_2) and pseudobrookite (M_3O_5). Pseudobrookite comprises a three-component system $FeO - TiO_2 - Ti_2O_3$, manifesting as a solid solution of $FeTi_2O_5$ and Ti_3O_5 (Pistorius, P. C. 2004a). Real slags contain more than these three elements, and the M_3O_5 stoichiometry is present in two forms, $M^{2+}(Ti^{4+})_2O_5$ and $(M^{3+})_2Ti^{4+}O_5$. In this form, titanium is tetravalent, and both divalent (Fe^{2+}, Mg^{2+} and Mn^{2+}) and trivalent (Ti^{3+}, Cr^{3+}, $Al^{3+}$and V^{3+}) metallic ions can be accommodated. Common impurities further include silica, which tends to report to separate minor phases, occasionally with some of the Al_2O_3 in the slag. (Pistorius, P., Coetzee 2003)

From a thermodynamic point of view the M_3O_5 phase is unstable below 1350 °C (Pistorius, P., Coetzee 2003), as compounds of titanium and oxygen with degrees of oxidation between Ti_3O_5 and TiO_2 take prevalence. The formation of these so-called Magnéli phases (general formula of Ti_nO_{2n-1}, where n ≥ 4, illustrated in Figure 7 below)(Eriksson, G., Pelton 1993) is however slow, and in practice, the titania-rich slags solidify in M_3O_5 configuration (Pistorius, P., Coetzee 2003).

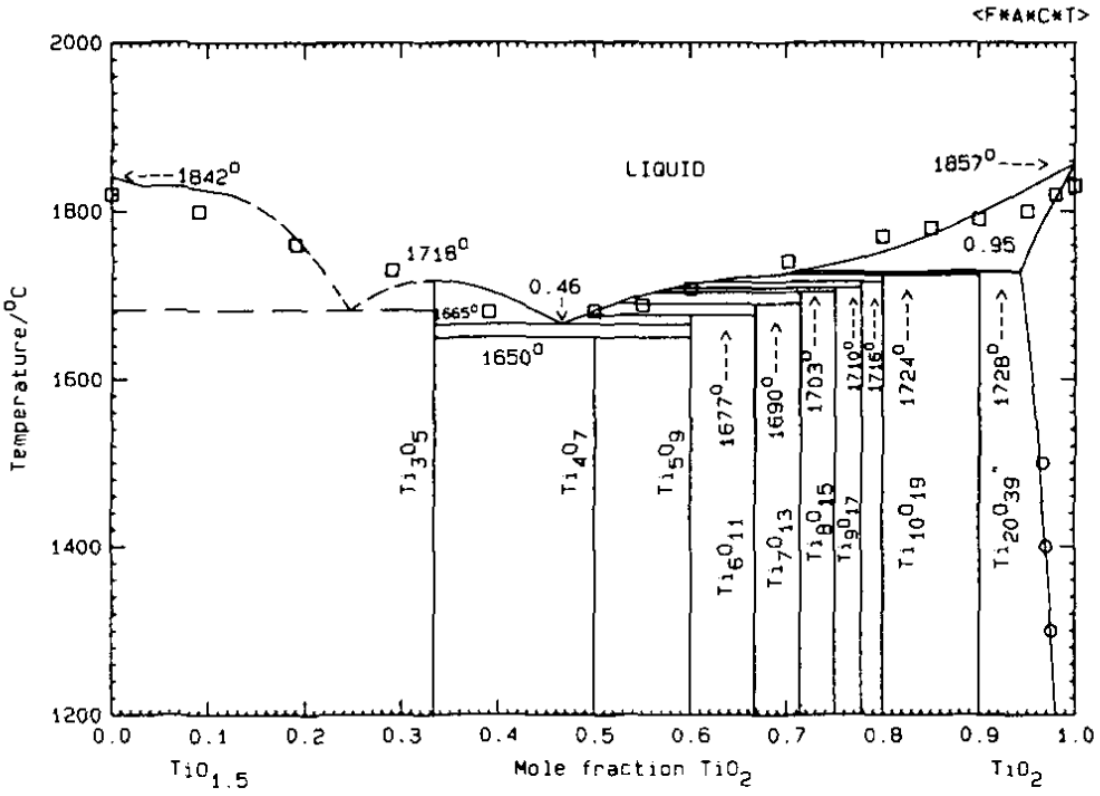

Figure 7 Ti2O3 - TiO2 phase diagram with Magnéli phases (Eriksson & Pelton, 1993)

5.1.2 Freeze-lining in ilmenite smelting

The deliberate formation of a freeze-lining on the furnace wall can be a useful solution to the problem of refractory erosion in any pyrometallurgical furnace. In the case of ilmenite smelting, it is of critical importance. The TiO_2-slag product has a low tolerance

for impurities, and any dissolved refractory material is unwanted. Thus, there are both a general economical and a process-specific incentive to optimize freeze-lining formation in ilmenite smelting operations. (Pistorius, P. C. 2008)

The enthalpy change for the solidification of the ilmenite slag was thermodynamically calculated by Pistorius (Pistorius, P. C. 2004b) and shown to be remarkably high compared to the heat capacity of the slag: the heat of solidification corresponds with a temperature change of over 600 °C of fully liquid slag. This means that the formation of a freeze-lining greatly affects the heat balance of the furnace. In the same study, the ilmenite and reductant feeds of the test furnace were shut off while energy input was continued. The temperature began to slowly climb, but the large heat of solidification kept the change relatively modest. Once the freeze-lining was completely dissolved, the temperature began to climb more aggressively. Thus, the presence of a freeze-lining of solidified slag seems to contribute to the stability of temperature inside the ilmenite smelting furnace.

Furthermore, the ilmenite smelter slag has relatively narrow solidification range of around 30 K (Pistorius, P. C. 2004b), affected among other factors by the FeO-content of the slag. The behavior of the solidus-liquidus gap in relation to iron oxide content (here depicted as fraction of $\mathrm{FeTi_2O_5}$ in a $\mathrm{M_3O_5}$-structure) is demonstrated in Figure 8 below (Pistorius, P., Coetzee 2003). The formation of a freeze-lining in the ilmenite smelting process is thus a precarious process, with many variables involved.

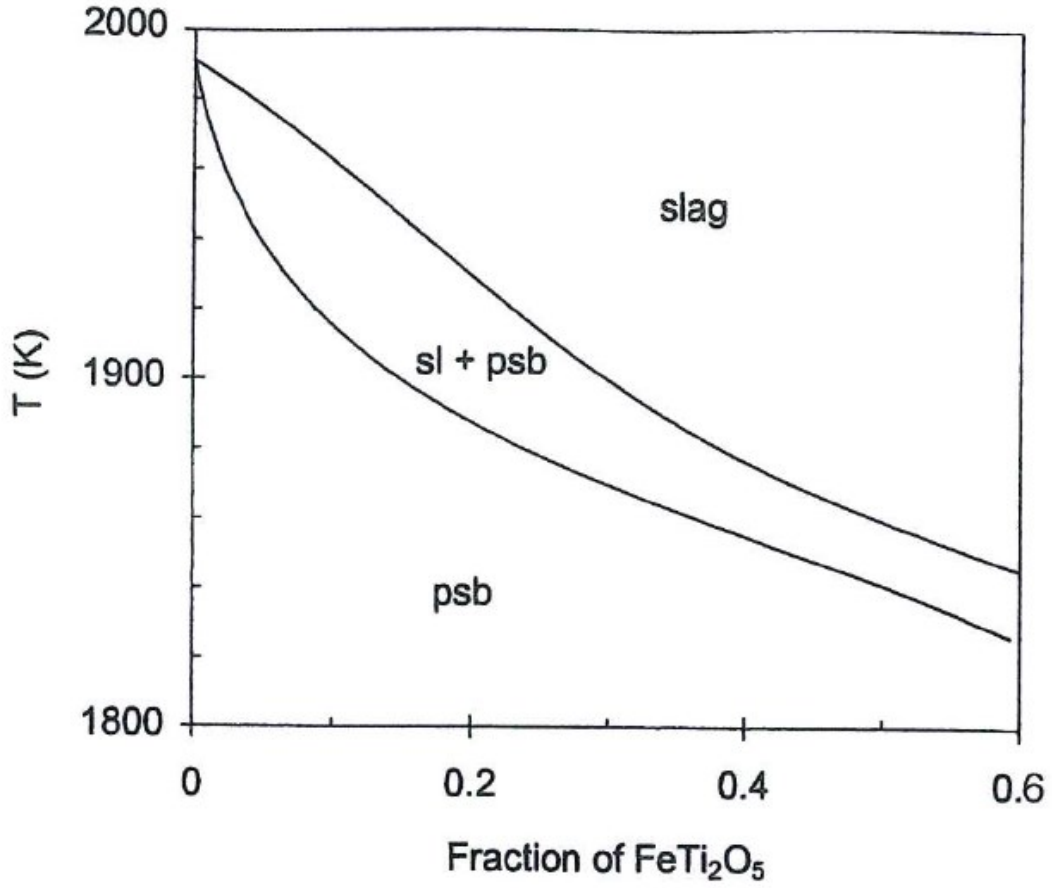

Figure 8 Behavior of the solidus-liquidus gap of ilmenite slag in relation to the fraction of $FeTi_2O_5$ (Pistorius, P., Coetzee 2003)

5.2 Process control variables

There are three main inputs to the EAF in ilmenite smelting: electrical power input and feed rates of ilmenite and reductant. The composition and temperature cannot be controlled independently. One reason is that the formation of freeze-lining is necessary for good operation. This is because the high-titania slag aggressively dissolves the magnesium-containing refractory bricks if their contact is not limited. If temperature is increased, cooling circulation needs to increase to maintain the freeze-lining. In other words, optimal process parameters would keep the molten slag temperature close to the slag melting point.

The balance between carbon (reductant) and power input is delicate, and if one changes, the other must be adjusted accordingly. If they are not matched, the process can destabilize. As an example, insufficient carbon input leads to the freeze-lining melting as temperatures rise, exposing the refractory to the aggressive slag. Similarly, if the energy input is too small in relation to the carbon input, the temperature will go down in the slag phase. In practice, this can result in either freeze-lining growth, or more seriously, precipitation of solidified pseudobrookite in the slag. This precipitation can cause uncontrolled slag foaming: this is because there is a sharp increase in the apparent viscosity of ilmenite slags just below their liquidus. (Pistorius, P. C. 2008)

6 Experimental

6.1 Experimental materials

The experimental materials were a selection of industrial and synthetic slags (X2, R2 and K19) and an excavated freeze-lining (T1). The chemical compositions of the materials are described in Table 2 below. Sample T1 was not analyzed for chemical composition. Sample X2 has a high TiO_2-equivalent content and represents an ilmenite slag with high purity with high degree of FeO reduction. Sample K19 has a high TiO_2-equivalent content, and higher FeO-content than X2, but fewer total impurities. Sample R2 has a higher amount of impurities than either of the other slag samples, and notably, a much lower degree of reduction of TiO_2 to Ti_2O_3. Table 2 below contains the chemical analyses of the sample materials.

Table 2 Chemical analyses for experimental samples. *analyzed as V_2O_5

Species	X2	R2	K19	T1
TiO2_eqv	90.57	77.06	87.60	N/A
Ti_2O_3	39.48	16.36	33.62	N/A
FeO	3.22	10.03	8.07	N/A
Fe_m	0.11	0.30	0.44	N/A
MgO	2.55	4.78	1.39	N/A
Al_2O_3	1.91	2.14	1.61	N/A
CaO	0.25	0.57	0.10	N/A
TiO_2	46.70	58.88	50.21	N/A
V_2O_3	0.25	0.43	0.28*	N/A
Cr_2O_3	0.45	0.15	0.14	N/A
MnO	1.10	0.31	1.49	N/A
SiO_2	1.04	1.72	0.84	N/A

6.2 Sample preparation

For the experimental part of this thesis, different methods of investigation were used. The methods had different requirements for the sample dimensions and additional preparations. The sample preparation procedures are described in this section.

6.2.1 Transient Plane Source

The slag samples were provided as 20 mm diameter drilled cores. The optimal dimensions for the Hot Disk measurements were determined to be a cylindrical disc with minimum 16 mm diameter and 6 mm thickness. Discs of 6.5-8 mm thickness were sawed from the drill cores with a low speed rotary saw. The amount of irregularities in the samples was minimized to ensure measurement accuracy.

6.2.2 Dilatometry

Rod-shaped samples were prepared with a low speed rotary saw. First, blocks of lengths of 10-20 mm length were sawn from the original drill cores. The core was fastened to the saw, and three cuts were made without moving the core. Cutting off a thin slice and then proceeding to saw the blank for the dilatometer without detaching the sample ensured that the cut surfaces were parallel to each other. A series of cuts could then be made to fashion a small rod. The ready samples were then dried in a furnace at 120 °C to ensure evaporation of any water from the sawing process. A ready-made dilatometer sample before the experiment is depicted in Figure 9 below.

Figure 9 Dilatometer sample of slag K19. Ruler for scale.

6.2.3 Laser Flash Analysis

A core drill bit with the required diameter of 12.7 mm was used to acquire blanks for sawing. These blanks were then sawn with a low speed saw, into approximately 2 mm thick slices. These slices were dried in a furnace at 120 °C to ensure evaporation of any left-over moisture from the drilling and sawing processes. Some of the samples had an appreciable amount of porosity, which needed to be filled. A mixture of fine silicon carbide powder and water was used to fill the pores to achieve a flat surface. Figure 10 below shows both an unfilled and a smoothened sample. Once a sample had a flat surface on both circular faces, thin layers of graphite were sprayed on both surfaces. Both the smoothness and blackness of the surface were necessary to ensure the quality of the result of the laser flash experiments. For the measurements of sample material X2 at Netzsch, a drill core of 12.6 mm diameter was used, and a single sample of approximately 4 mm thickness was sawn.

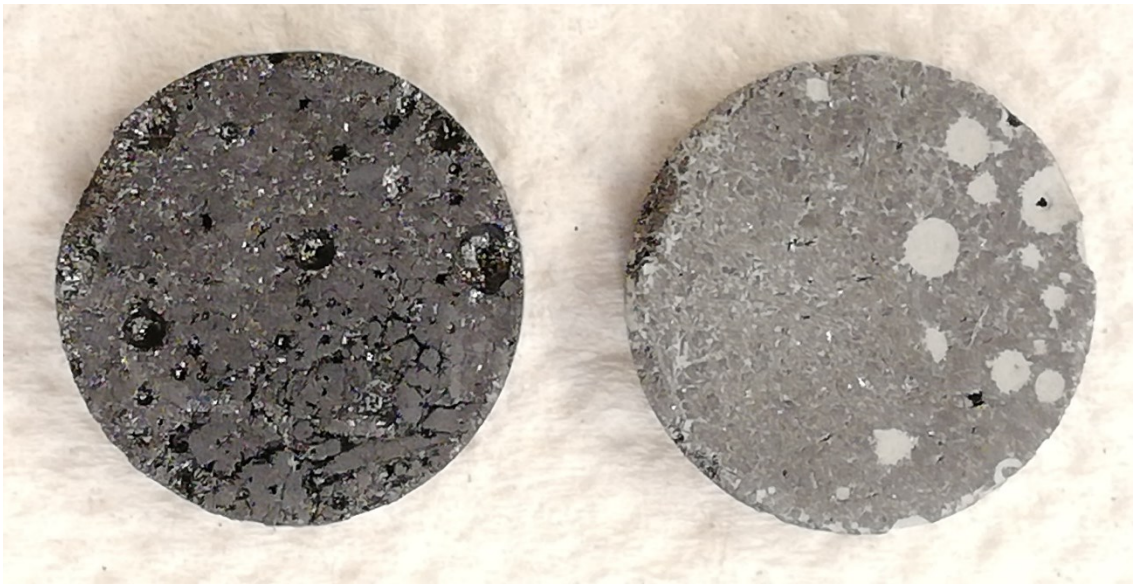

Figure 10 Samples of slag R2 naked (left) and with silicon carbide filling (right).

6.3 Experimental methods

This thesis seeks to utilize two different kinds of transient methods to determine thermal conductivity for a selection of TiO_2 slags. The experimental methodologies are the Hot Disk instrument, also called the transient plane source (TPS) method, and the laser flash analyzer (LFA). Inorganic, inhomogeneous metal compounds have been investigated with similar methods in the recent past. In her doctoral thesis, Miettinen used both the TPS and LFA methods to study the thermal conductivities of sulfate aggregates from copper flash smelting waste heat boiler walls (Miettinen 2008). Similarly, Ksiazek utilized the LFA method in temperatures up to 1000 °C, as he studied the thermal properties of ferromanganese ores in his dissertation. (Ksiazek 2012).

6.3.1 Transient Plane Source

A Hot Disk 2500 S TPS instrument (Figure 11) was used to determine thermal conductivity and diffusivity for slag samples in the temperature range from room temperature to 400 °C. The sample holder is presented in Figure 12. The TPS method is based on the hot disk sensor, a flat double spiral that is placed between specimens of

sample material. The disk acts as both the heat source and the temperature sensor in the experiment. As a pulse of electrical current is passed through the sensor, the change in resistance is recorded, and the temperature change in the disk is measured. The thermal conductivity and diffusivity of the sample material can be computed from the acquired values. The probing depth high limit for the TPS tests was set at 5 mm to ensure the quality of the results.

The time-dependent electrical resistance of the sensor $R(t)$ is expressed below:

$$R(t) = R_0(1 + c_t\overline{\Delta T(\tau)}), \tag{14}$$

where R_0 is the initial resistance and c_t is the sensor's temperature coefficient of resistivity. The term $\overline{\Delta T(\tau)}$ denotes the mean temperature increase in the sensor and can be expressed as:

$$\overline{\Delta T(\tau)} = \frac{P_0}{\sqrt{(\pi^3)}r\lambda} D(\tau), \tag{15}$$

where P_0 is the total power output of the transient, λ is the thermal conductivity of the sample material, and $D(\tau)$ is a dimensionless time function. The dimensionless time

$$\tau = \sqrt{\frac{t}{\theta}}, \tag{16}$$

where t is the real time of the measurement, includes the time scale θ, also referred to as the characteristic time of the transient recording. The characteristic time is defined as:

$$\theta = \frac{r^2}{\alpha}, \tag{17}$$

where r is the radius of the outer concentric circle of the Hot Disk sensor and α is the thermal diffusivity of the sample.

With the assumption that all heat is transported through a solid specimen, we can state that:

$$\alpha = \frac{\lambda}{\rho C_P}, \tag{18}$$

where ρC_p is the sample's specific heat across a volume unit. (Gustafsson 1991)

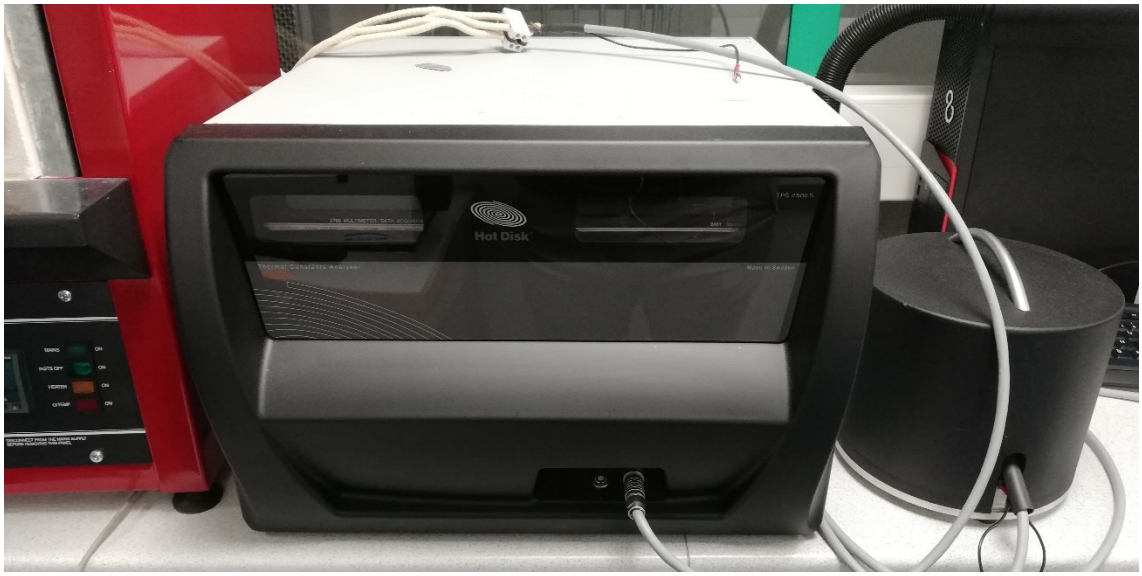

Figure 11 The Hot Disk TPS 2500 S instrument

Figure 12 The sample holder for the Hot Disk system

6.3.2 Dilatometry

The Netzsch 402E is a standard horizontal push-rod dilatometer. The dilatometer is used to determine the thermal expansion characteristics of the material. This data used to apply correction the LFA measurements. The test uses a rod cut from the measured material (maximum dimensions 8x8 mm). The default length of sample for the dilatometer is 50 mm. The dilatometry samples were of varying lengths, and one or more alumina distance pieces were used to accommodate for the sample sizes. Figure 13 below shows the sample holder of the dilatometer, with a slag sample and distance pieces. The dilatometry runs all used similar parameters: the temperature range was from room temperature to 1150 °C, the heating rate was 2 °C/min and atmosphere was argon.

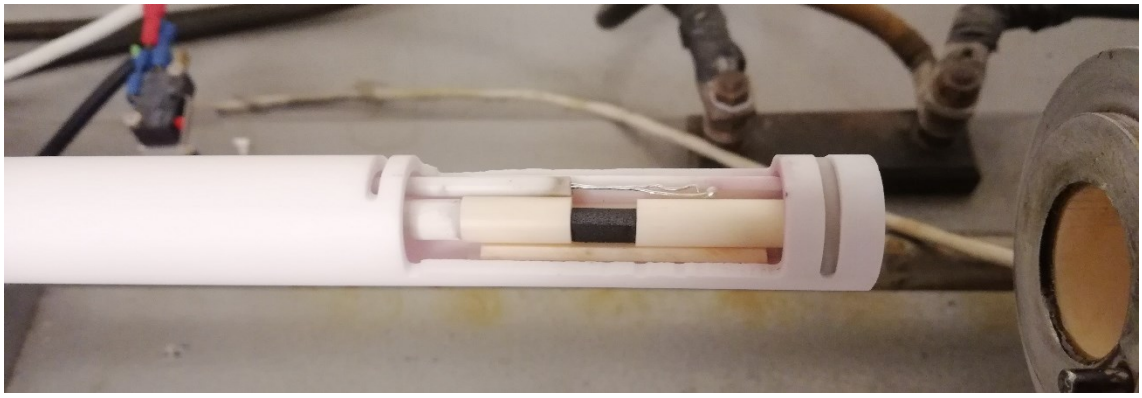

Figure 13 Slag sample and distance pieces in sample holder of the Netzsch 402E dilatometer.

6.3.3 Laser Flash Analysis

The flash method is an experimental technique for determining thermal diffusivity, heat capacity, and thermal conductivity of a sample first described in 1961 (Parker, Jenkins et al. 1961). In the procedure, a high-intensity light pulse is directed at forward surface of a thermally insulated specimen, and the resulting temperature change is measured at the back surface using a thermocouple. In laser flash analysis the energy pulse is delivered by laser. Thermal diffusivity can be determined from the temperature versus time curve, heat capacity by the maximum temperature reached, and thermal

conductivity by computing heat capacity, thermal diffusivity and density. In the experimental part of this thesis, a Netzsch LFA 457 instrument (Figure 14) was used for measurements from room temperature to 1100 °C. The experiments were conducted in a nitrogen atmosphere, and the heating rate was 100 °C/30 min.

Determining thermal diffusivity α from the experimental data is done through the relation:

$$\alpha = \left(\frac{0{,}48L^2}{\pi^2 t_{\frac{1}{2}}}\right), \tag{19}$$

where L is the thickness of the specimen, and $t_{1/2}$ the time required for the posterior surface of the specimen to reach half of the maximum increase in temperature. The mathematical basis for the expression is given elsewhere (Parker, Jenkins et al. 1961).

Figure 14 The Netzsch LFA 457 laser flash analyzer with sample holder exposed.

7 Experimental Results

7.1 Hot Disk measurements

It was not possible to equip the measurement apparatus with an inert atmosphere. This means that all samples oxidized to some degree during the measurements. Although oxidation is not likely to be very aggressive at the temperature range in question, it will unquestionably have altered the results to some degree. Past research indicates that decrepitation of high-titania slags is present at 400 °C, and this could be the cause for the sharp reduction in thermal conductivity for K19 at 400 °C. (Bessinger 2000) The results are presented in Figure 15 below. Some measurements were made in room temperature with Kapton sensors, denoted as HDRT. For the measurements from room temperature to 400 °C, mica sensors were used, denoted as HDM.

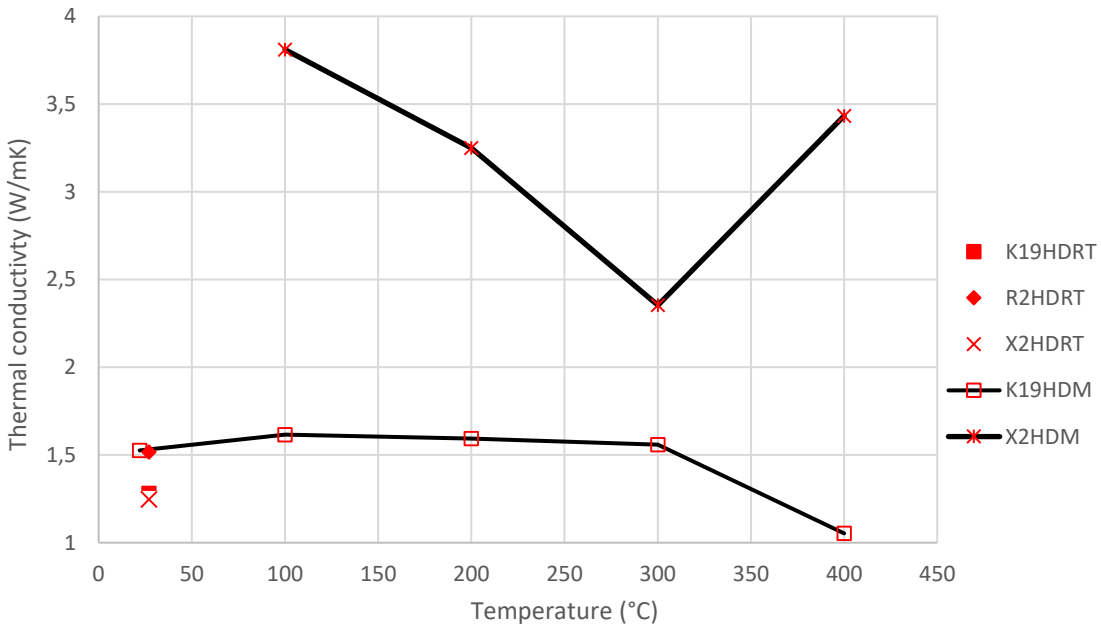

Figure 15 Thermal conductivities measured with TPS method.

7.2 Laser flash experiments

This section presents the results of the laser flash experiments. The experiments were conducted in two stages. The first stage, measuring conductivities between room temperature and 1100 °C, took place at NTNU in Trondheim, using SINTEF's equipment. For experiments closer to and beyond the melting point of the slags, measurements were ordered Netzsch. The limitations of the experimental setup led to the limitation of these ordered measurements to one temperature point for a single sample. In practice, measurements close to and above the melting point of the slag would have consumed a new crucible for every single repetition of the measurements. For financial reasons, measurements close to or beyond the slag melting point were not pursued.

7.2.1 Room temperature to 1400 °C

Four samples were analyzed with LFA from room temperature to 1100 °C. Two of the LFA measurement series (X2 and K19) used two samples with the third space in the apparatus occupied by a reference piece. The two others (R2 and T1) used three samples in all the sample holder slots. Measurements were taken at room temperature and 100 °C, and at 100-degree intervals from then on. Three measurements were taken for each sample at each temperature. The heating rate of the LFA furnace between temperatures was 100 °C/30 min. Additionally, sample X2 was measured separately at 1400 °C. One sample was prepared, and four consequent measurements were made. Measurement results were averaged and plotted over the temperature range. The results are combined in Figure 16 below.

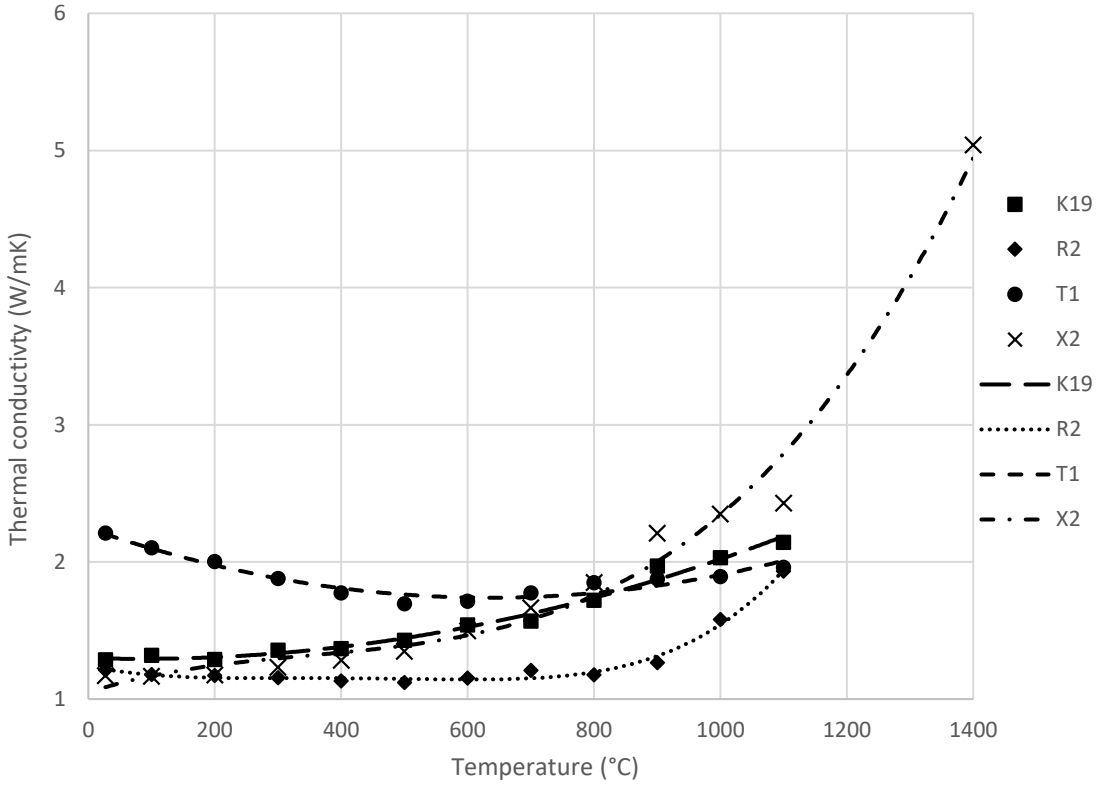

Figure 16 Combined thermal conductivity data from LFA analysis of samples K19, R2, X2 and T1.

For materials K19, R2 and X2, the behavior was similar at low temperatures, and above 800 °C. Thermal conductivity stayed relatively stable until 400 °C, with a conservative increase with increasing temperatures up until 800 °C. A large increase in conductivity is observed to occur after heating the materials past 800 °C. Especially materials R2 and X2 exhibit this behavior, with K19 displaying a more stable relationship between temperature and thermal conductivity. However, even in K19 there is a disproportionate increase from 800 °C to 900 °C.

The T1 material exhibits a different kind of behavior, with conductivity at room temperature being the highest in this temperature range. The conductivity started to decrease with increasing temperature up until about 500 °C, where the change reversed itself. From then on, the thermal conductivity rose with increasing temperatures. The

decrease of thermal conductivity is nearly linear from room temperature to 500 °C. From 500 °C to 1100 °C the conductivity continued to increase.

7.3 Scanning Electron Microscopy

SEM samples were prepared of materials K19, R2, X2 and T1. Taken images were analyzed with energy-dispersive X-ray spectroscopy (EDS) to identify the phases present in the samples. Selected SEM images are shown here. More images can be found in the Appendix.

7.3.1 Sample R2

Figure 17 represents an overview of the material. Figure 18 shows a section of the material in higher magnification. An oxide matrix is the largest phase present, containing mainly titanium and oxygen. The glassy phases, represented in darker gray, consist mostly of silicon and oxygen, with trace amounts of aluminum, calcium, titanium and iron. Metallic droplets seem to be situated preferentially inside the glassy phases. The droplets chiefly contain iron and varying degrees of sulphur and oxygen.

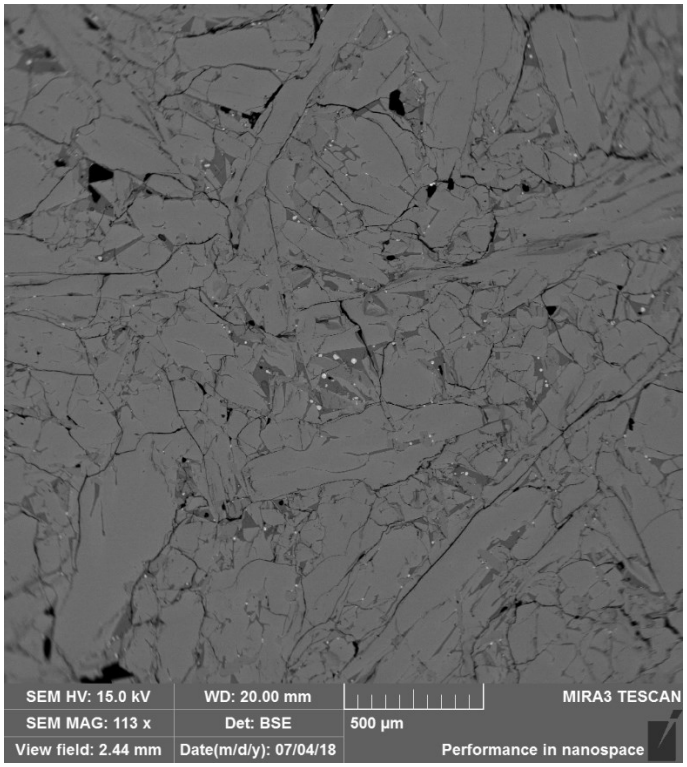

Figure 17 Overview of sample R2

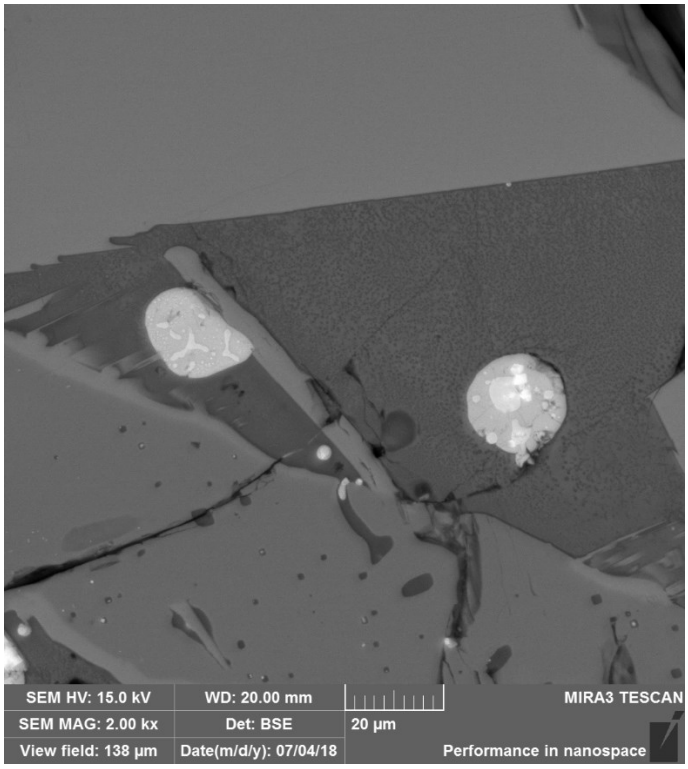

Figure 18 Section of sample R2 in higher magnification

7.3.2 Sample X2

Figures 19 and 20 represent an overview and a highly magnified section of sample X2, respectively. The sample has exhibits circular pores, and prolific micro-cracking. The material is dominated by an oxidic phase, which contains mainly titanium and oxygen, with some magnesium, aluminum and iron also present. Siliceous phases are locked inside the main oxide matrix and contain some titanium and aluminum in addition to silicon and oxygen. The siliceous phases appear to occasionally contain small droplets of the main oxide phase.

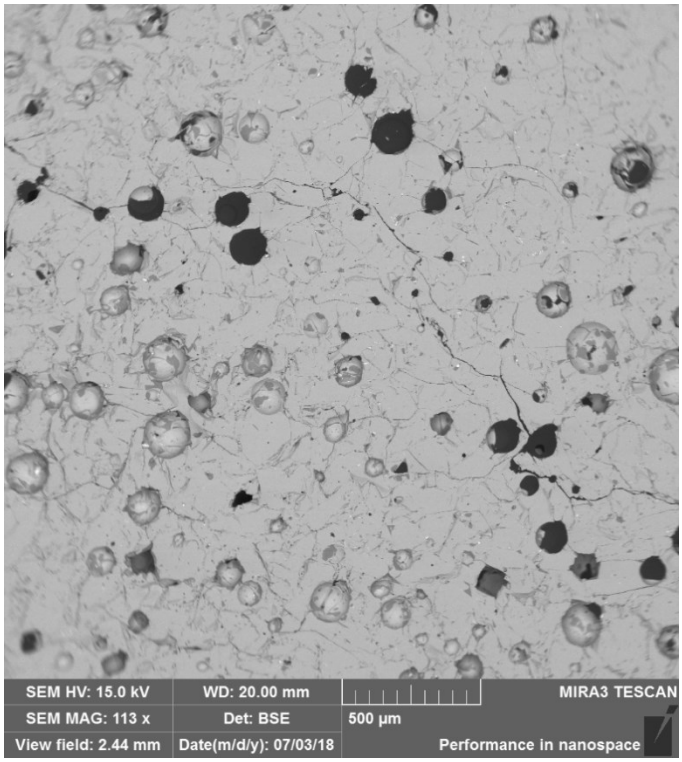

Figure 19 SEM overview of sample X2

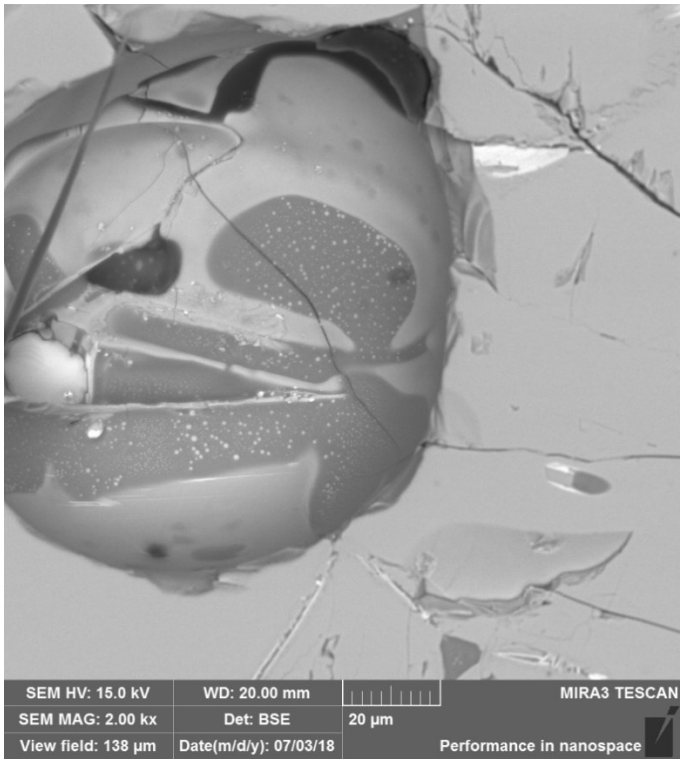

Figure 20 High magnification SEM image of sample X2

7.3.3 Sample K19

Figure 21 below is an overview of the K19 material, and Figure 22 shows a closer magnification of the same site. The macrostructure is blocky with a dominant oxidic phase, containing mostly oxygen, titanium, and iron. Long cracks are present with some more isolated porosity in the oxide matrix. Silicate droplets can be seen entrained inside the oxide matrix. Figure 22 illustrates how there are smaller oxide droplets entrained inside the silicate phase. Metallic phases are present as individual droplets as well as entrained in the silicate phase, occasionally forming spiky lamellae. The metallic phases contain mostly iron, occasionally accompanied by dissolved sulphur originating from the anthracite feed.

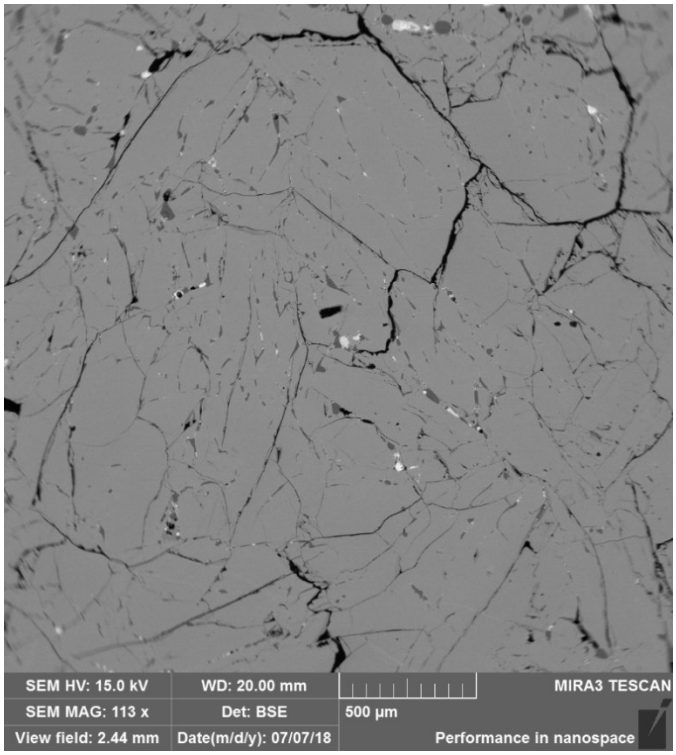

Figure 21 SEM overview of slag K19

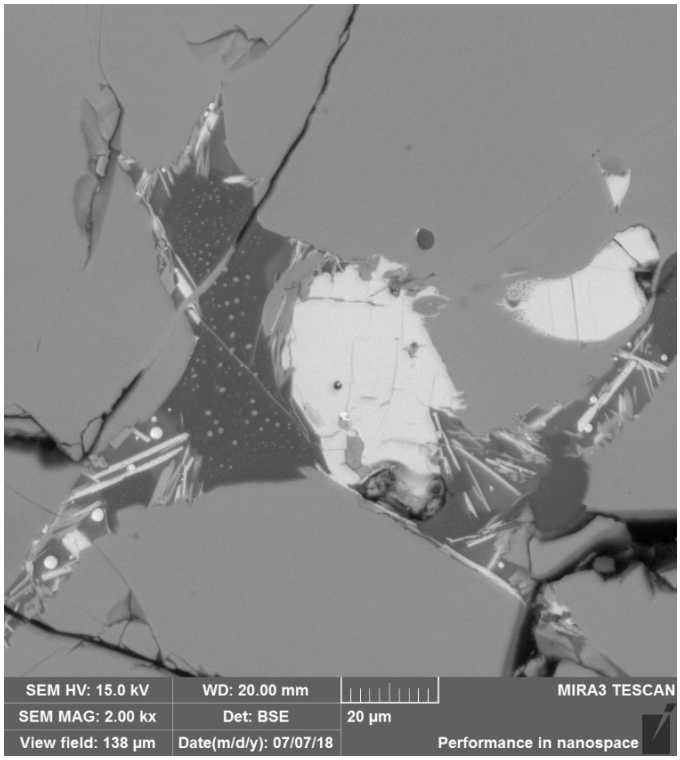

Figure 22 High-magnification SEM image of sample K19

7.3.4 Sample T1

Image 23 below shows the general structure of the T1 material, and image 24 is a section of the same area, in higher magnification. From the overview image, the structure can be seen to comprise mostly directionally oriented lamellae, with a moderate amount of porosity. The main oxide matrix is composed mainly of titanium oxides, with magnesium an important constituent. Small inter-granular glassy phases and metallic droplets are also present, as visualized by the more magnified image. The glassy phases consist mostly of oxygen and silicon, with appreciable amounts of aluminum. The metallic phases contain iron, zinc, and sulfur.

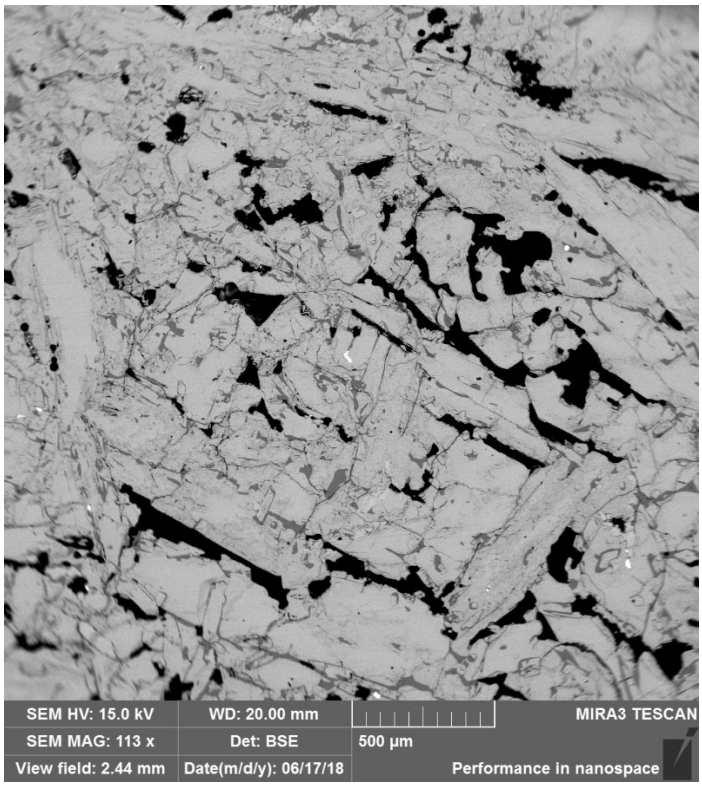

Figure 23 SEM overview of sample T1

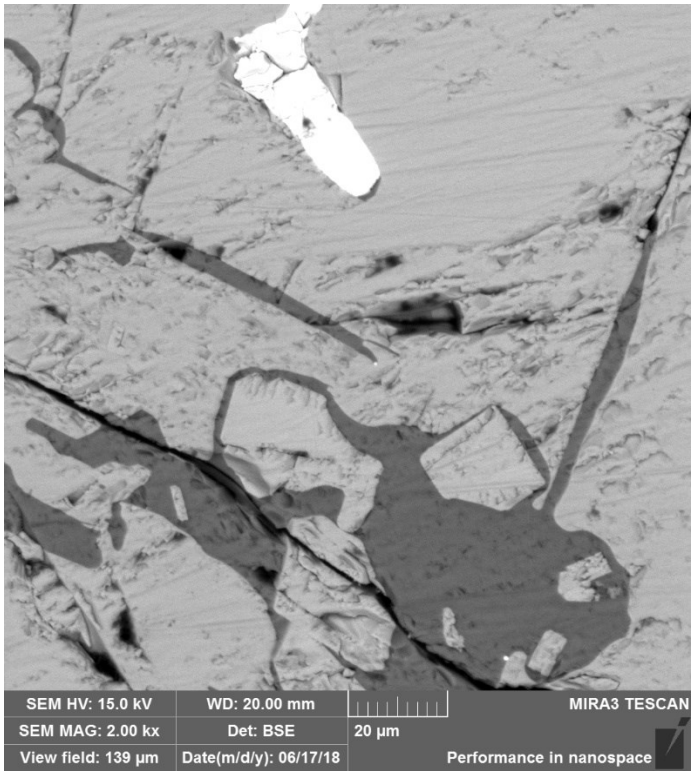

Figure 24 Higher magnification SEM image of sample T1

7.4 Computerized Tomography

Computerized tomography (CT) scans were taken of the LFA sample specimens of sample T1 (shown in Figure 25 & 26). A localized proliferation of metal droplets can be seen on the samples. Cracking is visible throughout the sample. Porosity appears to manifest itself as both crevasses and more bubble-shaped faults. The structure appears to have a crystalline nature, with lamellar formations of the main oxide matrix.

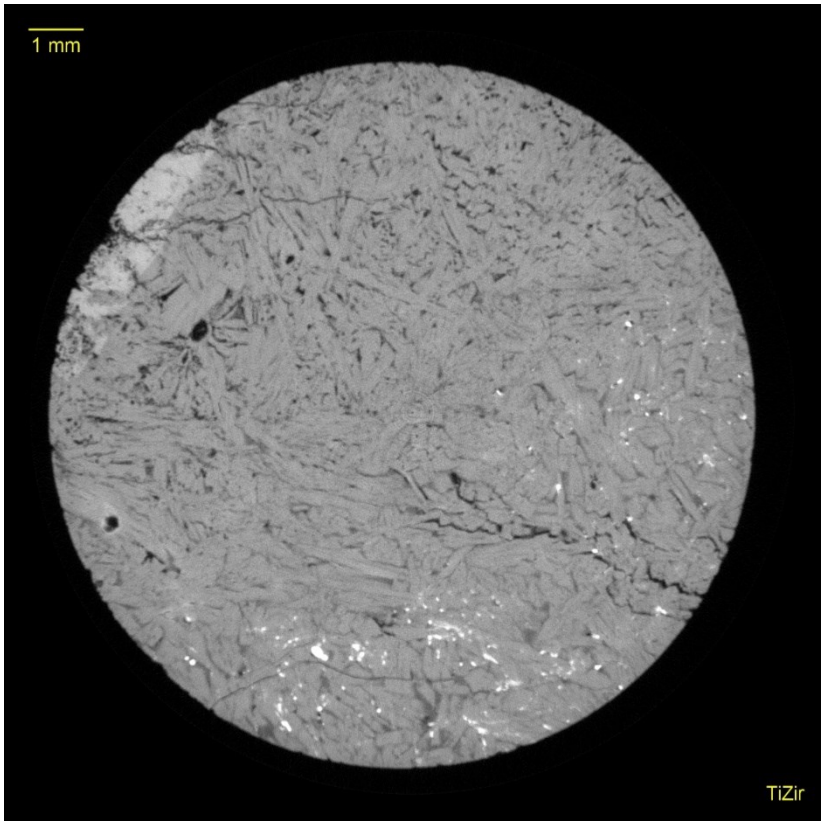

Figure 25 CT image of sample T1 LFA sample specimen

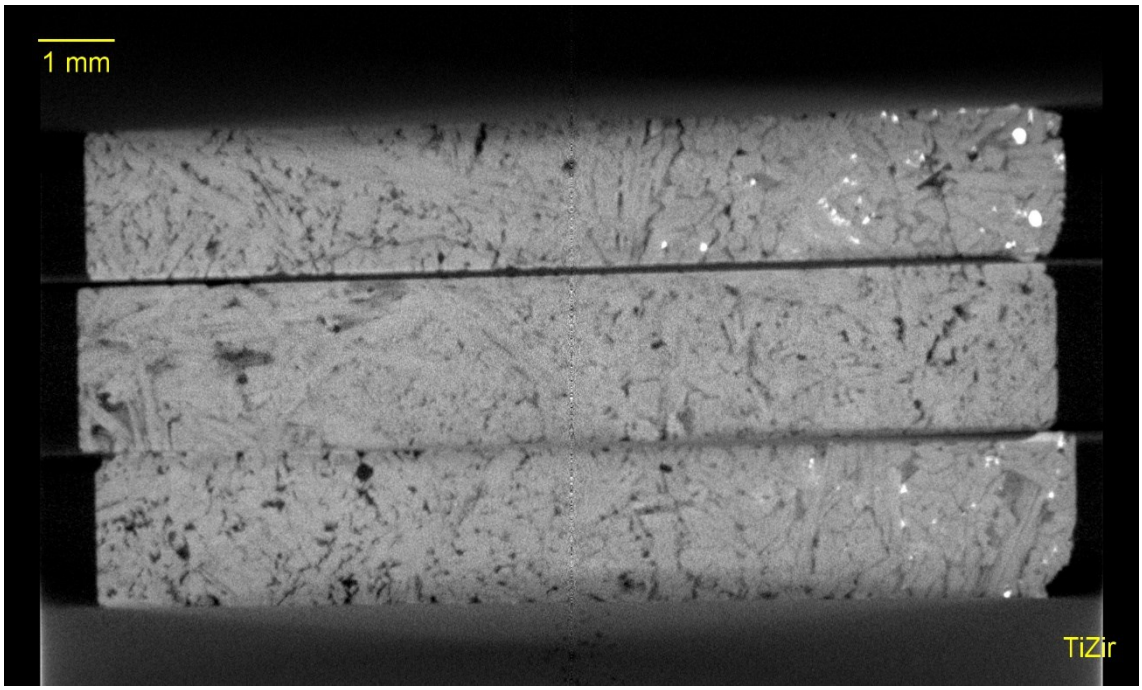

Figure 26 Cross section CT image of sample T1

8 Discussion

The thermal conductivity of three different slags and one excavated freeze-lining samples was measured. The combined results from both the LFA and TPS measurements are compiled in Figure 27 below. The results of the LFA measurements showed differences in behavior between the slag and freeze-lining samples. The freeze lining's composition was expected to differ from the composition of tapped slag. The reasons for this include the observed entrainment of larger metal droplets in the freeze-lining, as well as the partial dissolution of the refractory material to the freeze-lining. The general microstructure in all samples is crystalline with a dominant titanium-bearing oxide matrix making up the bulk of the material. The crystallinity of the material lends itself well to heat transfer through lattice vibrations.

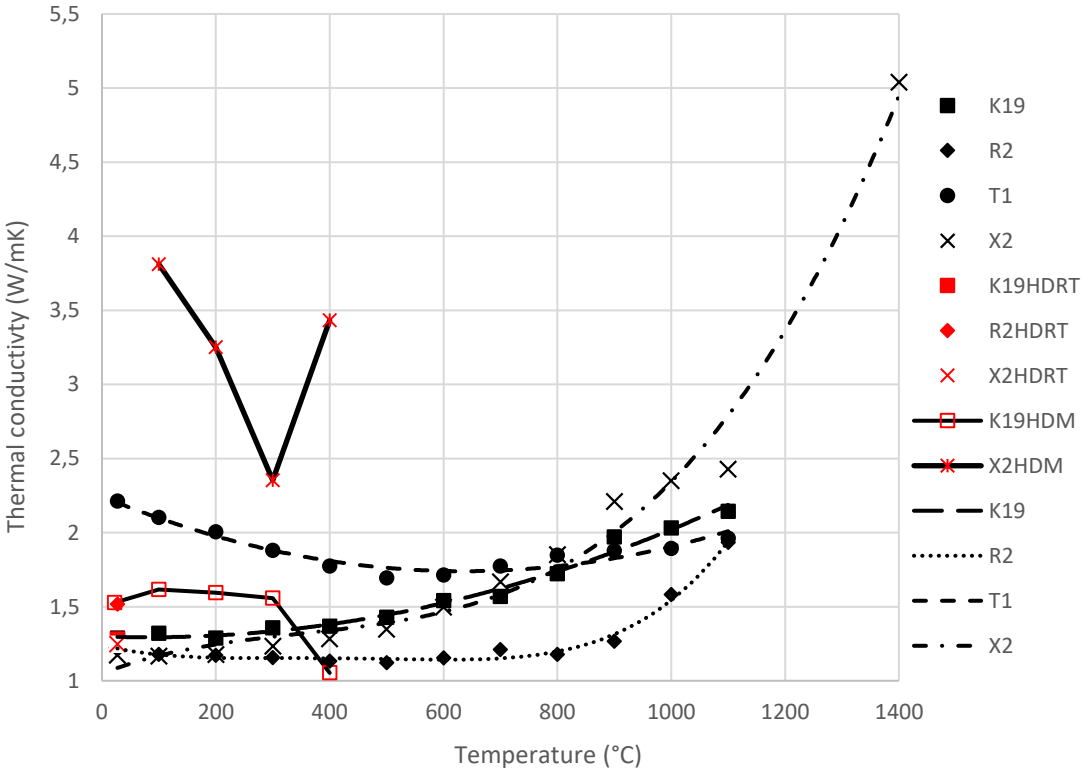

Figure 27 Combined thermal conductivity measurements. The lines are meant to guide the eye.

Samples K19 and X2 exhibited the most similarity in the general trend of the LFA measurement results. Their compositions are also closest to each other, especially in regard to the titanium oxides and the ratio of Ti^{3+} to Ti^{4+}. The slags' structures are visibly different, however. Although both have the oxidic matrix as the main structural element, the pores in sample K19 are mainly long cracks that are some distance from each other. Some of the smaller cracks are partially filled with siliceous deposits. Conversely, the cracks in X2 appear much smaller although more numerous, and the main pores are circular in shape. The siliceous deposits in both samples are similar in that there seem to be small droplets of the main oxide phase dispersed throughout the deposits. In both samples, metallic phases seem to coincide with silicate phases, and exhibit spiky lamellar shapes inside the silicate area.

The X2 slag was re-melted to facilitate sample preparation, and some bubbling was reported to have occurred in the crucible. This bubbling is the likely cause of these spherical pores. Another noteworthy characteristic of the bubbles is that most of the metallic and glassy constituents of the sample seem to be concentrated on the inside surface of these pores, which are visible as circular depressions in the SEM image.

The thermal conductivity of samples K19 and X2 is likely affected mostly by the thermal conductivity of the main oxide phase, which constitutes upwards of 90% of both sample materials. The second most important factor is thought to be the shape and size of the pores. The longer and wider cracks evident in the K19 sample are creating sharper discontinuities in the material than the spherical bubbles of X2. The depth of the cracks and overall prevalence of either of these structural faults cannot be fully assessed from the SEM images. However, following the previous statements, it can be proposed that regarding the thermal conductivity of these samples, the nominal degree of porosity may not be as important as the nature of the pores themselves. This argument is strengthened somewhat by the measured results, as X2 reaches a higher conductivity than K19.

Lattice vibrations can propagate around spherical pores equally well from all directions, but cracks and crevices can impede their movement more. The vibrations must circumvent the cracks, but depending on the direction of the propagation, the distance required can be much longer in relation to the absolute size of the crevice. Although a crevice running parallel to the propagation of lattice vibration will be much easier to circumvent than a bubble, if a crack runs perpendicular to the direction of the heat transfer, the phonon-path must change direction. Additionally, cracks do not consume as much space as spherical bubbles, and as such, that there can be numerically more cracks than bubble-shaped discontinuities in the bulk of a solid material. This is further exacerbated the smaller the crevices are. Furthermore, as is evident in the SEM imagery, the cracks in these materials are not unidimensionally orientated. This configuration of differently sized and dimensionally oriented crevices causes a high probability of phonon interference and contributes to the thermal resistivity of the sample material.

Sample X2 underwent additional LFA testing at 1400 °C, reaching a thermal conductivity of 5 W/mK, meaning that the thermal conductivity continued to rise by rising temperature. By this result it may be predicted that the other slags may behave similarly. The value of 5 W/mK itself is more than double that of the thermal conductivity of sample material X2 at 1100 °C. Furthermore, the thermal conductivity increases approximately 2,6 W/mK in a temperature interval of 300 °C, whereas the change of thermal conductivity from room temperature to 1100 °C is 1,2 W/mK. This indicates that the thermal conductivity of the slag may be even higher at temperatures close to the melting point. However, the effect of melting on the thermal conductivity of the slag is yet unconfirmed. Silicate slags often display this type of behavior. On the other hand, their tendency to polymerize sets them apart from the TiO_2-slag.

The behavior of sample R2 was slightly different from the other two slags, as the thermal conductivity did not immediately begin to rise with the increase in temperature. This could be caused by the marked difference in Ti^{3+}/Ti^{4+} -ratio compared to the other two slags. A comparison of SEM images shows that sample R2 also exhibits more cracking

than either of the two other slag samples, as well as the presence of additional pores. The nature of the cracks is not as wide as the ones of K19, but they are more numerous. As cracks impede lattice vibration, it may be that this structural factor may be the cause of the lesser thermal conductivity of R2 throughout the temperature range. Both the siliceous and metallic phases in the sample display a marked degree inhomogeneity. Inside the metallic phases there are consolidations of as many as three phases with different densities.

Sample T1 differs from the three other samples as it is not a slag, but excavated freeze-lining. A crucial difference from a characterization standpoint is that no compositional analysis for the material was made. However, the sample contained large droplets of metallic iron, visible to the naked eye. Their size in proportion to the samples used for the TPS method made the material unsuitable for testing with the Hot Disk. However, LFA samples were prepared from a section of the sample material that did not contain these large droplets.

The SEM investigation of sample T1 shows a crystalline structure of titanium-bearing oxide material, with small metallic and siliceous sites dispersed throughout the sample. The material is quite porous, more so than any other sample. Most pores are irregularly shaped. The amount of cracking appears to be small, with many crack-like areas being filled with a siliceous deposit.

The thermal conductivity of sample T1 behaved differently than the other three samples. At room temperature the thermal conductivity is approximately double that of the other samples and begins to decrease as temperature is increased. Iron metal has a thermal conductivity of around 80 W/mK at room temperature, which is in a different order of magnitude than the measured conductivities in this work. It can be speculated that the relatively high thermal conductivity of iron metal contributes to the conductivity of the freeze-lining material, which appears to contain more metallic iron than the slag samples. Furthermore, the thermal conductivity of iron metal is inversely proportional

to temperature, as is shown in Figure 28 below. The conductivity decreases to around 40 W/mK by 550 °C (Shelton 1934). This could explain why the thermal conductivity of the sample decreases with increasing temperature up to about 500 °C. The subsequent increase in thermal conductivity with increasing temperature could then be explained by the characteristic behavior of the titanium bearing oxide matrix that makes up most of the sample, as the thermal conductivity of the small amount of iron in the material continues to decrease. The value does not rise as high as the others at 1100 °C, possibly due to its higher porosity.

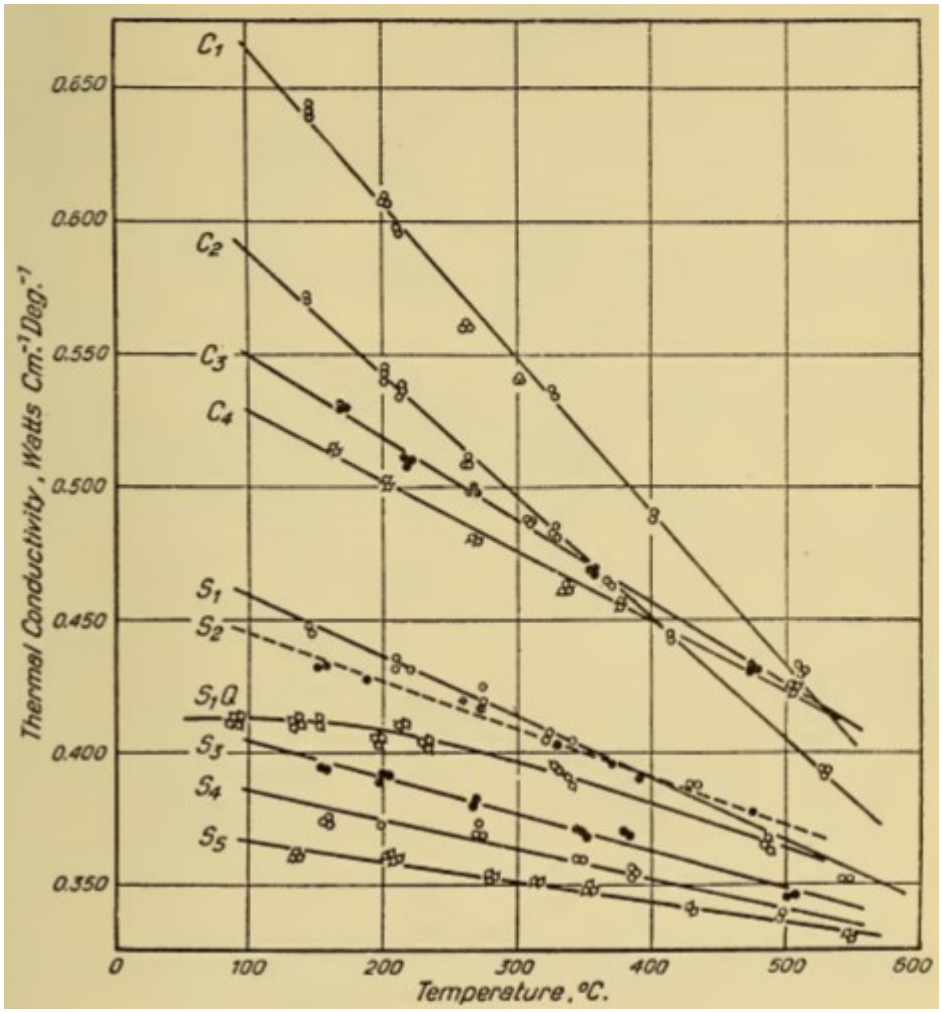

Figure 28 Thermal conductivity of 99.9% iron (line C_1) (Shelton 1934)

Each sample exhibited a degree of porosity, although the types of pores varied. The effect of macroscale porosity on the bulk thermal conductivity of the tested materials could not be determined, because the LFA method utilized very small samples. However, the fact that both the excavated freeze-lining and the slag samples exhibited some degree of pores would indicate that their presence is a constant when considering freeze-linings in ilmenite smelting. Thereby it could be hypothesized that the real thermal conductivity values of a freeze-lining could be different than what the slag itself might suggest.

In the light of these results, Pistorius' estimate of 1 W/mK thermal conductivity for the smelter freeze-lining (Pistorius, P. C. 2004b) may need re-evaluation, as the heat flux from the bath through the layers of the furnace wall is greater than estimated. The freeze-lining likely has a similar thermal conductivity as the refractory lining of the furnace. From an industrial standpoint, this simplifies the operation of an ilmenite smelter, as the formation of a freeze-lining does not have as great an effect on the heat flux through the furnace wall as previously thought.

The effect of freeze-lining formation on the heat flux through the furnace wall depends on the thermal conductivity of the freeze-lining. For example, MgO refractories have a thermal conductivity between 4.5 and 6.5 W/mK in 1000 °C according to prior research (Min, Blumm et al. 2007) (Saito, Kanematsu et al. 2009), with an inverse relationship to temperature. Let us assume that the thermal conductivity of the refractory continues to decrease as temperatures reach the 1700 °C typical of ilmenite smelters. It could be estimated that the thermal conductivity of the refractory wall is between 1 and 4 W/mK at 1700 °C. The exact value notwithstanding, this is still less than the measured value of solid TiO_2-slag at 1400 °C. Thus, when considering the required changes to cooling parameters caused by freeze-lining formation from the perspective of heat transfer, the change in the total thermal resistivity of the furnace wall layers will be less than if the refractory lining was simply made thicker.

An additional aim in this study was to compare the LFA and TPS methods for determining thermal conductivities. It is difficult to pass definite judgement due to experimental differences, such as the inability to use an inert atmosphere in the TPS measurements. Additionally, the smaller physical sample size of the LFA method allowed for selection of a more uniform sample. This leads to questions about how representative of the bulk material the samples are. Nevertheless, some information is better no information at all.

From a practical perspective, it was more challenging to conduct a successful measurement with the TPS method than the LFA method. This is mostly due to the need to change sensors between measurements, and the occasional sensor failure due to their consumable nature.

9 Error analysis

9.1 Laser Flash Analysis

The LFA 457 Laser Flash Analyzer has an error margin of ±3% in measuring the thermal diffusivity of samples according to the manufacturer. The error for the heat capacity is ±5%.

9.1.1 Sample T1

The LFA measurement results from room temperature to 1100 °C for sample T1 are presented in Figure 29 below. The material exhibits good repeatability of measurements. The variation between repeated measurements is generally smaller than the variation between different samples, which speaks for the precision of the LFA measurements. The samples behave similarly throughout the measured temperature range.

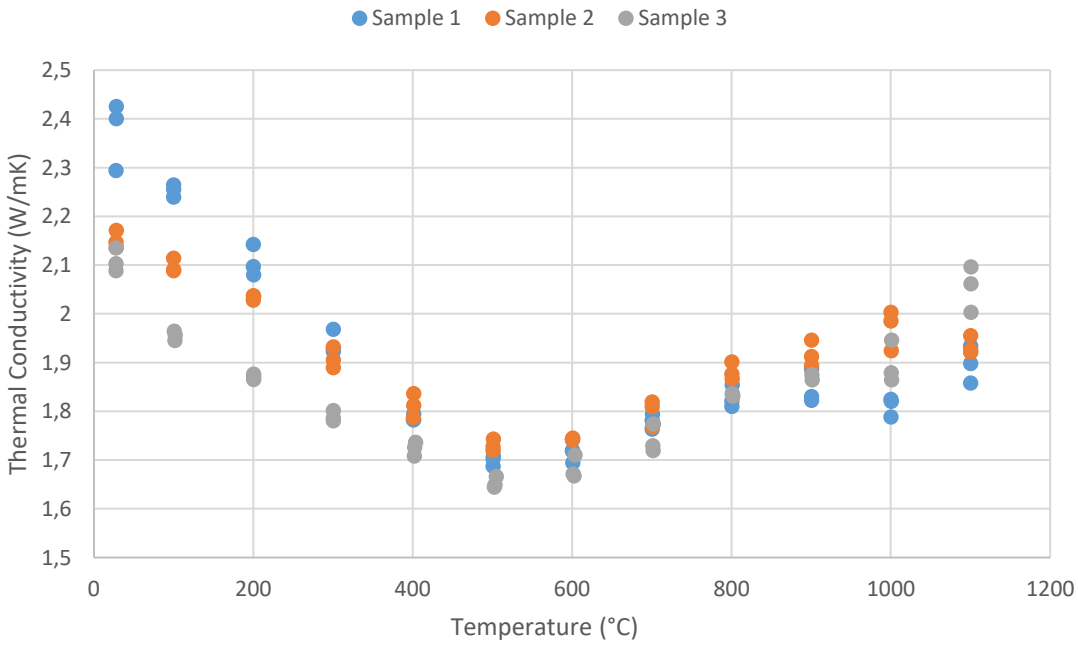

Figure 29 Repeat measurements of sample T1.

9.1.2 Sample X2

The LFA measurement results from room temperature to 1100 °C for slag X2 are denominated with sample 1 and sample 2 in Figure 30 below. The repeated measurement values for thermal conductivity for each sample are reasonable closely spaced. The repeat measurement points for the same sample are close to each other, even when there is some variability between samples, as is seen between 400 °C and 800 °C. Samples 1 and 2 behave highly similarly throughout the measured temperature range. Sample 3 was sent to Netzsch for measurement at 1400 °C. There is some quite some variance in the value, but if the measurement point with the lowest value is disregarded as an outlier, the grouping is much tighter.

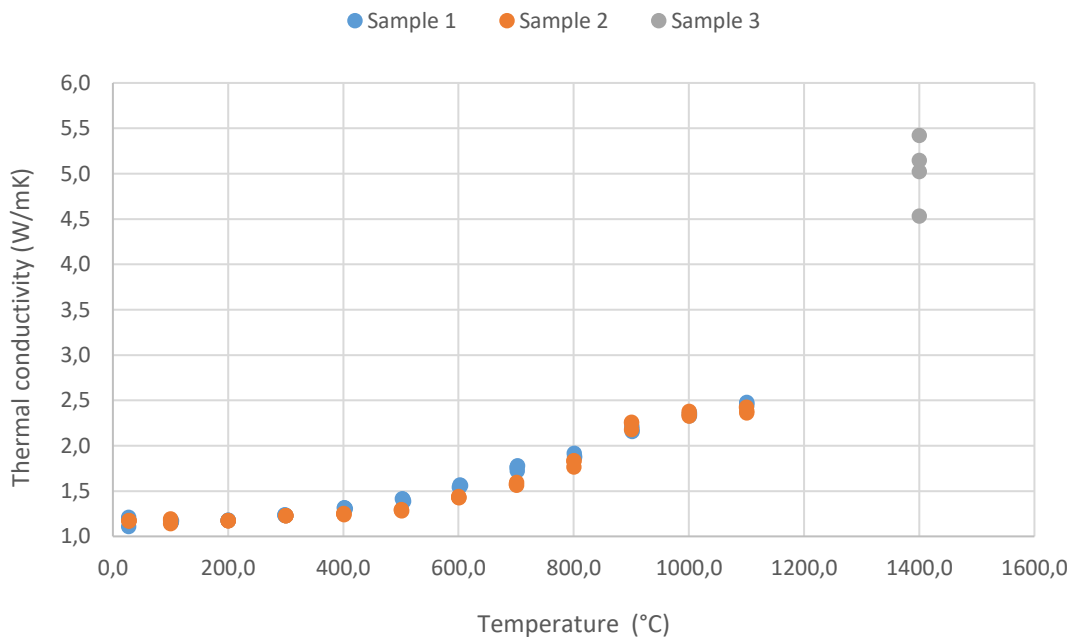

Figure 30 Repeat measurements of sample X2.

9.1.3 Sample R2

The measured values for thermal conductivity from room temperature to 1100 °C for sample R2 are shown in Figure 31 below. For this sample the overall repeatability is

acceptable, but specific measurement points are more problematic than others. Especially on the higher end of the temperature spectrum there is increased variability, with the greatest being exhibited at 1100 °C.

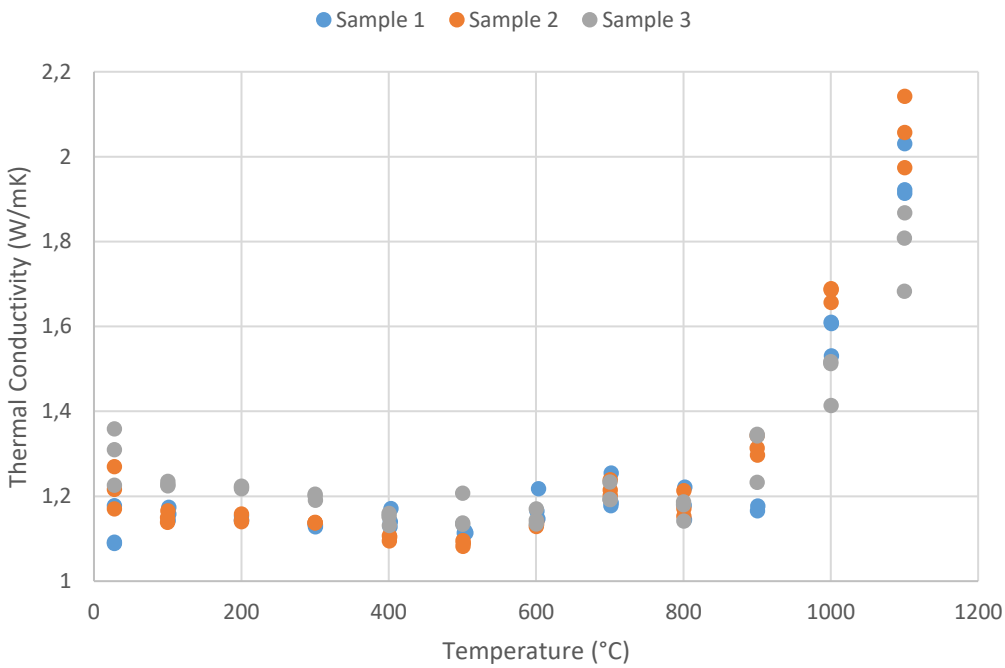

Figure 31 Repeat measurements of sample R2.

9.1.4 Sample K19

The measured values for thermal conductivity from room temperature to 1100 °C for sample K19 are presented in Figure 32 below. Overall, repeatability is acceptable, with repeat measurements of the same sample being grouped closer together than the two different samples averages.

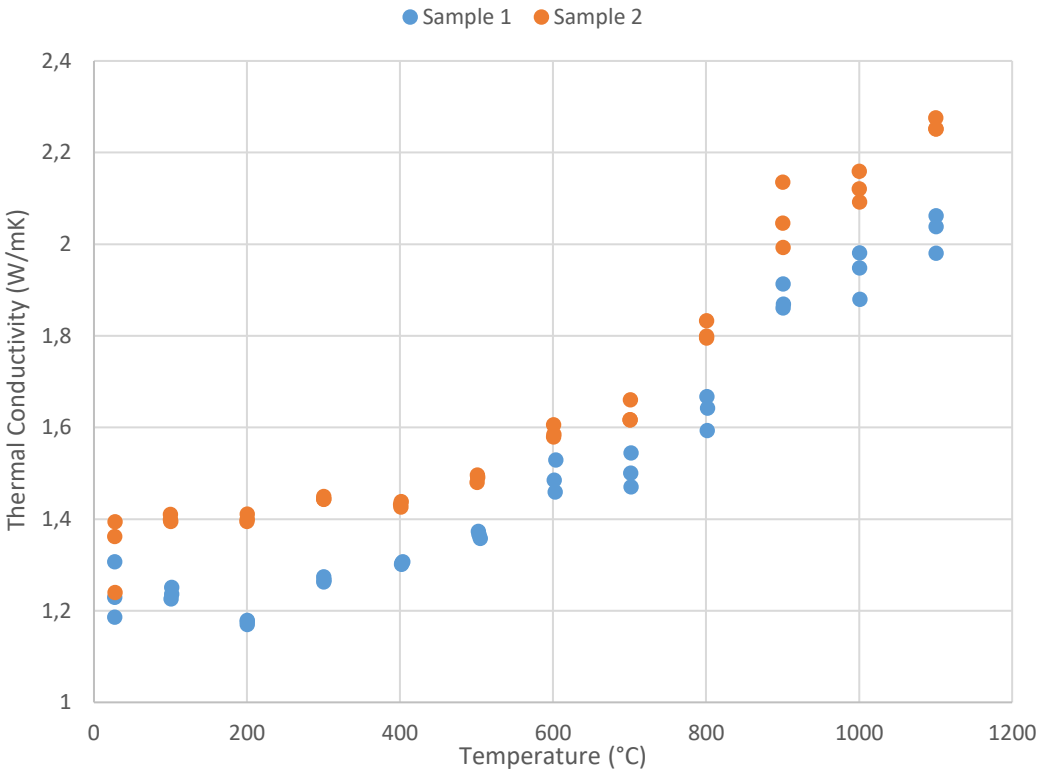

Figure 32 Repeat measurements of sample K19

9.2 Hot Disk TPS 2500 S

The manufacturer of the Hot Disk instrument guarantees a better than 5% accuracy for measurements. In practice, the real error may be higher than this. As mentioned before, the furnace could not be equipped with an inert atmosphere, which led to sample oxidation during the tests. Another equipment-related source of error is the use of mica sensors for the measurements. The equipment manufacturer does not recommend using mica sensors under 300 °C, to assure accurate the results. However, Kapton sensors could not be used at temperatures over 300 °C. This was a problem because the experiments were intended to be performed for the full temperature range in one session, without changing sensors in between. Furthermore, heating and cooling samples multiple times could have had unforeseen effects on their phase composition even without the use of an oxidizing atmosphere. The results from room temperature

measurements with Kapton sensors match the LFA results the best, as can be seen in Figure 27.

9.2.1 Sample K19

Sample K19 was measured in room temperature with the Kapton sensor. The measurement repeats are shown in Figure 33 below. The mica-sensor measurements ranged from room temperature to 400 °C and are shown in Figure 34. The results for the Kapton measurements are grouped in two clusters. The mica measurement repeats exhibit good repeatability.

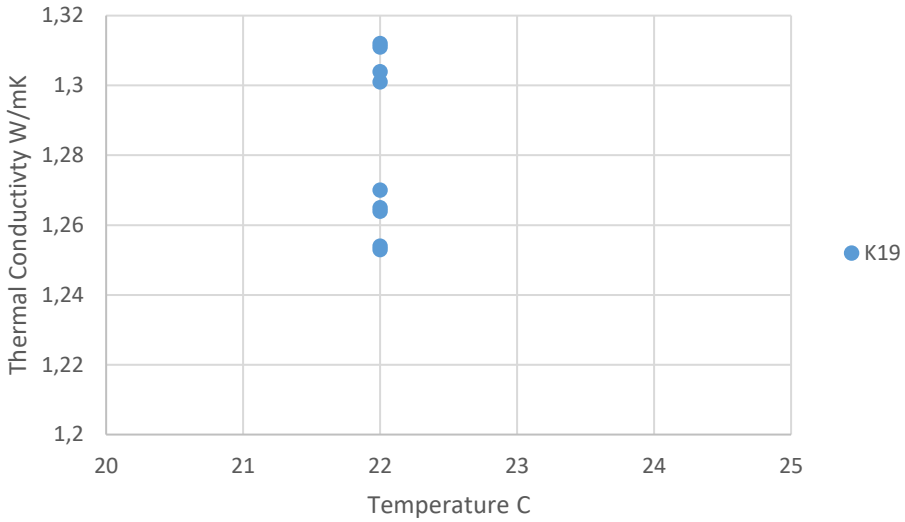

Figure 33 Measurement repeats for room temperature Kapton sensor measurements

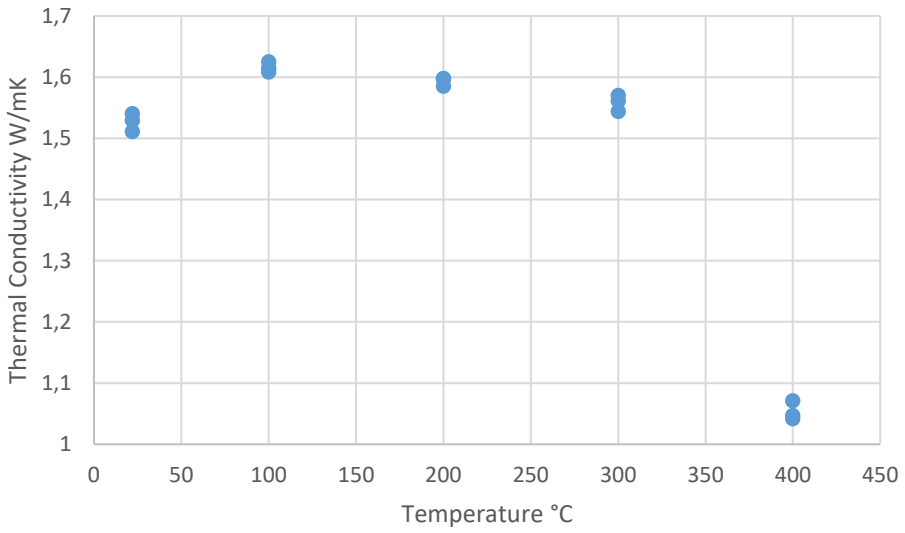

Figure 34 Slag K19 repeat measurements from room temperature to 400 C with mica sensor.

9.2.2 Sample X2

Sample X2 was measured in room temperature with the Kapton sensor. The measurement repeats are shown in Figure 35 below. There is one outlier in the measurement results, the deviance from the mean of the other results being around 10 %, which does exceed the promised error margin of 5%. The mica-sensor measurements ranged from room temperature to 400 °C and are shown in Figure 36. They exhibit good repeatability from room temperature to 300 °C, but at 400 °C there are some issues. Although the decrepitation of the sample due to oxidization is one potential cause of this, sensor failure is also possible. The two points shown here are far from one another, and the third one not pictured was necessary to discard, as it was orders of magnitude different.

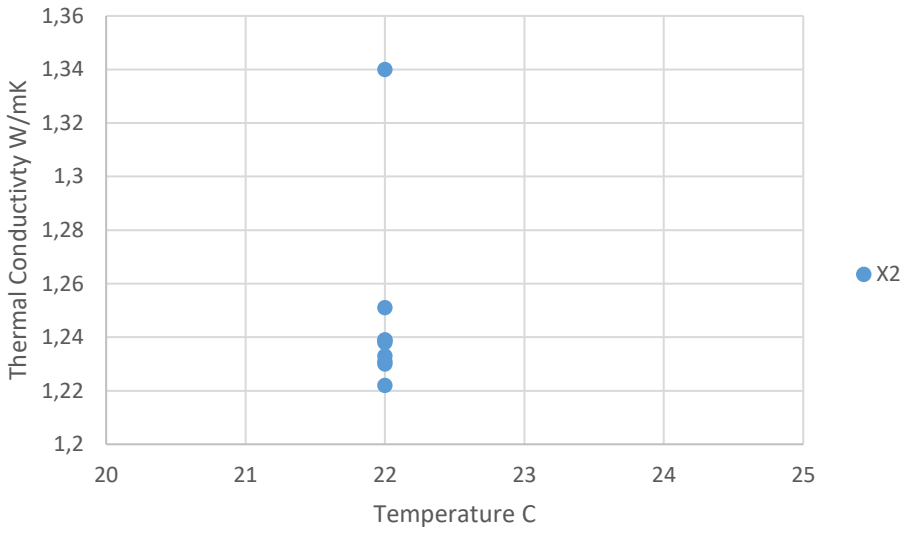

Figure 35 Kapton measurement repeats for slag X2

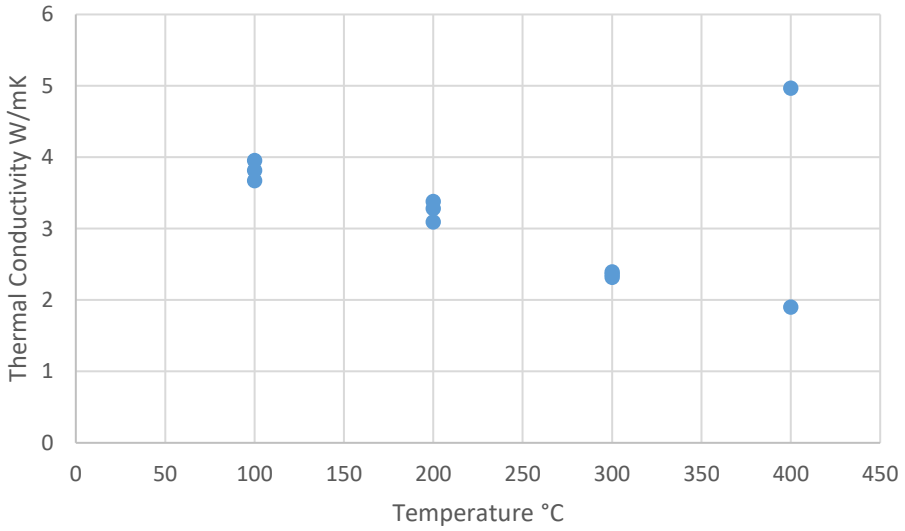

Figure 36 Slag X2 repeat measurements at 100-400 C with mica sensor.

9.2.3 Sample R2

Sample R2 was measured in room temperature with the Kapton sensor. The measurement repeats are shown in Figure 37 below. The results are well grouped, exhibiting good repeatability.

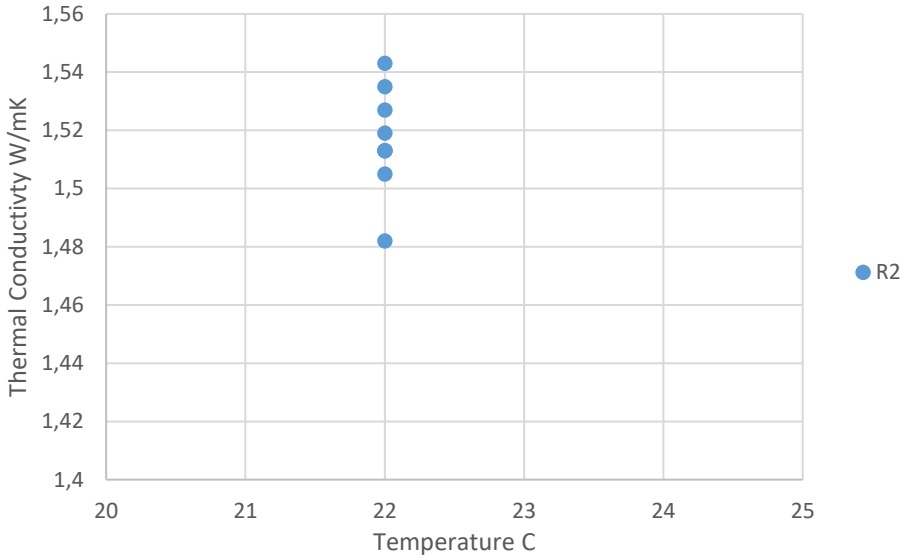

Figure 37 Kapton repeat measurements for slag R2

10 Conclusions

The main objective of this thesis was to create empirical data on the thermal conductivities of ilmenite smelting slags, by studying three slag samples and one sample of excavated freeze-lining. The incentive for finding this knowledge is to better be able to optimize the necessary freeze-lining in ilmenite smelters. The literature study found that data on the thermal conductivity of ilmenite slag is not available. Therefore, other metallurgical slags were studied. They were found to largely have thermal conductivities that increased with increasing temperature, until upon reaching their melting point the thermal conductivity decreased. The structure of ilmenite slags was found to be different than siliceous slags, which reach a polymerized configuration in liquid form.

The experimental approach was to take measurements with two different methods, LFA and TPS. This allowed the creation of additional information through comparison of the results for these two different methods. The measurement results were evaluated by comparing their repeatability. Three slag samples were analyzed for their chemical composition. Additional characterization of the samples was done through SEM-EDS analysis, and in the case of the freeze-lining sample, CT imaging. These methods shed light on the structure of the materials and allowed for speculation on the effect of structure on their thermal properties.

The thermal conductivity of the slags appeared to rise with rising temperatures. The chemical composition of the slag seems to have some effect on the thermal conductivity. Likewise, microstructure and porosity of the material has an effect. However, as these factors are likely to be highly affected by the slag composition, the question of how much can the thermal properties of an ilmenite smelter's freeze-lining be manipulated by means of process control rises.

Further research is needed at higher temperatures, close to the melting point of the slags in ilmenite smelters, as these are the temperatures at which the freeze-lining

formation occurs. Investigation of the thermal properties of the molten slag is similarly warranted. It would be interesting to discover whether TiO_2-rich slags exhibit a sharp drop in thermal conductivity after melting, as many other slags do. Further characterization of freeze-lining samples from ilmenite smelters would be beneficial to the effort to understand the phenomenon. Furthermore, an investigation on the differences of freeze-lining composition depending on which part of the furnace-wall it has been excavated on could be of use. A thorough comparison of freeze-linings from different smelters with different sorts of feed and slag compositions could shed on light on how slag composition translates to the respective freeze-lining's properties. Such a comparison is unlikely to occur, however, due to the nature of industrial competition.

The secondary objective of comparing the LFA and TPS was only a partial success, as a complete set of measurements couldn't be acquired for all samples on the TPS method. Furthermore, the results gotten with the mica sensor do not match the results from LFA experiments. Challenges with the equipment and setup have undoubtedly contributed to the difference, as has the unsuitability of mica sensors for measurements below 300 °C, a stated by the equipment manufacturer. Room temperature Kapton-sensor measurements, however, agree with LFA-derived results for the most part. Both Kapton and mica-sensor measurements also exhibit an acceptable level of repeatability, comparable to that of the LFA measurements. This leads to the conclusion that when optimally applied, the TPS and LFA methods can be equally reliable.

References

BEDINGER, G.M., 2018. *United States Geological Survey Mineral Commodity Summaries.* U.S. Geological Survey.

BEDINGER, G., KOHLER, J. and WALLACE, G., 2018. *USGS 2015 Minerals Yearbook.* U.S. Geological Survey.

BESSINGER, D., 2000. *Cooling characteristics of high titania slags*, Pretoria : [s.n.].

ERIKSSON, G. and PELTON, A.D., 1993. Critical evaluation and optimization of the thermodynamic properties and phase diagrams of the MnO-TiO2, MgO-TiO2, FeO-TiO2, Ti2O3-TiO2, Na2O-TiO2, and K2O-TiO2 systems. *Metallurgical Transactions B,* **24**(5), pp. 795-805.

ERIKSSON, R. and SEETHARAMAN, S., 2004. Thermal diffusivity measurements of some synthetic CaO-Al2O3-SiO2 slags. *Metallurgical and Materials Transactions B,* **35**(3), pp. 461-469.

FALLAH-MEHRJARDI, A., HAYES, P. and JAK, E., 2014. Understanding Slag Freeze Linings. *JOM,* **66**(9), pp. 1654-1663.

GUÉGUIN, M. and CARDARELLI, F., 2007. CHEMISTRY AND MINERALOGY OF TITANIA-RICH SLAGS. PART 1-HEMO-ILMENITE, SULPHATE, AND UPGRADED TITANIA SLAGS. *Mineral Processing and Extractive Metallurgy Review,* **28**(1), pp. 1-58.

GUSTAFSSON, S.E., 1991. Transient plane source techniques for thermal conductivity and thermal diffusivity measurements of solid materials. *Review of Scientific Instruments,* **62**(3), pp. 797-804.

HANDFIELD, G. and CHARETTE, G.G., 1971. *Viscosity and structure of industrial high Ti02 slags.*

INCROPERA, F.P., DEWITT, D.P., BERGMAN, T.L. and LAVINE, A.S., 2007. *Fundamentals of Heat and Mass Transfer*. 6 edn. 111 River Street Hoboken NJ USA: John Wiley & Sons.

KENNETH C. MILLS, MIYUKI HAYASHI, LIJUN WANG and TAKASHI WATANABE, 2014. *The Structure and Properties of Silicate Slags.*

KSIAZEK, M., 2012. *The thermophysical properties of raw materials for ferromanganese production*, Norwegian University of Science and Technology.

MATSUSHITA, T., WATANABE, T., HAYASHI, M. and MUKAI, K., 2011. Thermal, optical and surface/interfacial properties of molten slag systems. *International Materials Reviews,* **56**(5-6), pp. 287-323.

MIETTINEN, E., 2008. *Thermal Conductivity and Characteristics of Copper Flash Smelting Flue Dust Accretions*, Helsinki University of Technology.

MILLS, K.C., 1995. 14 Electrical conductivities of molten slags. In: VEREIN DEUTSCHER EISENHUTTELEUTE (VDEH), ed, *Slag Atlas.* Dusseldorf: Verlag Stahleisen GmbH, pp. 557-590.

MIN, S., BLUMM, J. and LINDEMANN, A., 2007. A new laser flash system for measurement of the thermophysical properties. *Thermochimica Acta,* **455**(1), pp. 46-49.

PARKER, W.J., JENKINS, R.J., BUTLER, C.P. and ABBOTT, G.L., 1961. Flash Method of Determining Thermal Diffusivity, Heat Capacity, and Thermal Conductivity. *Journal of Applied Physics,* **32**(9), pp. 1679-1684.

PISTORIUS, P.C., 2012. Departure from Equilibria in Ilmenite Smelting. In: J.P. DOWNEY, T.P. BATTLE and J.F. WHITE, eds, *International Smelting Technology Symposium.* Hoboken, NJ, USA: John Wiley & Sons, Inc, pp. 171-177.

PISTORIUS, P.C., 2008. Ilmenite smelting: the basics. *The Journal of the Southern African Institute of Mining and Metallurgy,* **108**, pp. 35-43.

PISTORIUS, P.C., 2004aEquilibrium interactions between freeze lining and slag in ilmenite smelting, *VII International Conference on Molten Slags Fluxes and Salts* 2004a, The South African Institute of Mining and Metallurgy.

PISTORIUS, P.C., 2004bEquilibrium interactions between freeze lining and slag in ilmenite smelting, *VII International Conference on Molten Slags Fluxes and Salts* 2004b, The South African Institute of Mining and Metallurgy, pp. 237-242.

PISTORIUS, P. and COETZEE, C., 2003. Physicochemical aspects of titanium slag production and solidification. *Metallurgical and Materials Transactions B,* **34**(5), pp. 581-588.

ROZENDAAL, A., PHILANDER, C. and HEYN, R., 2017. The coastal heavy mineral sand deposits of Africa. *South African Journal of Geology,* **120**(6), pp. 133-152.

SAHU, K.K., ALEX, T.C., MISHRA, D. and AGRAWAL, A., 2006a. An overview on the production of pigment grade titania from titania-rich slag. *Waste Management & Research,* **24**(1), pp. 74-79.

SAHU, K.K., ALEX, T.C., MISHRA, D. and AGRAWAL, A., 2006b. An overview on the production of pigment grade titania from titania-rich slag. *Waste Management & Research,* **24**(1), pp. 74-79.

SAITO, Y., KANEMATSU, K. and MATSUI, T., 2009. Measurement of Thermal Conductivity of Magnesia Brick with Straight Brick Specimens by Hot Wire Method. *MATERIALS TRANSACTIONS,* **50**(11), pp. 2623-2630.

SHELTON, S.M., 1934. *THERMAL CONDUCTIVITY OF SOME IRONS AND STEELS OVER THE TEMPERATURE RANGE 100 TO 500 C.*

SUN, S., PAN, Y., TRAN, T. and WRIGHT, S., 2012. *Thermal conductivity of slags and refractory materials.* Stockholm, Sweden: Department of Materials Science and Engineering School of Industrial Engineering and Management, Royal Institute of Technology, KTH, Brinellvägen 23 SE-100 44.

VEREIN DEUTSCHER EISENHÜTTENLEUTE, ed, 1995. *Slag Atlas* . 2nd edn. Verlag Stahleisen GmbH, D-Düsseldorf, Germany.

ZHANG, W., ZHU, Z. and CHENG, C.Y., 2011. A literature review of titanium metallurgical processes. *Hydrometallurgy,* **108**(3), pp. 177-188.

ZIETSMAN, J.H. and PISTORIUS, P.C., 2004. Process mechanisms in ilmenite smelting. *The Journal of The South African Institute of Mining and Metallurgy,* , pp. 653-660.

Appendices

Appendix A – SEM-EDS Sample T1 overview

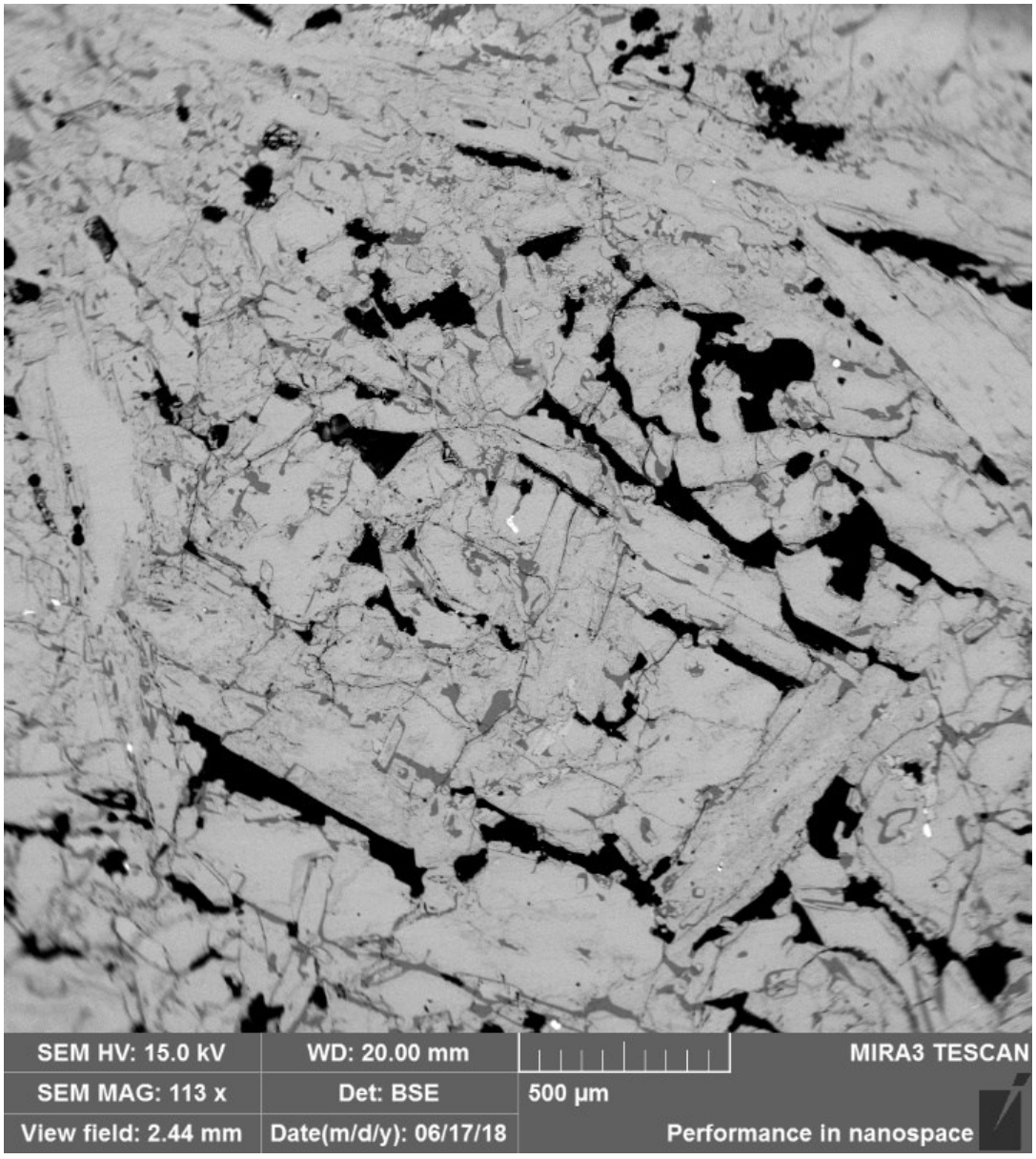

Appendix B – SEM-EDS Sample T1 Site 1 Zoom

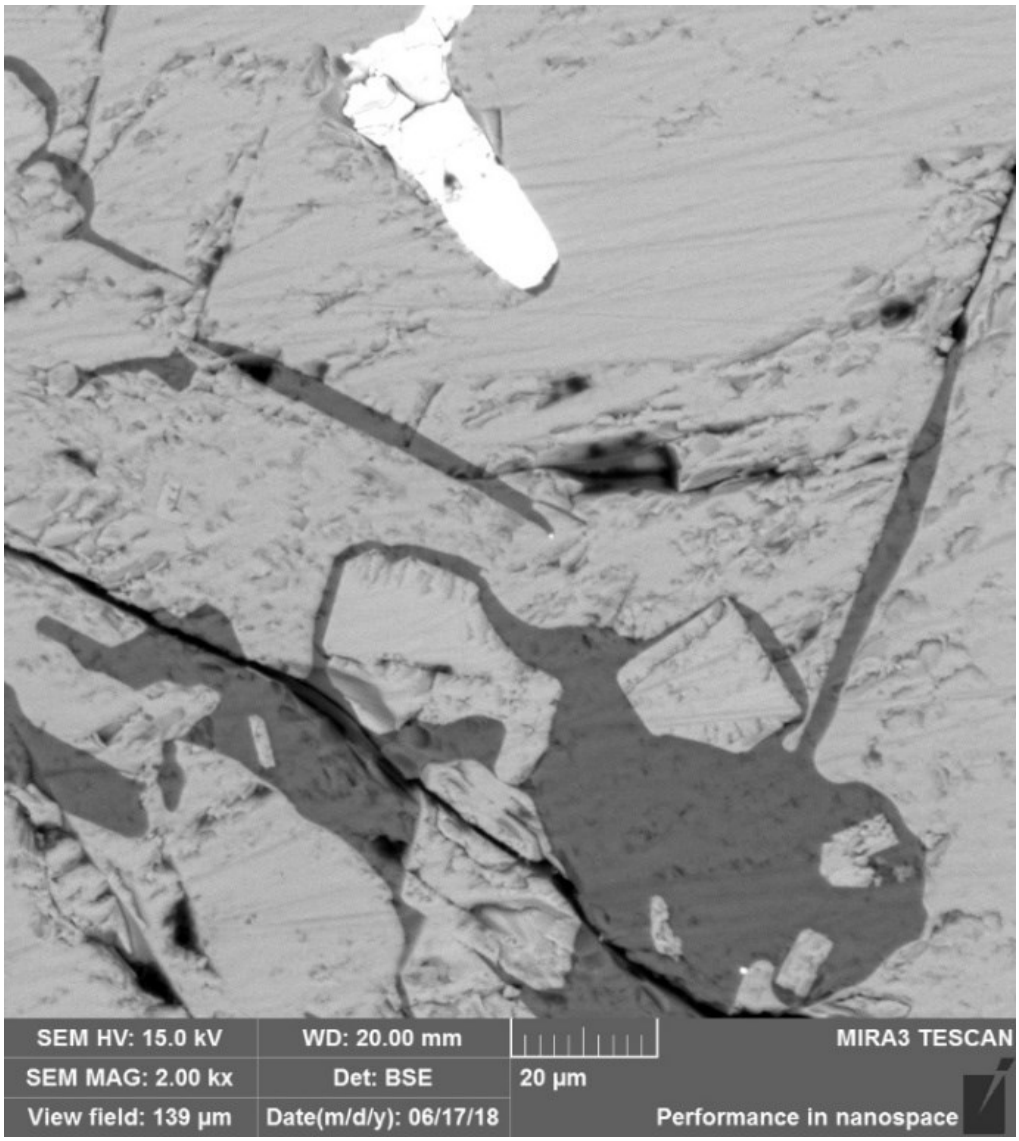

Appendix C – SEM-EDS Sample T1 Site 1 EDS Sites

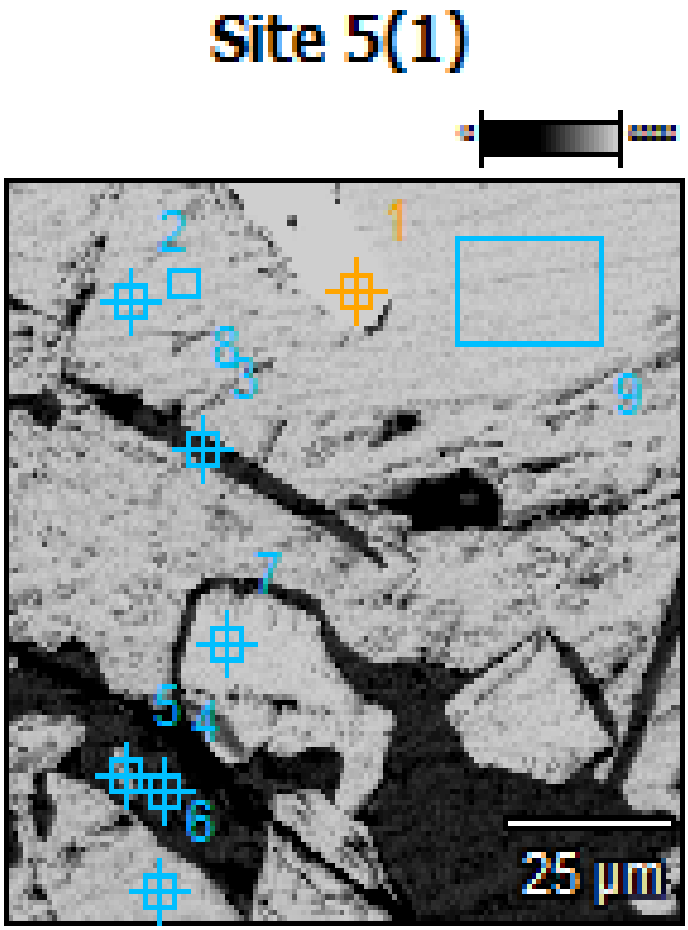

Appendix D – SEM-EDS Sample T1 Site 1 EDS Analyses

Atom %

	O-K	Mg-K	Al-K	Si-K	S-K	K-K	Ca-K	Ti-K	Cr-K	Fe-K	Cu-K	Zn-K	Re-M	Pb-M
Site 5(1)_pt1	0.00	0.00	1.17	0.00	47.44		0.00	1.51		27.58	0.02	21.17	0.05	1.05
Site 5(1)_pt2	57.42	9.40	0.94	0.01			0.01	28.60		3.63	0.00			0.00
Site 5(1)_pt3	68.07	0.05	6.49	22.04		1.49	0.16	1.41		0.29	0.01			0.00
Site 5(1)_pt4	63.75	0.25	7.16	24.83		1.61	0.18	1.82		0.39	0.00			0.00
Site 5(1)_pt5	69.86	0.09	4.21	13.01		0.92	0.08	11.82		0.01	0.00			0.00
Site 5(1)_pt6	58.55	9.42	0.81	0.00			0.01	27.98	0.30	2.93	0.00			0.00
Site 5(1)_pt7	62.00	0.01	0.45	0.06			0.01	37.15	0.30	0.00	0.02			0.00
Site 5(1)_pt8	60.42	8.65	0.94	0.00			0.01	26.42		3.55	0.02			0.00
Site 5(1)_pt9	59.58	8.47	0.82	0.00			0.01	26.93		3.98	0.03	0.18		0.00

Appendix E – SEM-EDS Sample T1 Site 2 Zoom

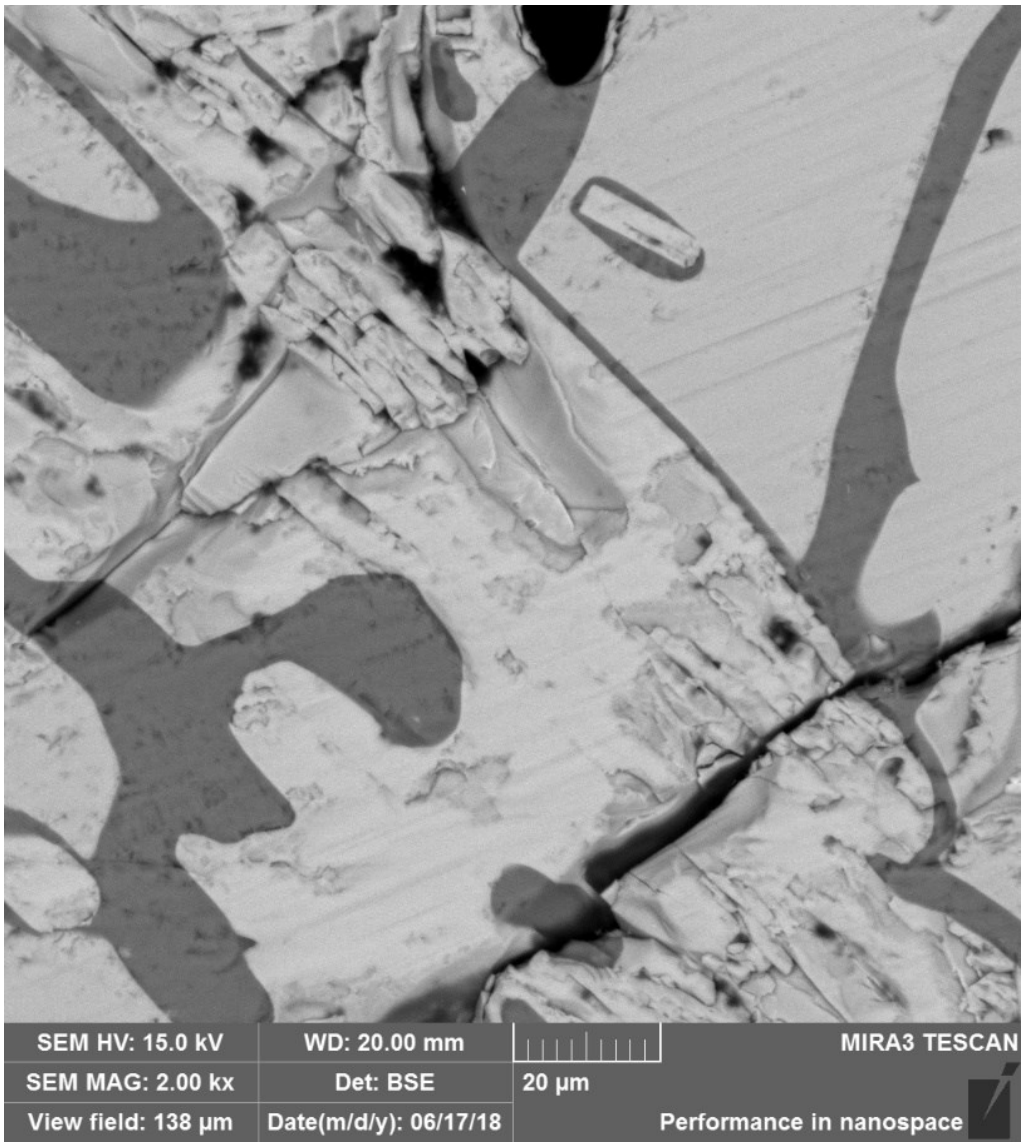

Appendix F – SEM-EDS Sample T1 Site 2 Zoom

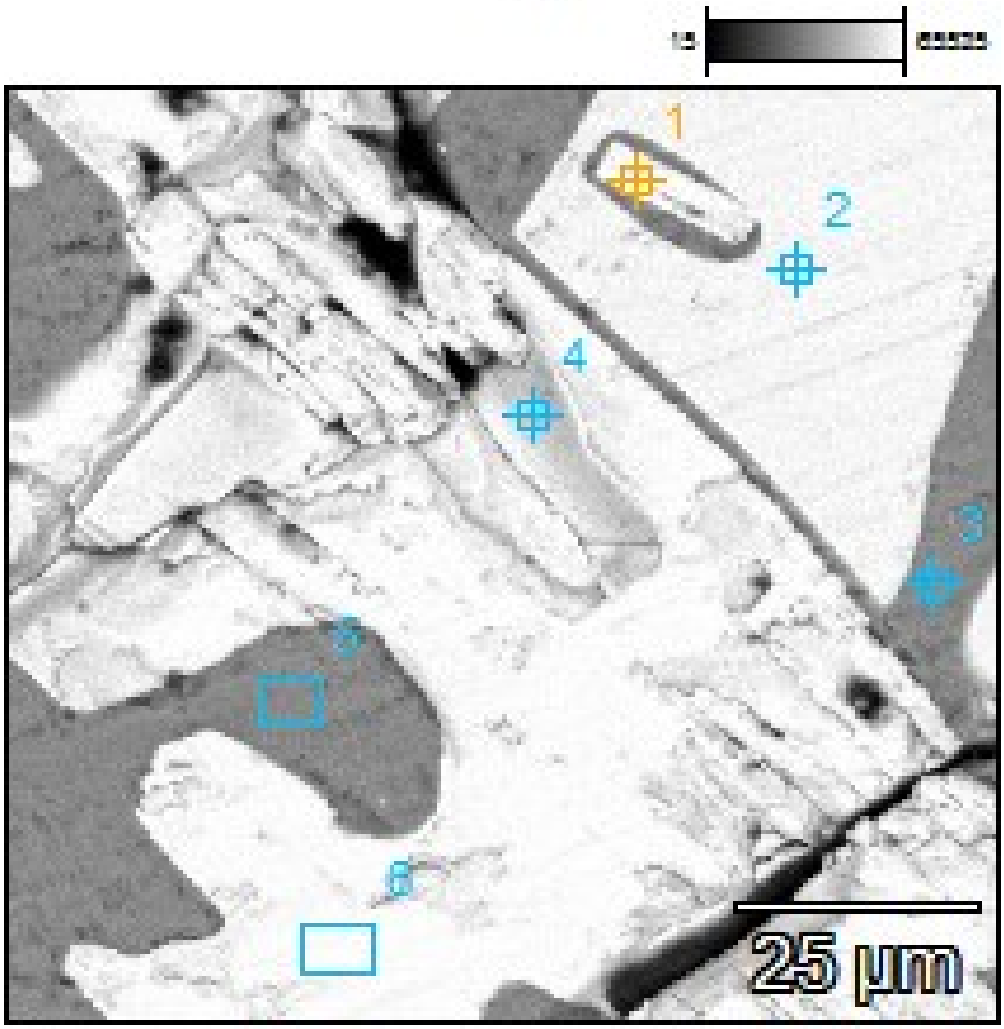

Appendix G – SEM-EDS Sample T1 Site 2 EDS Analyses

Atom %

	O-K	Mg-K	Al-K	Si-K	Ca-K	Ti-K	Cr-K	In-L
Base(2)_pt1	62.70	0.02	0.20	0.13	0.01	36.95		
Base(2)_pt2	61.82	10.05	0.50	0.02	0.00	27.32	0.30	
Base(2)_pt3	69.94	0.31	5.32	20.80	0.55	1.44		1.63
Base(2)_pt4	71.86	0.01	0.04	0.05	0.00	28.04		
Base(2)_pt5	71.64	0.12	4.91	19.60	0.68	1.24		1.81
Base(2)_pt6	60.50	0.00	0.17	0.07	0.00	39.25		

Appendix H SEM-EDS – Sample K19 Site 1 Overview

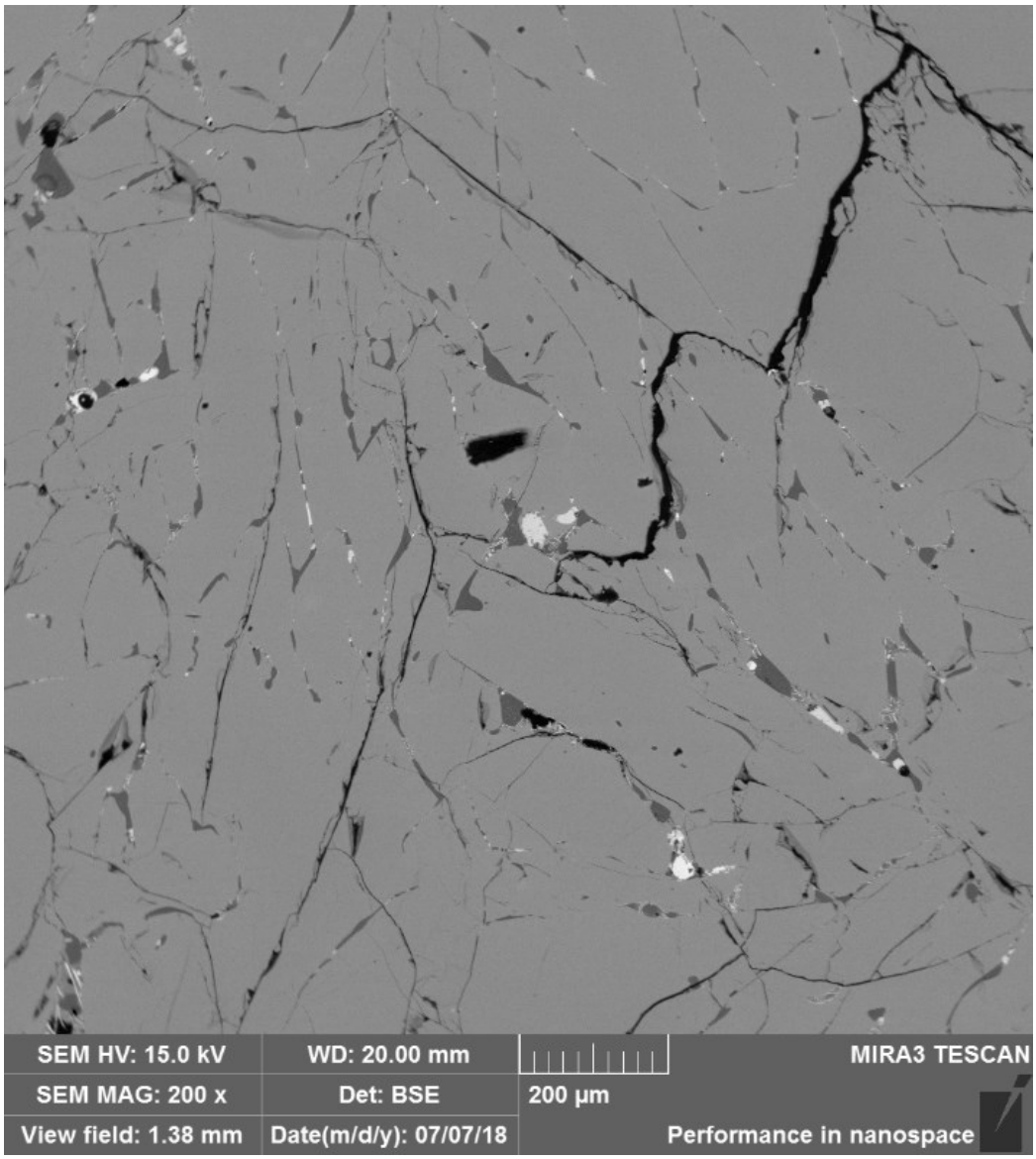

Appendix I SEM-EDS – Sample K19 Site 1 Zoom

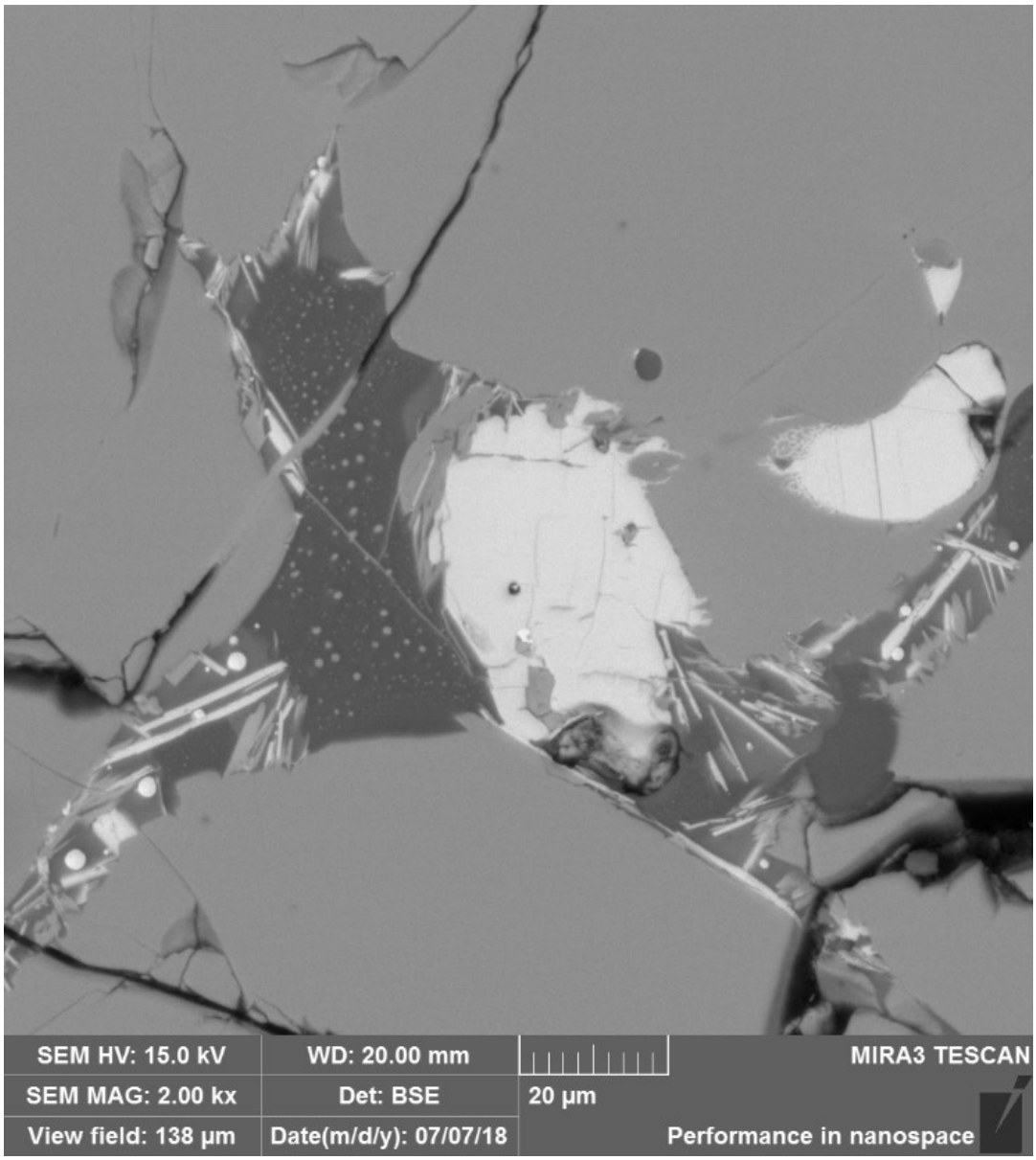

Appendix J SEM-EDS – Sample K19 Site 1 EDS Sites

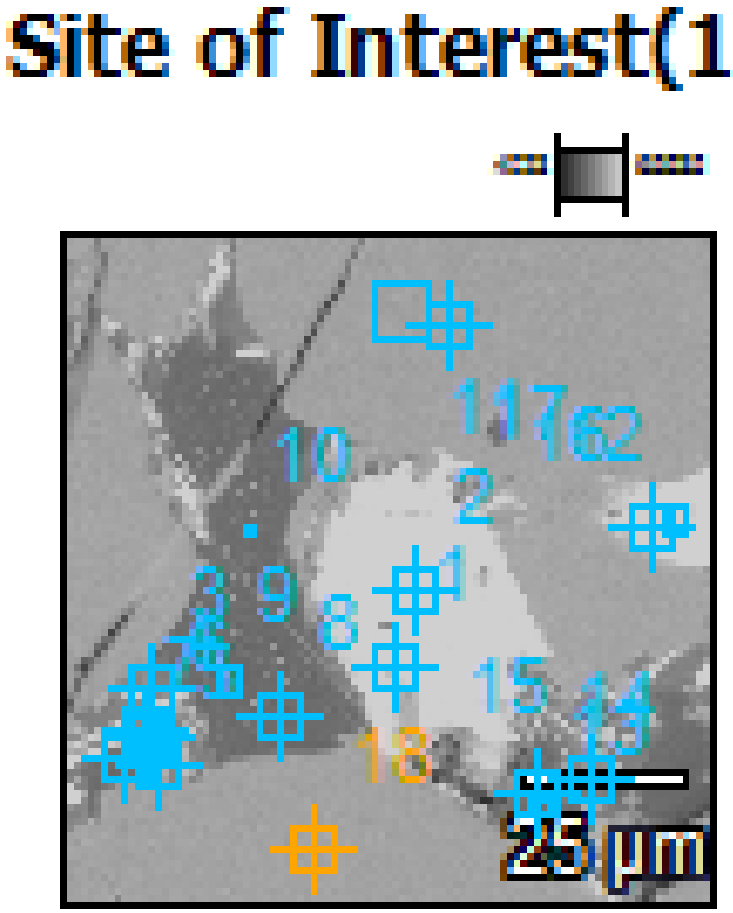

Appendix K SEM-EDS – Sample K19 Site 1 EDS Analyses

Atom %

	O-K	Mg-K	Al-K	Si-K	S-K	Ca-K	Ti-K	Mn-K	Fe-K	Pd-L
Site of Interest(1)_pt1	10.77	0.00	0.03	0.21	7.30	0.05	0.73	0.23	80.68	
Site of Interest(1)_pt2	0.00	0.00	0.02	0.04	48.81	0.02	0.01	2.98	48.12	
Site of Interest(1)_pt3	10.02	0.52	0.84	4.15	0.07	0.53	1.82	0.70	81.36	
Site of Interest(1)_pt4	65.86	0.54	3.46	18.40		3.02	5.18	3.10	0.45	
Site of Interest(1)_pt5	67.94	0.20	2.46	18.88		1.07	7.93	1.43	0.09	
Site of Interest(1)_pt6	69.61	0.30	2.04	15.12		2.44	8.65	1.43	0.39	
Site of Interest(1)_pt7	66.26	0.11	2.58	26.67		1.03	2.02	1.13	0.20	
Site of Interest(1)_pt8	65.81	0.05	2.64	28.53		0.65	1.39	0.57	0.36	0.00
Site of Interest(1)_pt9	65.77	0.10	2.49	27.75		0.72	1.81	0.97	0.40	
Site of Interest(1)_pt10	65.88	0.08	2.56	28.22		0.68	1.43	0.72	0.42	
Site of Interest(1)_pt11	56.79	1.20	1.02	0.12		0.02	35.29	1.08	4.48	
Site of Interest(1)_pt12	5.38	0.00	0.04	0.02	46.69	0.03	0.01	3.12	44.70	
Site of Interest(1)_pt13	63.94	0.12	2.75	26.73		0.93	1.12	0.39	4.03	
Site of Interest(1)_pt14	50.17	0.09	2.18	19.32	2.42	1.18	1.48	0.33	22.83	
Site of Interest(1)_pt15	64.84	0.46	3.52	19.58		3.55	5.37	1.68	1.00	
Site of Interest(1)_pt16	8.55	0.00	0.09	0.08	43.99	0.02	1.21	2.50	43.58	
Site of Interest(1)_pt17	56.75	1.20	1.05	0.10		0.02	35.47	0.87	4.53	
Site of Interest(1)_pt18	57.60	1.16	0.93	0.16		0.01	34.13	1.51	4.48	

Appendix L SEM-EDS – Sample K19 Site 2 Overview

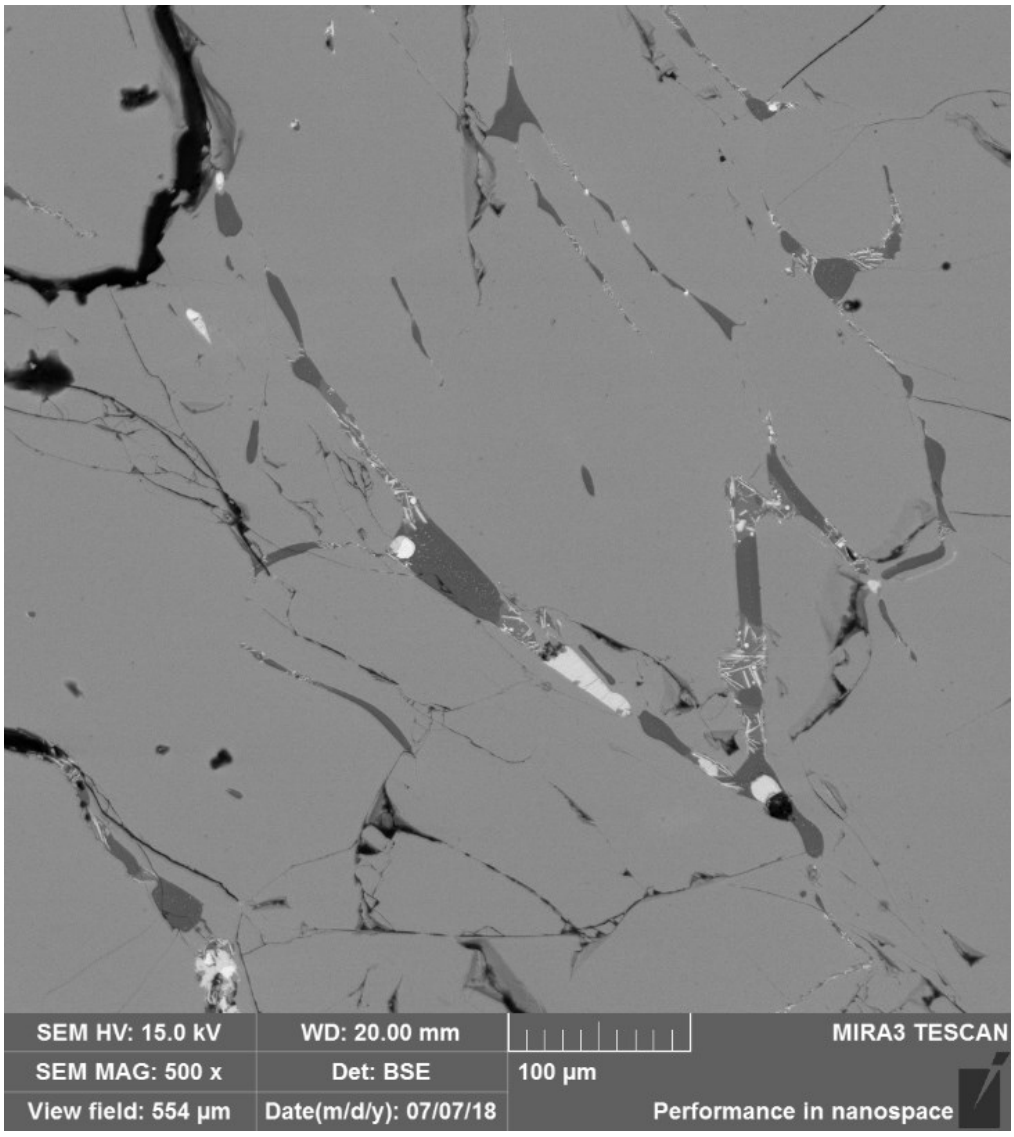

Appendix M SEM-EDS – Sample K19 Site 2 Zoom

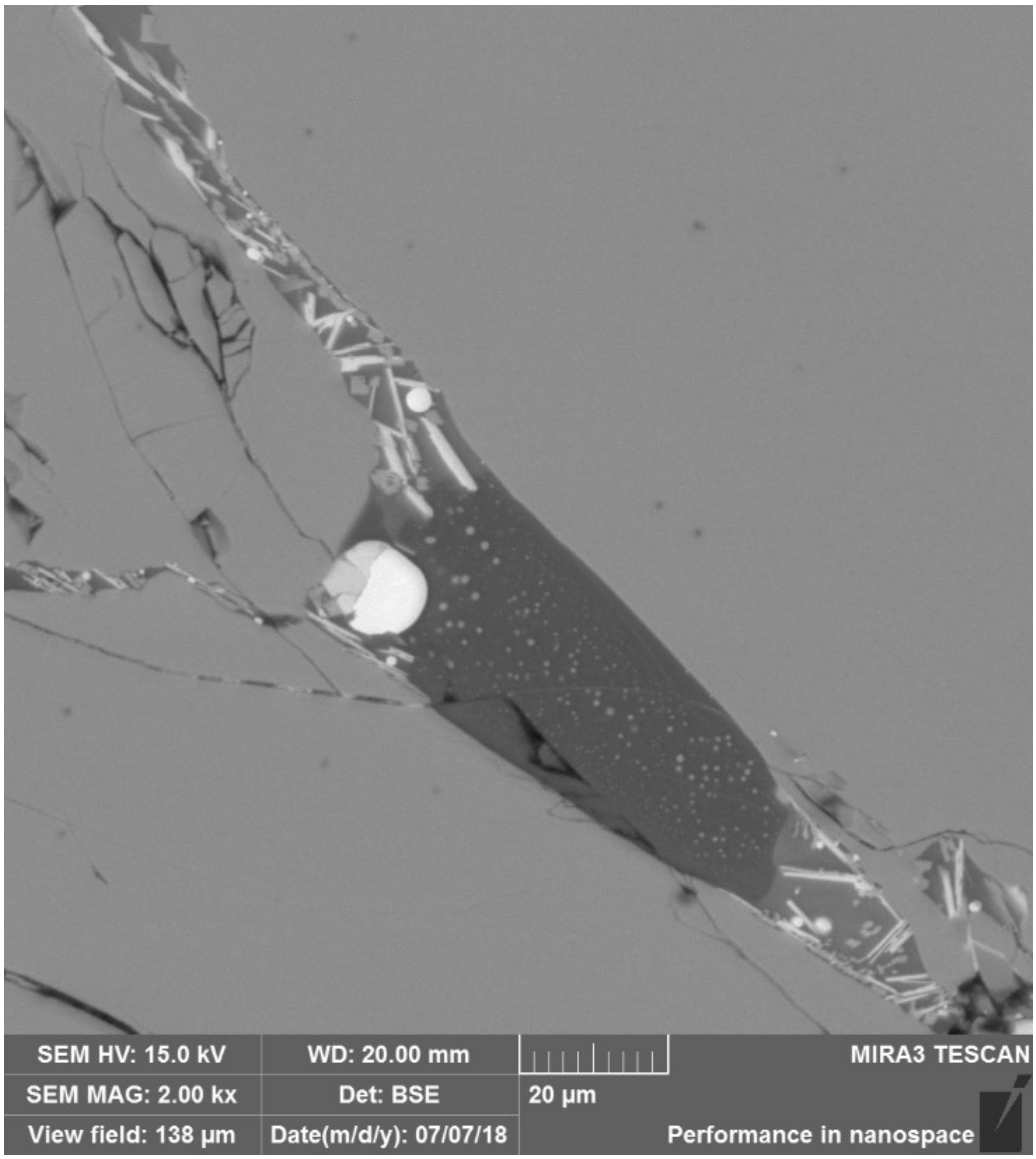

Appendix N SEM-EDS – Sample K19 Site 2 EDS Sites

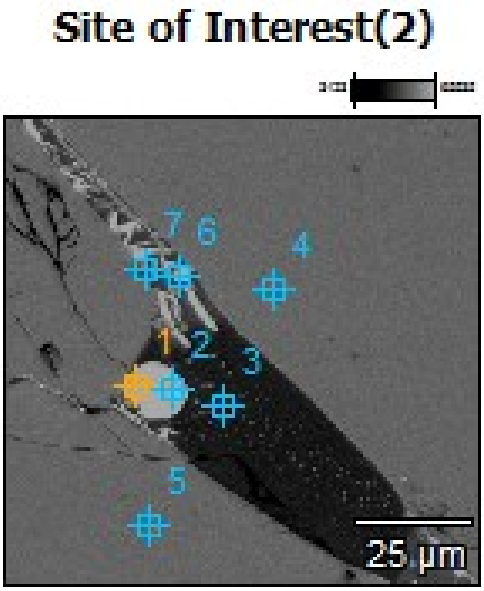

Appendix O SEM-EDS – Sample K19 Site 2 EDS Analyses

Atom %

	O-K	Mg-K	Al-K	Si-K	S-K	Ca-K	Ti-K	Cr-K	Mn-K	Fe-K
Site of Interest(2)_pt1	0.00	0.00	0.06	0.05	47.45	0.03	1.74		24.38	26.29
Site of Interest(2)_pt2	0.00	0.01	0.04	0.36		0.09	1.81			97.69
Site of Interest(2)_pt3	64.99	0.05	2.54	29.44		0.59	1.52		0.52	0.34
Site of Interest(2)_pt4	56.38	1.14	1.02	0.15		0.02	35.40	0.30	1.06	4.53
Site of Interest(2)_pt5	57.50	1.10	0.99	0.13		0.02	34.76		1.03	4.47
Site of Interest(2)_pt6	0.00	0.09	0.03	0.68	0.18	0.23	3.20		0.46	95.14
Site of Interest(2)_pt7	68.08	0.13	0.98	3.89		0.39	26.10		0.44	0.00

Appendix P SEM-EDS – Sample R2 Site 1 Overview

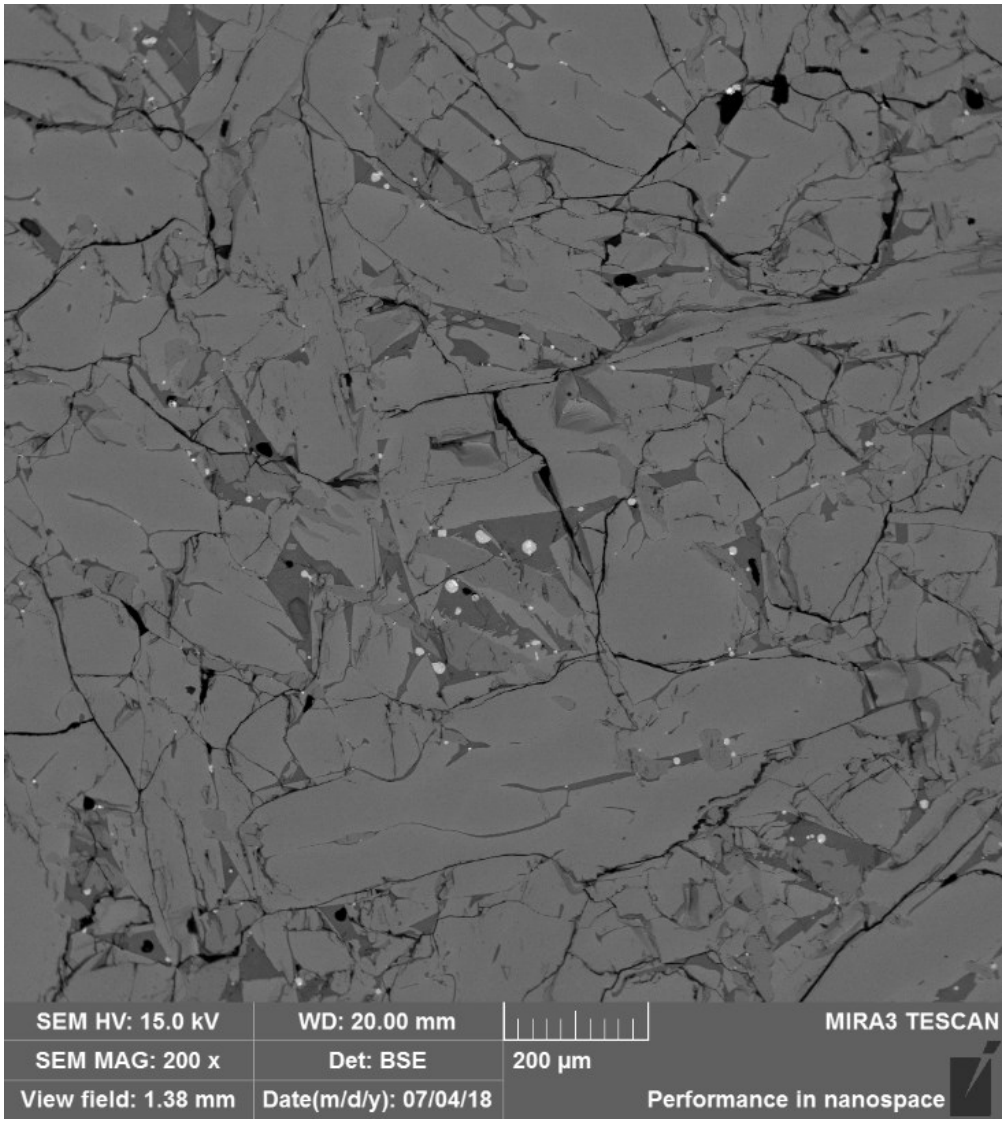

Appendix Q SEM-EDS – Sample R2 Site 1 Zoom

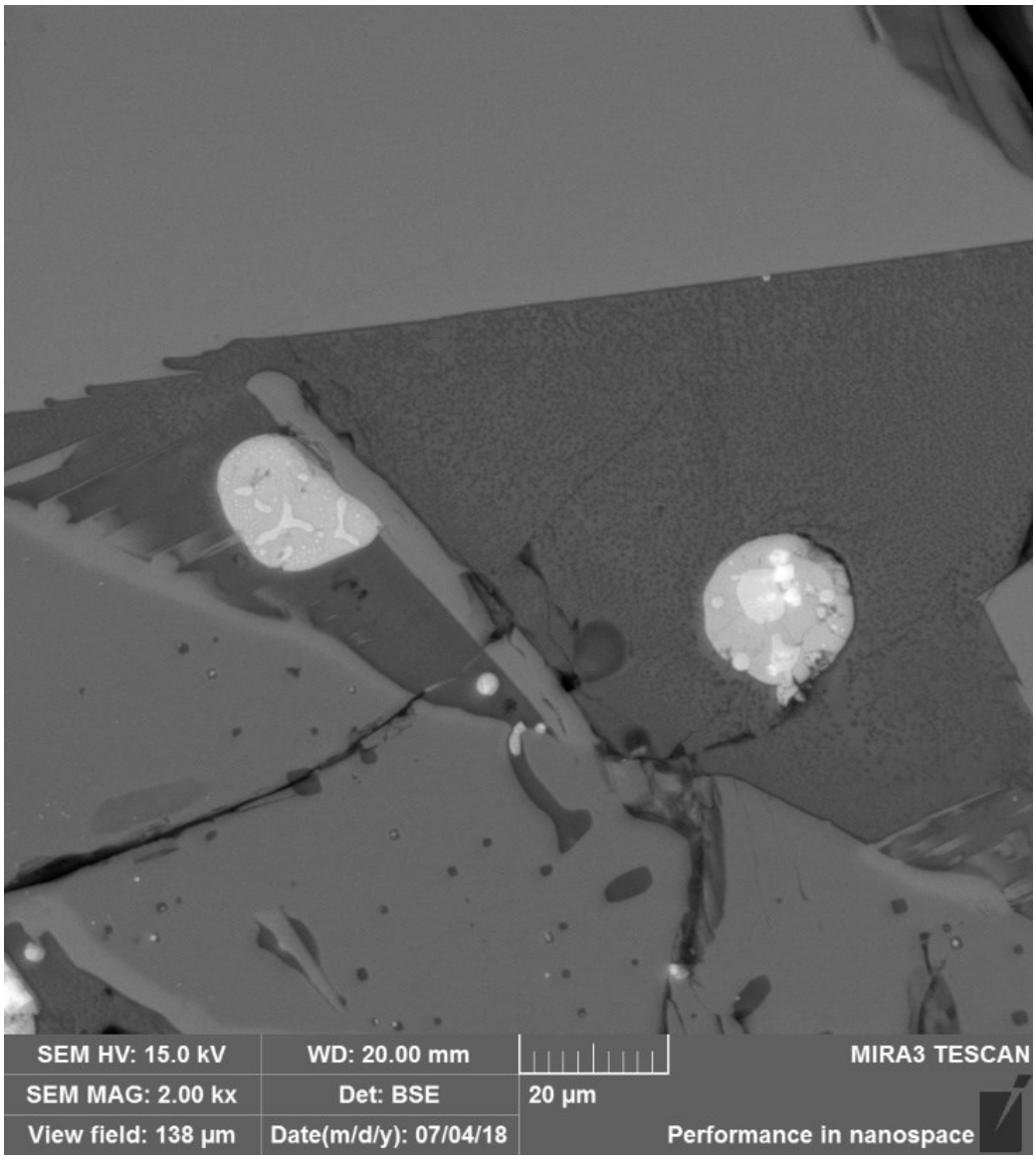

Appendix R SEM-EDS – Sample R2 Site 1 EDS Sites

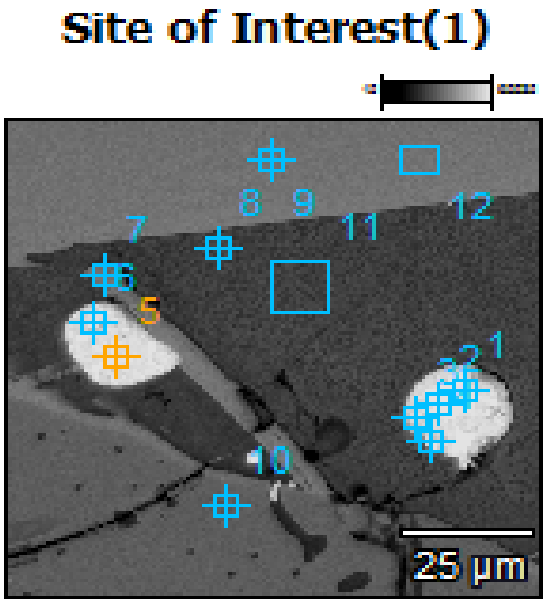

Appendix S SEM-EDS – Sample R2 Site 1 EDS Analyses

Atom %

	O-K	Mg-K	Al-K	Si-K	S-K	Cl-K	Ca-K	Ti-K	Fe-K
Site of Interest(1)_pt1	1.97	1.16	0.64	0.30	56.75		0.12	0.01	39.05
Site of Interest(1)_pt2	0.00	0.35	0.09	0.19	3.35		0.16	0.72	95.14
Site of Interest(1)_pt3	6.41	0.32	0.22	0.20	43.77		0.12	0.00	48.95
Site of Interest(1)_pt4	6.83	0.21	0.03	0.21	39.12		0.12	0.01	53.45
Site of Interest(1)_pt5	0.00	0.26	0.07	0.17	14.14		0.07	1.16	84.14
Site of Interest(1)_pt6	0.00	0.01	0.00	0.22	38.87		0.11	0.83	59.94
Site of Interest(1)_pt7	53.38	2.62	0.84	0.74	0.01		0.24	31.77	10.41
Site of Interest(1)_pt8	62.79	0.94	3.07	20.55	0.00	0.03	5.11	2.36	5.14
Site of Interest(1)_pt9	57.67	3.45	1.27	0.10	0.03		0.03	30.44	7.02
Site of Interest(1)_pt10	62.94	0.01	0.10	0.12	0.27		0.04	36.46	0.06
Site of Interest(1)_pt11	63.92	0.84	2.93	20.44	0.00	0.03	4.74	2.29	4.81
Site of Interest(1)_pt12	57.51	3.18	1.14	0.10	0.02		0.05	30.33	7.67

Appendix T SEM-EDS – Sample R2 Site 2 Zoom

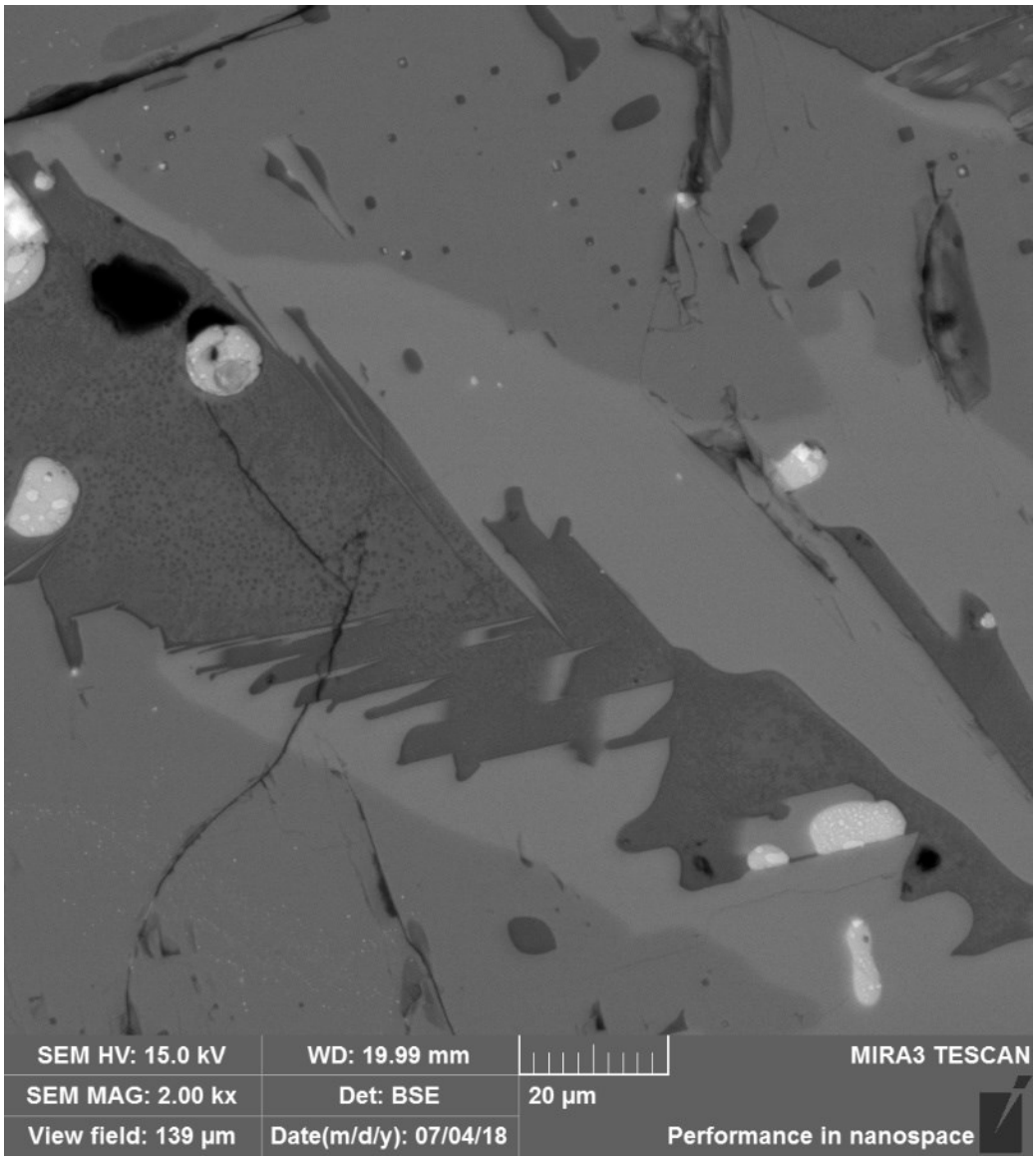

Appendix U SEM-EDS – Sample R2 Site 2 EDS Sites

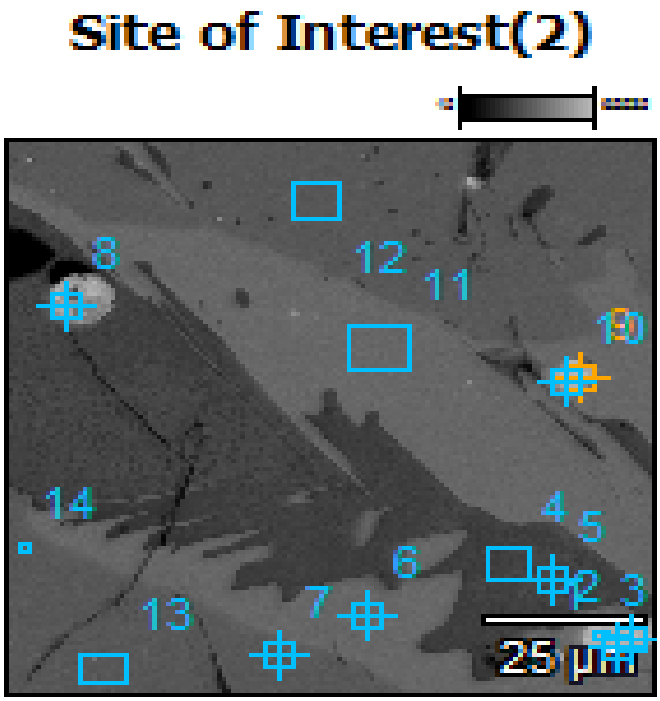

Appendix V SEM-EDS – Sample R2 Site 2 EDS Analyses

Atom %

	O-K	F-K	Mg-K	Al-K	Si-K	S-K	Cl-K	Ca-K	Ti-K	Fe-K
Site of Interest(2)_pt1	6.65		0.58	0.22	0.11	21.21		0.06	2.96	68.21
Site of Interest(2)_pt2	6.07		0.01	0.03	0.15	37.06		0.08	1.29	55.32
Site of Interest(2)_pt3	0.00		0.00	0.00	0.16	38.21		0.07	1.39	60.16
Site of Interest(2)_pt4	63.89		0.76	3.09	20.86	0.01	0.03	4.96	1.94	4.46
Site of Interest(2)_pt5	62.96		0.80	3.10	20.52	0.00	0.03	5.40	2.14	5.06
Site of Interest(2)_pt6	58.08		2.52	0.99	0.12	0.02		0.05	29.42	8.79
Site of Interest(2)_pt7	57.34		0.06	0.14	0.16	0.29		0.04	41.67	0.31
Site of Interest(2)_pt8	8.51		0.18	0.20	0.29	42.32		0.17	0.01	48.34
Site of Interest(2)_pt9	7.39		1.22	0.61	0.18	32.94		0.02	2.51	55.13
Site of Interest(2)_pt10	6.43		0.34	0.25	0.09	38.64		0.02	2.03	52.20
Site of Interest(2)_pt11	54.00		2.73	1.06	0.10	0.03		0.04	32.66	9.38
Site of Interest(2)_pt12	62.60		0.01	0.10	0.10	0.30		0.02	36.84	0.03
Site of Interest(2)_pt13	63.17		0.03	0.10	0.15	0.28		0.03	36.08	0.17
Site of Interest(2)_pt14	59.98	0.07	0.04	0.12	0.15	1.12		0.07	37.51	0.93

Appendix W SEM-EDS – Sample X2 Site 1 Overview

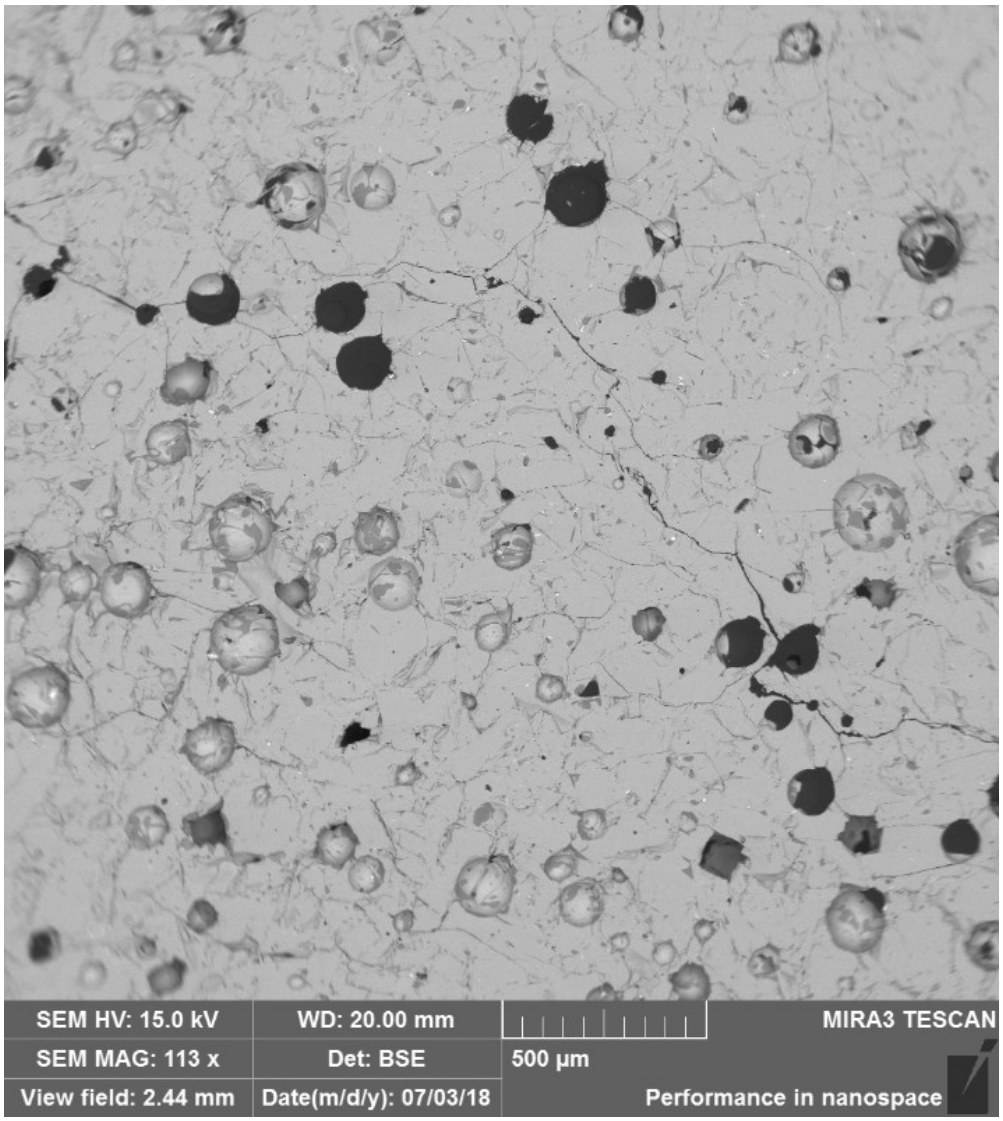

Appendix X SEM-EDS – Sample X2 Site 1 Zoom

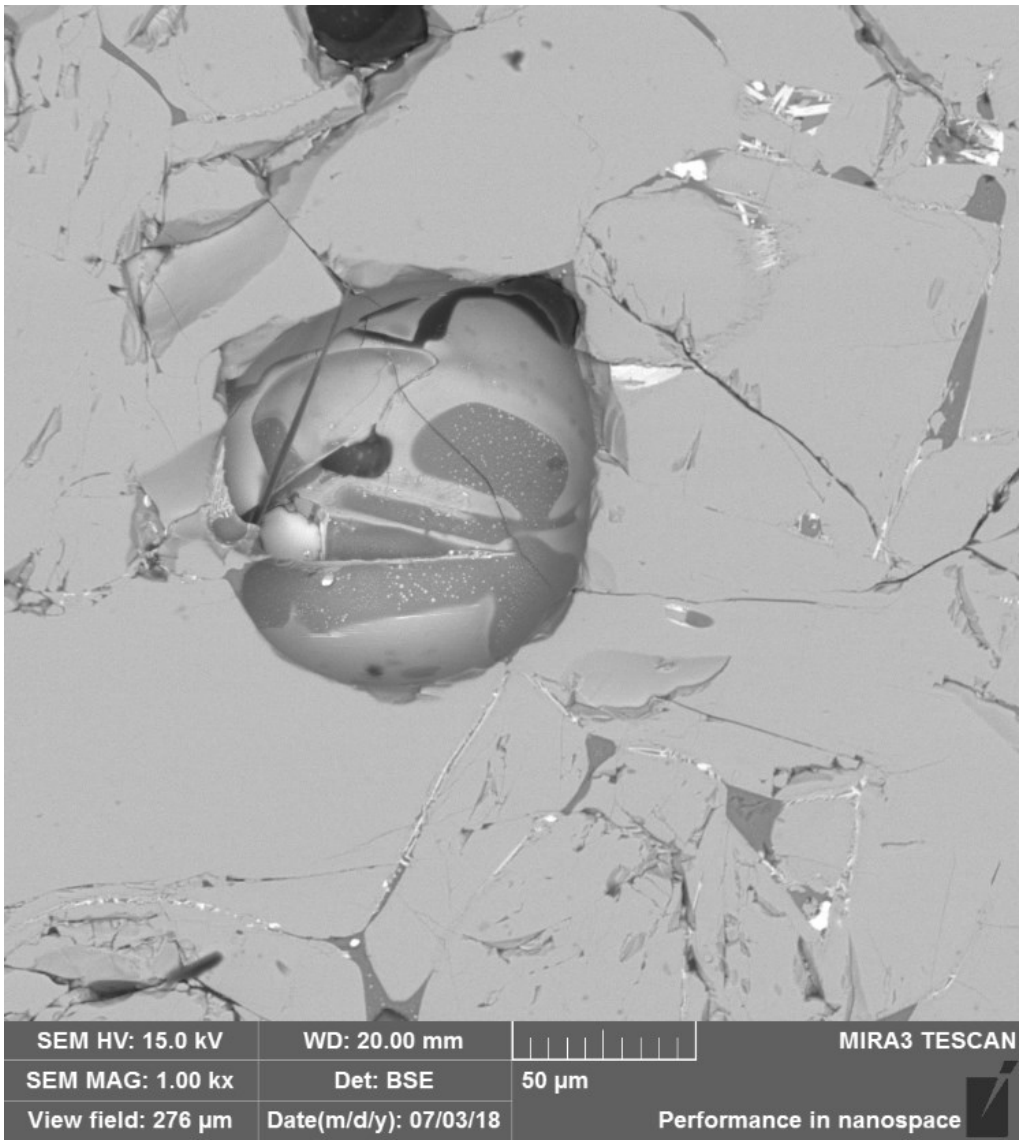

Appendix Y SEM-EDS – Sample X2 Site 1 EDS Sites

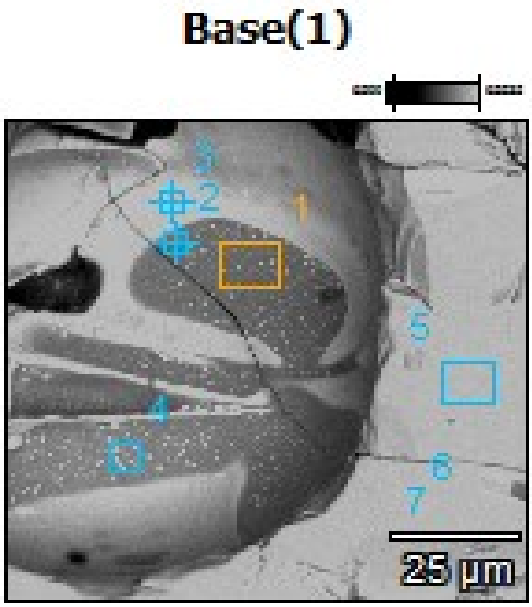

Appendix Z SEM-EDS – Sample X2 Site 1 EDS Analyses

Atom %

	O-K	Mg-K	Al-K	Si-K	K-K	Ca-K	Ti-K	Cr-K	Fe-K	Pd-L
Base(1)_pt1	70.98	0.03	1.62	24.28		0.54	2.55		0.02	
Base(1)_pt2	71.10	0.12	1.87	22.59		0.53	3.76		0.02	0.00
Base(1)_pt3	65.06	1.94	1.13	0.33		0.11	29.39	0.55	1.50	
Base(1)_pt4	46.87	0.56	1.37	1.27	0.23	3.78	45.39		0.52	
Base(1)_pt5	44.39	2.94	1.68	0.11		0.00	48.01	0.81	2.05	
Base(1)_pt6	58.35	2.22	1.24	0.08		0.01	36.13	0.53	1.45	
Base(1)_pt7	63.21	2.20	1.20	0.03		0.02	31.54	0.48	1.32	

Appendix AA SEM-EDS – Sample X2 Site 2 Overview

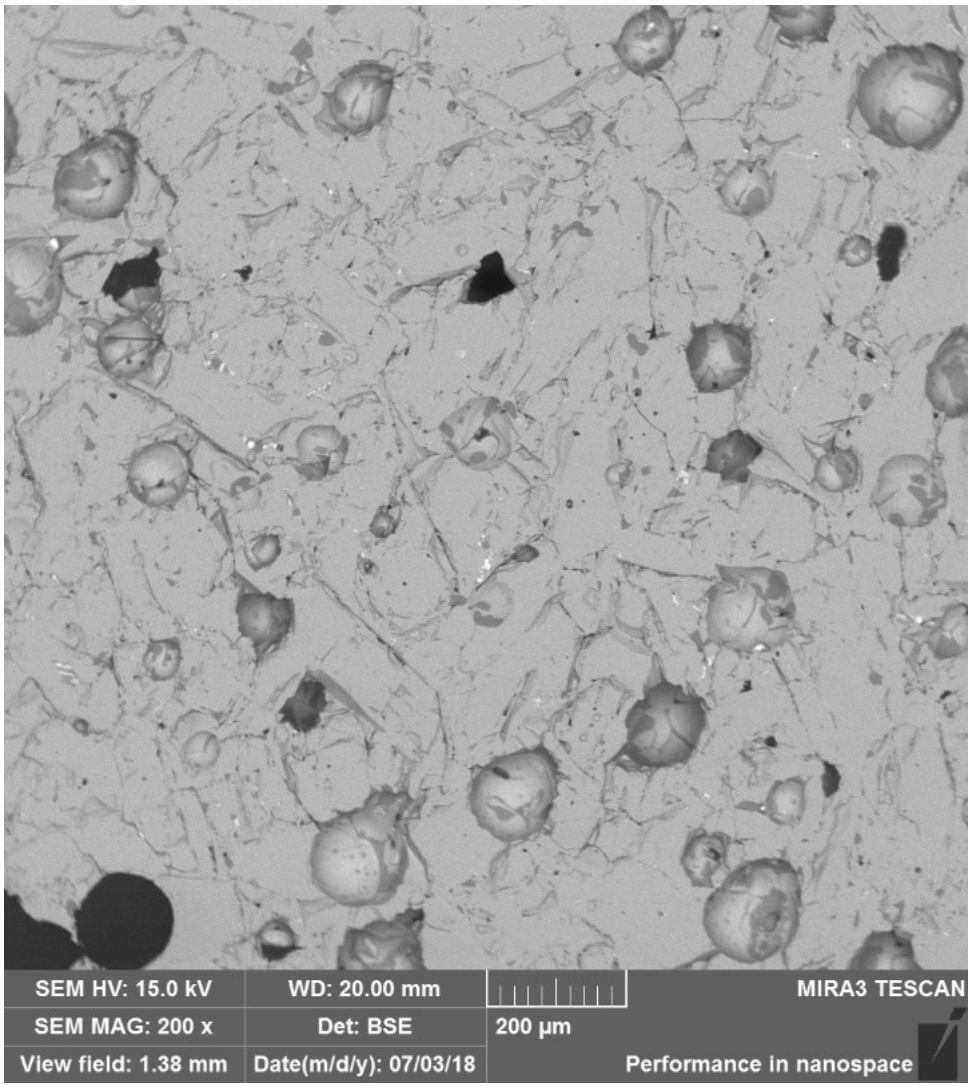

Appendix AB SEM-EDS – Sample X2 Site 2 Zoom

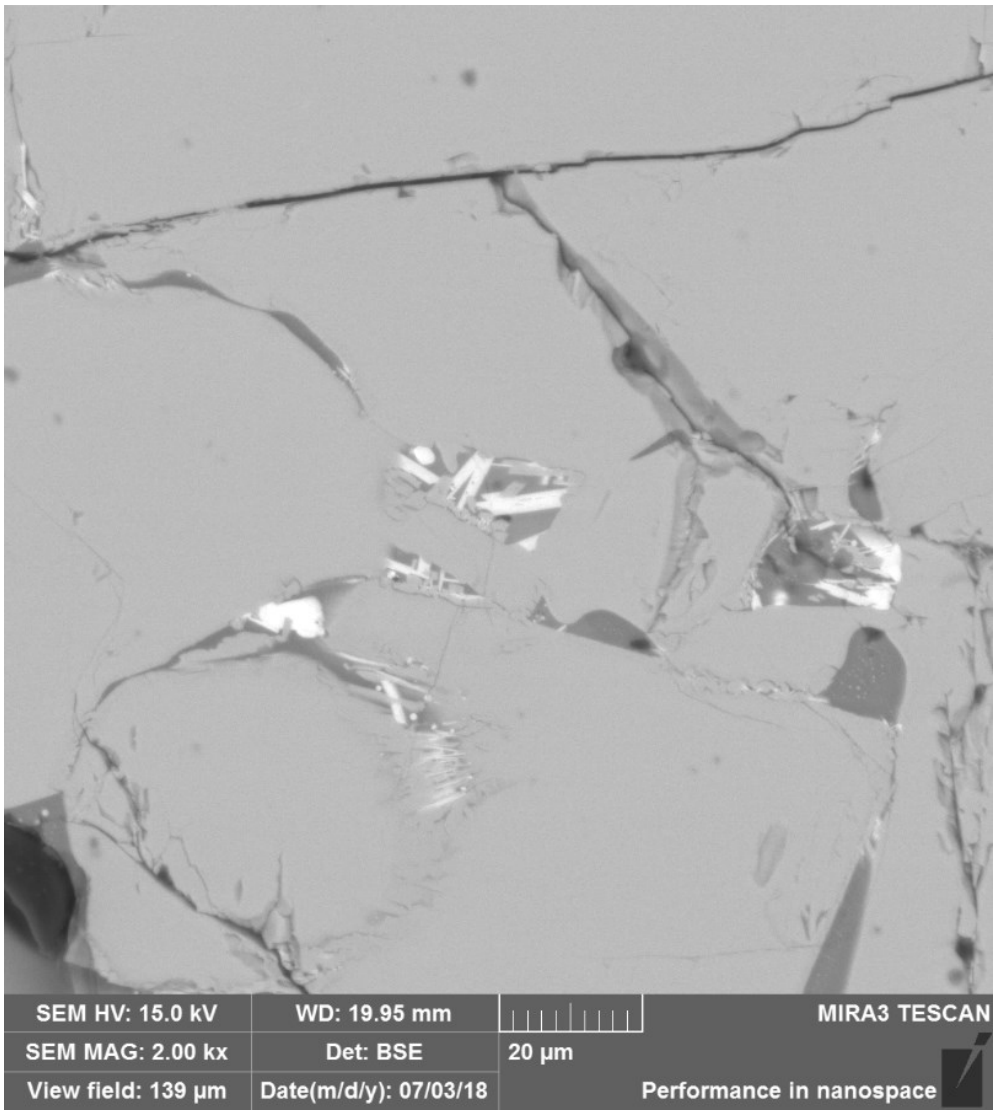

Appendix AC SEM-EDS – Sample X2 Site 2 EDS Sites

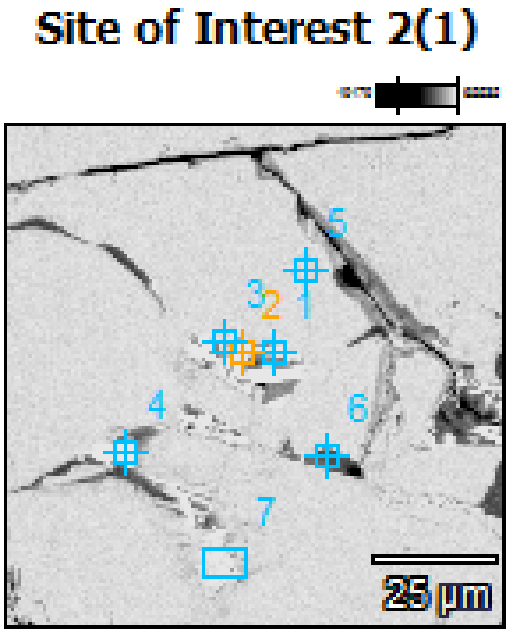

Appendix AD SEM-EDS – Sample X2 Site 2 EDS Analyses

Atom %

	O-K	Mg-K	Al-K	Si-K	Ca-K	Ti-K	Cr-K	Fe-K	Sn-L
Site of Interest 2(1)_pt1	67.54	0.13	1.11	4.34	0.96	25.91		0.00	
Site of Interest 2(1)_pt2	69.43	0.13	0.65	8.55	4.08	17.13		0.03	
Site of Interest 2(1)_pt3	65.62	0.04	0.51	1.68	0.24	31.92		0.00	
Site of Interest 2(1)_pt4	2.39	0.44	0.60	0.75	0.07	13.76	1.89	80.09	
Site of Interest 2(1)_pt5	41.99	3.09	1.70	0.09	0.01	50.53	0.78	1.82	
Site of Interest 2(1)_pt6	66.57	0.08	2.25	27.61	1.20	2.05		0.00	0.23
Site of Interest 2(1)_pt7	64.61	0.75	1.75	5.31	1.26	25.50		0.81	